Ultra Wide-Bandwidth Micro Energy Harvester

by

Arman Hajati

Bachelor of Science, University of Tehran (2003)
Master of Science, University of Tehran (2005)

Submitted to the Department of Electrical Engineering and Computer Science
in partial fulfillment of the requirements for the degree of

Doctor of Philosophy in Computer Science and Engineering

at the

MASSACHUSETTS INSTITUTE OF TECHNOLOGY

February 2011

Author .....
Department of Electrical Engineering and Computer Science
September 28, 2010

Certified by.....
Sang-Gook Kim
Associate Professor of Mechanical Engineering
Thesis Supervisor

Accepted by .....
Terry P. Orlando
Chairman, Department Committee on Graduate Theses

Ultra Wide-Bandwidth Micro Energy Harvester

by

Arman Hajati

Submitted to the Department of Electrical Engineering and Computer Science
on September 28, 2010, in partial fulfillment of the
requirements for the degree of
Doctor of Philosophy in Computer Science and Engineering

Abstract

An ultra wide-bandwidth resonating thin film PZT MEMS energy harvester has been designed, modeled, fabricated and tested. It harvests energy from parasitic ambient vibration at a wide range of amplitude and frequency via piezoelectric effect. At the present time, the designs of most piezoelectric energy devices have been based on high-Q linear cantilever beams that use the bending strain to generate electrical charge via piezoelectric effect. They suffer from very small bandwidth and low power density which prevents them from practical use. Contrarily, the new design utilizes the tensile stretching strain in doubly-anchored beams. The resultant stiffness nonlinearity due to the stretching provides a passive feedback and consequently a wide-band resonance. This wide bandwidth of resonance enables a robust power generation amid the uncertainty of the input vibration spectrum. The device is micro-fabricated by a combination of surface and bulk micro-machining processes. Released devices are packaged, poled and electro-mechanically tested to verify the wide-bandwidth nonlinear behavior of the system. Two orders of magnitude improvement in bandwidth and power density is demonstrated by comparing the frequency response of the system with that of an equivalent linear harvester with a similar Q-factor.

Thesis Supervisor: Sang-Gook Kim
Title: Associate Professor of Mechanical Engineering

Acknowledgments

Hereby, I would love to deeply acknowledge the people whose contributions have made my graduate experience at MIT a successful and wonderful one.

First, I would like to thank my advisor Professor Sang-Gook Kim for his support and guidance during the past four years. He has taught me a new way of thinking and looking at the problems. He provided me the ability of engineering thinking with his practical insight. There are many things I have learned from him that I will treasure for the rest of my life. Thank you very much.

Also, I thank my committee members, Professor Martin Schmidt and Professor Anantha Chandrakasan. They gave me great support and guidance in the committee meetings. Marty gave me wonderful technical suggestions and feedback on every aspects of the project. I would like to thank Anantha for his encouragements and support especially during the final months of my thesis. In addition, I would like to thank Dr. Dennis Buss for the friendly discussions that we had together. Furthermore, thank Prof. Lang for his comments and feedback during and after the final thesis defense.

I would like to thank my group mates Stephen Bathurst and Heonju Lee. They provided technical and emotional support as friends and we spend hours and hours discussing everything including technical, political and social stuff. I wish them success in their career and happiness in their life. Also, I would like to thank my former labmates Dr. Hyungwoo Lee, Dr. Soohyung Kim, Nathan Reticker-Flynn, Zachary Traina, Robert Xia, Jordan Peck, Jisoo Kim, Jessie Jeon, and Mark Roscher for technical advice and help. They made the Micro and Nano Systems Laboratory a constructive place with a friendly environment. I would look to specially thank Ray Hardin for his help and administrative support.

I thank all the MTL staffs as well as fellow researchers at MTL for your advices and supports. You have all made the countless hours at MTL more bearable. I especially like to thank Dennis Ward, Kurt Broderick, Donal Jamiesson, Eric Lim, Dave Terry, Bob Bicchieri and Vicky Diadiuk for help with processing, and be extremely patient

in helping me with machines. Also I have to thank Prof. Brian Wardle and Miso Kim for letting me access the laser vibrometer facility at their laboratory.

I would like to thank my friends, Amin Ajdari, Pedram Hassanzadeh, Hami Golbayani, Mina Karzand, Ali Marzban, Samira Faegh, Sohrab Eslami, Hoda Shojaei and Shervin Shahsavari for providing all the entertainment and support I needed during those stressful times. I would not be able to finish my thesis without them.

Lastly, I would like to thank my dad and mom for the sacrifices they made and their unconditional love. I would not be able to become who I am today without their unselfish support. I hope to do the same and be there for them. I also thank my sister Azadeh and my brother Omid for always being there for me, and I wish them the very best throughout their lives!

Contents

1 Introduction **29**

1.1 Thesis Objective and Contribution 31

1.2 Thesis Organization 31

2 Background **33**

2.1 Energy Harvesting 33

2.2 Vibration Energy Harvesting 36

2.2.1 Electrostatic Energy Harvesting 38

2.2.2 Electromagnetic Energy Harvesting 40

2.3 Piezoelectric Energy Harvesting 42

2.3.1 Piezoelectricity 42

2.4 Cantilever beam design 45

2.4.1 Previous Works 46

2.4.2 Type I: Piezoelectric Micro Power Generator 50

2.5 Discussion and Motivation 53

3 Design and Modeling **57**

3.1 Energy analysis 57

3.2 Redesign 60

3.2.1 Quality Factor 60

3.2.2 Strain Distribution 63

3.3 Doubly-clamped Structures 64

3.3.1 Stretching vs bending 64

3.3.2 Load-deflection Characteristics 65
3.4 2nd Generation: Pie-shaped Design 68
3.4.1 Mechanical Model 70
3.5 Frequency Response 73
3.5.1 Deflection 73
3.5.2 Multiple equilibrium points 75
3.5.3 Jump phenomenon 76
3.5.4 Strain vs Frequency 77
3.5.5 Robustness 78
3.5.6 Bandwidth 80
3.6 Design considerations 88
3.7 3rd Generation 91
3.7.1 Electrode Configuration 94
3.7.2 Properties 97

4 Fabrication **99**
4.1 2nd Generation: Pie-Shaped Structure 99
4.1.1 Structural Layer 99
4.1.2 Active Layer 102
4.1.3 Passivation 105
4.1.4 Etching and Release: Issues and Challenges 106
4.1.5 Released Device 110
4.2 3rd Generation 111
4.2.1 Stress Engineering 113
4.2.2 Structural Layer 115
4.2.3 Active Layer 116
4.2.4 Passivation Layer 120
4.2.5 Etching and Release 123

5 Testing and Discussion of Results **129**
5.1 XRD Crystallography 129

5.2 Packaging 132
5.2.1 Pie-shaped device 132
5.2.2 3rd generation 133
5.3 Testing Board 135
5.4 P-V Measurements 137
5.5 Poling 139
5.6 Electromechanical Testing Setup 144
5.7 Vibration Testing Results 147
5.8 Output Measurement 150

6 Electronic circuits and interfaces **159**
6.1 Electrical Interface 159
6.1.1 Electromechanical Model 160
6.1.2 Piezoelectric energy harvesting interfaces 162
6.1.3 Power Estimation 169
6.2 Start-up Circuit 170

7 Summary and Conclusions **175**
7.1 Thesis Summary and Conclusion 175
7.2 Future Work 176

A MATLAB Codes **179**
A.1 Piezoelectric Energy Harvester Response 179
A.2 Designing the Mask 181
A.3 Interdigitated Electrodes Mask, 3rd Generation 185

B Masks **187**

List of Figures

2-1 Comparison of power from vibrations, solar and various battery chemistries. (from [1–3]) 36

2-2 Three possible topologies for MEMS-scale electrostatic energy harvester: (a) in-plane overlap type, (b) in-plane gap closing type, (c) out-of-plane gap closing type [1–3]. 38

2-3 The mechanical schematic of a typical electromagnetic energy harvester [4]. 40

2-4 The structure of a typical electromagnetic energy harvester [5]. 40

2-5 perovskite crystal structure: left) above Curie point cubic lattice, symmetric arrangement of positive and negative charges, right) below Curie point tetragonal (orthorhombic) lattice, crystal has dielectric dipole. [6] 43

2-6 Direction conventions for PZT: direction of positive polarization coincides with Z-axis [7] 44

2-7 Linear piezoelectric energy harvesting scheme based on a simple cantilever 45

2-8 d_{31} and d_{33} modes in PZT thin film [8] 46

2-9 Parasitic power shoes project at MIT Media Lab (from [9]) 47

2-10 Picture of bulk piezoelectric energy harvester developed by Roundy et al. at UC Berkeley (from [1]). 47

2-11 Type-I piezoelectric energy harvester (PMPG): SEM images of the stress-controlled cantilevers consisting of (a) PZT/ZrO2/SiO_2(thermal), (b) PZT/ZrO_2/SiO_2(PECVD) and (c) PZT/ZrO_2/SiO_2(PECVD)/SiN_x (from [10]) 51

2-12 Schematic of the type-I PMPG structure based on d_{33} piezoelectric mode. (from [10]) 51
2-13 Picture of power generator prototype based on an array of cantilever beams (from [11]) 54

3-1 Piezoelectric energy harvesting concept in energy domain 57
3-2 Transmissibility of a linear resonator as a function of its damping ratio shows gain × bandwidth limitation dilemma in linear systems 59
3-3 Beam length versus its thickness to achieve 0.1% strain at 1g level of acceleration (100Hz) for various Q-factor 62
3-4 The proof mass required to reach 0.1% strain at a constant natural frequency constant (100Hz). 62
3-5 tri-angular shaped harvester by IMTEK are more effective than rectangular-shaped beam in terms of strain distribution. [12] 63
3-6 Strain distribution in geometry-optimized tri-spiral design with a heavy central proof mass. 64
3-7 Bending vs stretching in a doubly-clamped beam 65
3-8 Strain distribution in doubly-clamped structures: Bending vs stretching 66
3-9 Schematic structure of pie-shaped design with interdigitated electrodes. 69
3-10 Lumped model of the system: a nonlinear stiffness due to the stretching in the doubly-clamped structure is added to the typical linear model . 70
3-11 Simulated frequency response of the pie-shaped structure. 74
3-12 Pie-shaped harvester shows unique solution at low frequency and high frequency ranges (red). But more than one equilibrium points is possible in the mid-range frequencies (350Hz-1100Hz): high-amplitude stable response (cyan), unstable response (blue) and low-amplitude stable response (green). Convergence to each of these regions depend on the initial conditions or the excitation pattern. 75
3-13 Jump phenomenon in ramp-up (green) and ramp down (red) response due to the Duffing nonlinearity. 77

3-14 Resulting stretching strain versus bending strain in the PZT layer as a function of frequency at a constant excitation amplitude. 78

3-15 The amplitude of vibration is pretty robust to the excitation amplitude as long as it is larger than the jump-down threshold. 79

3-16 The effect of the total damping including mechanical damping and electrical damping on the frequency response of the system. 80

3-17 The ratio of harvestable power to the maximum power as a function of frequency based on the strain level evaluated in Figure 3-14. 81

3-18 At every frequency below the jump-down frequency, the upper limit of the electrical power harvesting is defined by the maximum electrical damping at the threshold of the jump-down. 82

3-19 The maximum vibration amplitude and electrical damping ratio as a function of frequency. 83

3-20 The maximum electrical power extractable as a function of frequency. This power is calculated based on the maximum electrical damping that may push the vibration to jump-down. Therefore its realization requires an ideal electrical interface. 84

3-21 The wide-bandwidth resonance of the system can be explained by the negative feedback resulting from Duffing stiffness. Stretching stiffness induces an amplitude-dependent stiffness which forces the equivalent resonance frequency to track the excitation frequency. 84

3-22 The nonlinear feedback keeps the resonator pre-resonance by acting like a barrier. The resonator needs a strong disturbance to climb this barrier. The arrows show qualitatively how large is the barrier (due to the nonlinearity) which keeps the system in the high-energy stable region. Increasing the electrical damping weakens the nonlinear feedback and decreases the barrier size. Finally at $\zeta_{E,max}$ there is no barrier and the system jumps down to the low-energy level without any external disturbance. 87

3-23 Increasing the number of rectangular beams in the pie-shaped structure decreases the active area. Wide doubly-clamped rectangular-shaped beams with central proof mass is a more efficient topology (75% active) compared to the pie-shaped designs (37.5% and 30% active area in case of 4-beam and 8-beam topologies, respectively) 92

3-24 The schematic structure of 3rd generation energy harvester: a) the main part consists of four doubly clamped beams, b) the external proof mass, c) the assembled part 93

3-25 Interdigitated (IDT) electrodes extract the generated charge from PZT using d_{33} mode of piezoelectric effect. All the electrode have been electrically connected in parallel to increase the output current. . . . 94

3-26 Bending strain (top) and stretching strain (down) distribution across the length and thickness of the doubly-clamped beams. Half of the beam's length would undergo a compressive bending strain while the other half is in tension. 95

3-27 Splitting the length of the beam into two pairs of electrodes: a) d_{31} mode electrodes, b) d_{33} mode electrodes (IDT) 96

3-28 IDT electrodes configuration in the 3rd generation device 96

4-1 Schematic cross-section of the device 99

4-2 200Å Ti/2000Å Pt are e-beamed and patterned by lift-off. IDT electrodes collect the electrical charge generated in the PZT layer in d_{33} mode. 105

4-3 dry-etched vias (yellow circles) in the passivating layer provides access to the pads for wire-bonding 106

4-4 Large undercut in PZT during the wet-etching with BOE solution. . . 107

4-5 Optical image of a released device (top view) 109

4-6 Undercuts in the silicon proof mass (dark brown), the IDT electrodes behind the transparent LPCVD nitride, and the openings between beams can be easily seen in the optical image of a released device taken from its back. 109

4-7 Fully released device (back side) 110

4-8 SEM image of a released device shows the interdigitated electrodes . . 110

4-9 Optical image of a released device (top view) 111

4-10 Fabrication process plan 112

4-11 Asymmetrical distribution of residual stress with respect to the neutral axis may generate a crack at the anchors and brake the device. The released device (right) is broken and buckled upward to release the bending moment resulted from the stress distribution. 114

4-12 The stress distribution across the thickness of the structure. 115

4-13 Patterned ZrO_2/PZT after annealing. 117

4-14 XeF_2 can attack the IDT electrodes especially by undercutting the adhesion layer (Ti). 118

4-15 200Å Ti/2000Å Au are e-beamed and patterned by lift-off to form the IDT electrodes. The electrode material has been switched to Aluminum in further batches to avoid the attack by XeF_2. 119

4-16 The residual stress of the Plasma Enhanced Chemical Vapor Deposited (PECVD) films can be controlled by changing the ratio of high frequency mode interval to the total time. (Data courtesy of Donal Jamieson from MTL). 121

4-17 An opening has been etched in the passivation layer at the pad areas. Each device will be connected electronically to the package through wire-bonding to these pads. Gold pads have been slightly over-etched by the XeF_2 etchant, but this problem has been solved by using Aluminum pads. 124

4-18 Pre-released devices are cut and separated from the main wafer automatically at the end of DRIE step. Each device will be fully released later by XeF_2 etchant. The 4" wafer is simply mounted on a 6" glass wafers by Kapton tape. 125

4-19 The optical image of a fully released 3rd generation device. 127

4-20 The optical image of a fully released 3rd generation device from its backside. The IDT electrodes are visibly through the optically transparent structural layer. 128

4-21 A complete device under the probe-station. 128

5-1 X-Ray diffraction crystallography shows strong < 110 > perovskite peak for type-E PZT. 130

5-2 Type-G3 PZT (thick film) crystallized mainly at the < 111 > Perovskite phase. 131

5-3 Released device is super glued to a PGA package. Electrodes are wire-bonded to the package's pads. 132

5-4 A silicon base has been fabricated by KOH etching of a silicon wafer. It fills the cavity of the CPGA package, acts as the base for the device and provide enough room for the proof mass downward motion. . . . 133

5-5 Each cell of a device has four pairs of electrodes which are wire-bonded to the designated pads in the package (marked in red). 134

5-6 The wire-bonding setup. Aluminum pads on the packaged device are bonded by gold wires to the pads on a ceramic pin grid arrays (CPGA) package. 134

5-7 The testing board for a pie-shaped device: each package has been directly soldered to a perforated PCB. 135

5-8 Packaged devices can be easily mounted on the testing board for P-V measurements and electromechanical vibration tests. Each pair of electrode can be independently controlled by the DIP switches on the testing board. 136

5-9 Measured P-V curve for the poled pie-shaped energy harvester. 137

5-10 Measured P-V curve for the poled 3rd generation energy harvester. . 138

5-11 polarizing (poling) a piezoelectric ceramic [7] 139

5-12 First poling setup 140

5-13 Second poling setup: the packaged device mounted on the testing-board is heated by convection at a well-controlled temperature condition. 141

5-14 Excessive heat and electric field can result in the dielectric breakdown. The dielectric layer has been destroyed and a crack has been propagated from the breakdown region. 142

5-15 New poling process avoids the breakdown using a limiting resistor. The graph shows the effective poling voltage, current and temperature as a function of poling time. 143

5-16 Electromechanical test setup: laser vibrometer measure the velocity of the proof mass and the base of the device excited by electromagnetic shaker. The output electrical charge is measured by the charge amplifier. 144

5-17 Schematic diagram of electromechanical test setup. 145

5-18 The position of laser can be controlled by the software. The velocity of the base and also the proof mass can be measured using multi-point measurement mode. 146

5-19 The testing board in connected to the shaker by 5 screws to improve the rigidity of the structure during vibration testing (left). Packaged devices can be easily mounted on the socket for electromechanical testings (right). 146

5-20 The initial testing shows a very high frequency resonance (2.7kHz). . 147

5-21 Nano-indentation result: the force is a linear function of displacement and the stiffness is estimated about 5300N/m. 148

5-22 External heavy metallic mass attached to the proof mass of the pie-shaped harvester to decrease the resonance frequency. 149

5-23 System's frequency response: *up* simulated response: nonlinear broadband system shows a wide bandwidth (73Hz) compared to the equivalent linear system that provides a very narrow bandwidth (8.5Hz) at the same gain and damping (Q=85), *down* experimental response verifies the simulation. 151

5-24 Measured output charge from the pie-shaped energy harvester. 152

5-25 The open circuit output voltage from the 3rd generation device with rotated IDT electrodes. 153

5-26 Measured open-circuit voltage generated by the harvester (peak-to-peak value in millivolts). 154

5-27 Calculated electric current source (peak-to-peak value in microampers). 155

5-28 Measured displacement (top) and open-circuit voltage (bottom) spectrum generated by the harvester (low-g condition: shaker input of 0.05V). 156

5-29 Measured displacement (top) and open-circuit voltage (bottom) spectrum generated by the harvester (mid-g condition: shaker input of 0.4V). 157

5-30 Measured open-circuit voltage spectrum generated by the harvester (high-g condition: shaker input of 1.0V). 158

6-1 A classical piezoelectric energy harvesting interface implemented in the PMPG device. The AC signal generated by the piezoelectric layer is converted to a DC source using a bridge rectifier followed by a filtering capacitor [10]. 160

6-2 The bending strain acts as a current source which is in phase with the velocity of the proof mass. The stretching strain oscillates at twice the frequency of vibration. 162

6-3 Classic DC interface [13]. 162

6-4 Classic AC interface [14]. 163

6-5 Simulated current and voltage waveform for a DC classic interface [15]. 164

6-6 Voltage doubler interface [13]. 165

6-7 Simulated current and voltage waveform for a voltage doubler interface [15]. 165
6-8 Adding an inductor to the classic AC interface can improve the efficiency. 166
6-9 A switching inductor circuit and its corresponding voltage, current and switching waveforms. 166
6-10 Synchronized switch harvesting on the inductor (SSHI) interface [13]. 167
6-11 Simulated current and voltage waveforms for a voltage doubler interface. 167
6-12 synchronized charge extraction (SCE) interface [13]. 168
6-13 synchronized charge extraction (SCE) interface [13]. 169
6-14 Calculated Matched resistive load, extractable electric power and the power density based on a classic AC interface. 171
6-15 Calculated extractable electric power based on a SSHI interface (Q_I=10). 172
6-16 Block diagram of the start-up circuit simulated in MATLAB/Simulink. 172
6-17 The effect of the start-up circuit on the response of the nonlinear energy harvester. Activating the circuit for a short period of time can push the system from low-amplitude stable region (up) to its high-amplitude stable region. 174

List of Tables

2.1 Comparison of power scavenging and energy sources (from [1,3]). . . 35

2.2 Acceleration (m/s^2) magnitude and frequency of fundamental vibration mode for various sources (from [1,3]). 37

2.3 Comparison of the relative merits of three primary types of converters (from [1,3]). 37

2.4 Comparison among MEMS electrostatic energy harvesting devices (from [16]). 39

2.5 Summary of electromagnetic energy harvesters. (from [17]). 41

2.6 Summary of piezoelectric energy harvesters. (updated from [17]). . . 48

2.7 Coefficients of common piezoelectric materials. (from [17]). 50

3.1 Typical properties of PZT. 60

3.2 Typical design parameters of pie-shaped energy harvester that has been used in the simulation. 74

4.1 Measured average change in the bow of the wafer from the films in the structure. The KLA-Tencor FLX 2320 system has been off-calibration during the measurements and all the values have been updated accordingly. 114

Nomenclature

A	Acceleration level (m/s^2)
A_{ex}	Excitation acceleration (m/s^2)
A_{IDT}	Effective area of interdigitated electrodes (m^2)
C_0	clamped capacitance (F)
c_a	Aerodynamic damping coefficient (N.s/m)
c_c	Critical damping coefficient (N.s/m)
c_E	Equivalent electric damping coefficient (N.s/m)
c_{eq}	Equivalent linear damping coefficient (N.s/m)
c_M	Equivalent mechanical damping coefficient (N.s/m)
C_r	Filtering capacitance (F)
c_s	Structural damping coefficient (N.s/m)
$C\left(\dot{z}, I_{Load}\right)$	Total damping force (N)
D	Charge density (C/m^2)
d	Piezoelectric coefficient (C/N)
D_{in}	Inner diameter of pie-shaped structure (m)
D_{out}	Outer diameter of pie-shaped structure (m)
E	Electric field (V/m)
E_c	Coercive electric field (V/m)
$\bar{\dot{E}}_{ex}$	Average rate of energy change (J/s)
$\bar{\dot{e}}_e$	Electrical power generation density (W/m^3)
F	Force at the proof mass (N)
$F_e\left(z, I_{Load}\right)$	Electrical damping force (N)
f_{ex}	Excitation frequency (Hz)

f_n	Linear natural frequency (Hz)
$f_{n,eq}$	Equivalent linear natural frequency (Hz)
F_{peak}	Peak frequency (Hz)
$G(j\omega_{ex})$	Linear transmissibility
$\|G(j\omega)\|$	Linear gain -
$\angle G(j\omega_{ex})$	Phase delay -
g	Piezoelectric voltage coefficient (Vm/N)
I	Electric current (A)
I_{Load}	shunting current across the resistive load (A)
I_S	Stretching-based current source (A)
$I_{S,max}$	Maximum stretching-based current source (A)
k_{33}	Piezoelectric coupling factor (%)
k_B	Linear stiffness due to bending (N/m)
k_{eq}	Equivalent linear stiffness (N/m)
k_S	Nonlinear stiffness due to stretching (N/m^3)
k_{σ_0}	Linear stiffness due to residual stress (N/m)
L	Beam length (m)
m_{pm}	Proof mass (kg)
P	Output electric power (W)
P_{max}	Maximum extractable eletric power (W)
P_r	Remnant polarization (C/m^2)
P_s	Saturation polarization (C/m^2)
Q	Quality factor -
Q_0	Quality factor with no electric loading -
Q_I	Inversion quality factor -
Q_T	Quality factor with electric loading -
R	Resistive load (Ω)
R_{opt}	Optimum electric load at matched condition (Ω)
S	Strain -
s_E	Compliance (1/Pa)

S_B	Bending strain (%)
S_S	Stretching strain (%)
S_T	Total strain (%)
S_{max}	Maximum allowable strain before failure (%)
T	Stress (Pa)
t	Beam thickness (m)
t_{beam}	Thickness of beam (m)
t_s	Switching time (s)
t_{PZT}	Thickness of PZT layer (m)
$u(x)$	Deflection of the neutral axis (m)
$\tilde{W}$	Modified strain energy from deformation (J/m^3)
V	Voltage across the piezo element (v)
V_{DC}	Output voltage across the load (v)
w	Beam width (m)
w_f	Electrode finger width (m)
w_g	Gap between interdigitated electrodes (m)
Y	Young's modulus (Pa)
Y_{beam}	Young's modulus of beam (Pa)
y_{ex}	Base motion (m)
y_{pm}	Proof mass motion (m)
Z	Deflection in phasor domain (m)
z	Distance from neutral axis (m)
α_B	Bending-based mechanical to electrical force factor (A.s/m)
α_E	Electrical to mechanical force factor (N/v)
α_S	Stretching-based mechanical to electrical force factor ($A.s/m^2$)
δ	Beam deflection (m)
ϵ_r	Relative permittivity -
ϵ_T	Permittivity (F/m)
ζ	Damping ratio -

ζ_E	Electrical damping ratio -
η	Structural damping coefficient -
$\eta_{filling}$	Filling factor (%)
ν	Poisson ratio (%)
$\rho_{proof\,mass}$	mass density of the proof mass (kg/m^3)
σ_0	Residual stress (Pa)
$\Delta\omega$	Power bandwidth (Rad/sec)
ω_{ex}	Excitation frequency (Rad/s)

Acronym

3D	Three-dimensional
AFM	Atomicmforce microscopy
$BaTiO_3$	Barium titanate
BHF	Buffered hydrofluoric acid
BNC	Bayonet Neill-Concelman connector
CMOS	Complementary metal-oxide-semiconductor
CPGA	Ceramic pin grid array
CPU	Central processing unit
DAQ	Data acquisition
DI	Distilled water
DIP	Dual in-line package
DMSE	Department of material science and engineering
DRIE	Deep reactive ion etching
ECR	Electron cyclotron resonance
EM	Electromagnetic
FEM	Finite element model
HD	High definition

HVAC	Heating, ventilating, and air conditioning
ICL	Integrated circuit laboratory
IDT	Interdigitated
LPCVD	Low pressure chemical vapor depositon
LTO	Low temperature oxide
MEMS	Micro electro-mechanical systems
MFC	Macro fiber composite
MTL	Microsystems technology laboratory
PCB	Printed circuit board
PCI	Peripheral component interconnect
PECVD	Plasma enhanced chemical vapor deposition
PEH	Piezoelectric energy harvester
PMN-PT	lead magnesium niobate-lead titanate
PMPG	Piezoelectric micro power generator
PT	Lead titanate
P-V	Polarization vs Voltage
PVDF	Polyvinylidene fluoride
PZT	Lead zirconate titanate $Pb(Zr,Ti)O_3$
Q-factor	Quality factor
RF	Radio frequency
RFID	Radio-frequency identification
RIE	Reactive ion etching
RPM	Rotation per minute
RTA	Rapid thermal annealing
SCE	Synchronized charge extraction
SEM	Scanning electron microscope
SHM	Structural health monitoring
SOC	System-on-chip
SOI	Silicon-on-insulator
SSD	Synchronized switch damping

SSHI	Synchronized switch harvesting on inductor
SSHC	Synchronized switch harvesting on capacitor
TDP	Thermal design power
TRL	Technology research laboratory
UWB	Ultra wide-bandwidth
ULP	Ultra low-power
XRD	X-ray diffraction crystallography

Chapter 1

Introduction

Energy harvesting is the process by which electrical energy is extracted and converted from ambient energy sources and has been around for centuries in the form of wind mills and turbines, watermills, hydroelectric dams and solar power systems. Compared to the macro-scale harvesting technologies, a recent frontier is micro-scale energy harvesting. The aim is to scavenge microwatts to milliwatts of electrical power from solar, vibration, thermal, electromagnetic, and biological sources.

A decade ago, micro-scale energy harvesting could have been called a scientific curiosity [18]. Nevertheless, by recent developments in CMOS technologies in scaling the power consumption down to ultra-low-power (ULP) level, a new horizon can be seen for micro-scale energy harvesting systems. For the first time, the electric power generated by the MEMS-scale harvesters seems adequate to power ULP circuits and wireless sensors. Consequently, micro-scale energy harvesting has become of a growing interest in the last few years.

Many environments are subjected to ambient energy which can be harvested to power wireless electronics. Additionally, energy harvesting is very important for systems which do not allow battery replacement or are not able to have wired power coupling, e.g. tire pressure sensors. A practical harvester has to be relatively small in order to be applicable in the aforementioned applications.

Ambient energy exists in the environment of the system and is not stored explicitly for reuse. The most familiar ambient energy source is solar power. Other examples

include electromagnetic fields (used in RF powered ID tags, inductively powered smart cards, etc.), thermal gradients, fluid flow, energy produced by the human body, and the action of gravitational fields.

Several vibration energy harvesting methods exist including the use of electromagnetic induction [4,17,19–31], electrostatic generation [16,22,32–41], and piezoelectric materials [1,9,10,42–60]. While each of the above-mentioned techniques can provide a useful amount of energy, piezoelectric materials have received the most attention due to their ability to directly convert applied strain energy into usable electric energy. Furthermore, piezoelectric energy harvesters can be easily integrated into a system, especially in MEMS-scale. In addition, piezoelectric energy harvesting has a high theoretical power density and accordingly is considered as an attractive option. Among the available piezoelectric materials, lead zirconate titanate (PZT) shows a very high coupling factor and has been used in most piezoelectric energy harvester.

At the present time, most piezoelectric energy devices have been designed to have high-Q linear cantilever beams that resonate at small environmental vibrations and result in sizable bending strain on the piezoelectric layer to generate electrical charge [17, 55, 61–63]. There are however, some intrinsic problems associated with this approach. Harvested power decays sharply if the input vibration frequency is off more than 1-2% from the natural frequency of the beam structure. The higher the Q-factor, the less robust the system becomes.

Furthermore, the density of the actual harvested power that has been reported is orders of magnitude less than the maximum power density that can be extracted from PZT theoretically. This is due to the fact that the bending of a cantilever beam cannot generate large enough strain. Our group has reported the first working MEMS-scale cantilever-based piezoelectric power generator using thin film PZT [8,10,64,65], which also suffered from a narrow bandwidth and low power density. Various passive and active frequency-tuning mechanisms have been reported [11,66–69], but in reality they have not yet provided a practical solution to make the energy harvesting devices efficient. A simple broadband design is required to make energy harvesting devices compact, efficient and practically deployable.

1.1 Thesis Objective and Contribution

We report a MEMS energy harvester that resonates in a wide frequency range without any active tuning mechanism. The key idea is to utilize the stretching strain in thin doubly-anchored beams instead of the bending strain in cantilever structures. The resulting non-linear stiffness provides a passive feedback and consequently a wide-band resonance. In addition, unlike bending strain, stretching strain is almost uniform across the structure and boosted rapidly for very small deflection levels.

The novelty of our design is a device structure that ensures the dominance of the stretching mode of the beams. Therefore, most of the kinetic energy from the external vibration can be converted into elastic energy in the form of stretching and subsequently to electric energy via piezoelectric effect. Moreover, its corresponding nonlinear stiffening would enhance the bandwidth. Consequently, this design enables us to harness the maximum theoretical power density from the piezoelectric material without sacrificing the bandwidth [70, 71].

The objective of this research is to study the nonlinear nature of the stretching beams, model its behavior and provide design considerations to achieve the wanted performance. In addition, it includes the concept verification by developing and fabrication of a prototype and its experimental testings.

1.2 Thesis Organization

The thesis is organized to provide a comprehensive review of the problem description, design considerations, theoretical analysis and modeling, experimental methods and results. Chapter 1 introduces the concept of energy harvesting and also the objective of this work. Chapter 2 reviews the theory, background, and current practices related to energy harvesting and specifically MEMS-scale piezoelectric energy harvesting. Chapter 3 provides an extensive and comprehensive theoretical analysis of the UWB energy harvester. It includes the design, mechanical modeling and nonlinear analysis of the new harvester. Based on the analysis, a set of design guideline and criteria

has been suggested to improve the performance of the system. Chapter 4 provides a detail review of the fabrication steps and considerations utilized to micro-machine the pie-shaped and 3rd generation harvesters. Chapter 5 includes the packaging process, testing setup, and the measurement results. Chapter 6 discusses the electronic circuits used in this research and also the possible electronic interfaces that can boost the power harvesting capabilities. Chapter 7 is a discussion of the results and areas for future improvement.

Chapter 2

Background

2.1 Energy Harvesting

Over the past few decades, the CMOS technology has been scaled continuously following the Moore's law. Currently, the 32-nm process is being used in developing ultra-low power digital chips and also mixed-signal system-on-chips (SOC). For example, the new Intel i5-540UM processor has 382 million transistors with a die-size of only $81mm^2$ [72]. This chip consumes only 15W (TDP) and hence provide an extremely high processing power at such a low power. Qualcomm Inc. is developing a single-chip dual-CPU QSD8672 which is an ULP SOC. Significant processing power, full HD video processing, wireless networking and 3D graphics capabilities has been enabled in this single chip [73]. The ultra low power consumption of these chips has enabled new handheld products like smartphones and tablets.

Exploiting these new technologies, the use of wireless sensors and wearable electronics has grown steadily. Wireless systems are becoming ubiquitous; examples include wireless networking and wireless connectivity of portable devices and computer peripherals using the Bluetooth standard [17]. Electrochemical batteries have remained the main power source for these systems. Nevertheless, the battery technology has not seen Moore's Law-like progress and has developed at a much slower pace in terms of energy density. Consequently, the power source has become the main challenge in portable devices and also wireless networks.

The issue of replenishing energy is especially important in wireless applications. If conventional batteries were to be used, one would also need to include the cost of battery replacement. Replacing batteries at hostile, large terrain or inaccessible environment can be extremely expensive. Wireless sensors that are embedded in structures such as buildings, bridges or rotary systems do not allow foreign access to replenish their energies. Replacing batteries for artificial heart can be expensive and harmful to the patient. Consequently, researchers have begun investigating micro-scale energy harvesting as a solution to extend the life and reduce the volume of the electronics.

Several micro-scale energy harvesting sources to power ULP systems can be identified [74]:

- Motion, vibration or mechanical energy from: floors, stairs, home appliances, object's movement, engines, fluid flow, acoustic, etc. The electromechanical transducer can be electromagnetic [9], electrostatic [10], or piezoelectric.
- Electromagnetic (RF): Base stations, wireless internet, satellite communication, radio, TV, digital multimedia broadcasting, etc. One must not confuse between electromagnetic energy source and electromagnetic transducer. In some articles, electromagnetic generator is used for electromagnetic transducer.
- Thermal.
- Momentum generated by radioactive reactions into electrical energy.
- Pressure gradients.
- Solar and light.
- Biological.

Roundy et al. at UC Berkeley are among the early researchers who consider the possibility of harvesting ambient energy as a power source for wireless sensor nodes [1, 3]. The power density of potential ambient sources for energy harvesting

Table 2.1: Comparison of power scavenging and energy sources (from [1,3]).

Energy Source	Power density ($\mu W/cm^3$) 10 years lifetime
Solar (outdoor)	15000 (Direct sun), 150 (Cloudy day)
Solar (indoor)	6 (Office desk)
Vibration (piezoelectric)	250
Vibration (electrostatic)	50
Acoustic noise	0.003 at 75dB, 0.96 at 100dB
Temperature gradient	15 (at $10°C$ gradient)
Shoe inserts	330
Batteries (non-rechargeable lithium)	3.5
Batteries (rechargeable lithium)	0
Hydrocarbon fuel (micro heat-engine)	33
Fueld cells (methanol)	28

and also the energy storage systems is compared over a 10 year lifetime (Table 2.1). A graphical comparison of solar power, vibration conversion and battery power (the most common alternative) is shown in Figure 2-1. The shaded boxes indicate the feasible power density from solar and vibration energy which are not a function of time. The other five curves estimate the average available power density form different battery technologies.

The graph indicates that if the desired lifetime of the system is less than 1 year, battery technology can provide enough energy and should be employed. However, if longer lifetime is required (e.g. 5 years or more), there is a need for battery replacement due to the leakage. Consequently, energy harvesting techniques seem to be a reasonable candidate for applications like wireless sensors which require a long lifetime.

Based on Roundy's estimates, vibrational energy harvesting via piezoelectric conversion has a high power density (250 $\mu W/cm^3$), only second to solar power (15,000 $\mu W/cm^3$). In theory, much higher power density (3.6 W/cm^3) is achievable via piezoelectric energy harvesting as will be explained in Section 3.1. If one were to take into account the cost of manufacturing and applications such as powering low cost devices, then hydrocarbon fuel and fuel cells are too extravagant and expensive. Solar cells are a mature technology and a mature research area. If outdoor sunlight, or relatively

intense indoor light is available, solar cells appear to be the best alternative. Otherwise, solar power is impractical especially in embedded applications; thus, vibration energy harvesting can be a more attractive option for this type of applications.

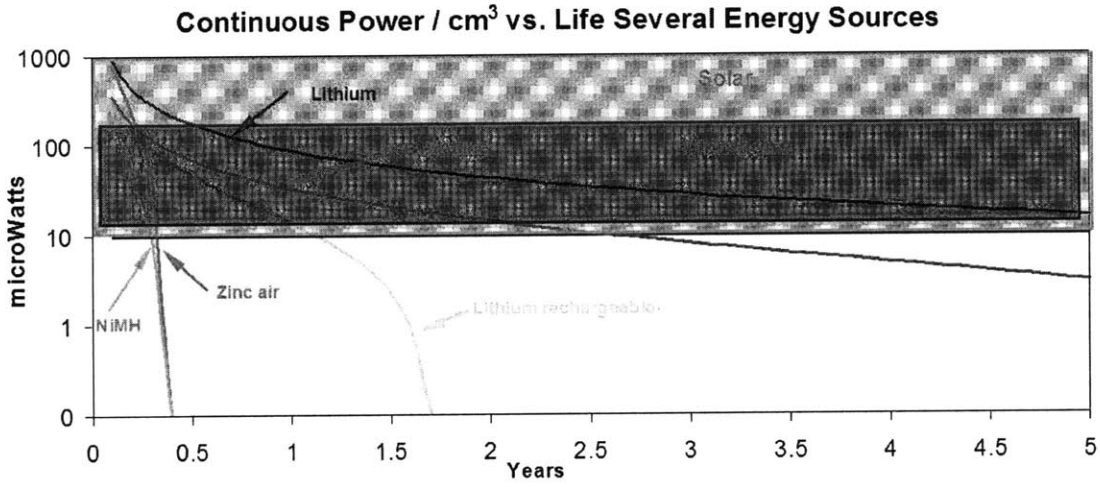

Figure 2-1: Comparison of power from vibrations, solar and various battery chemistries. (from [1–3])

2.2 Vibration Energy Harvesting

There are many advantages of using an ambient vibrational energy source such as:

- The energy source can have an infinite lifetime, which means the device can have an infinite shelf life.
- The device can be enclosed and protected from the harsh environment.

A variety of commonly occurring vibration have been measured by Roundy in terms of the frequency and acceleration magnitude of the fundamental vibration mode (Table 2.2). It can be inferred that a practical energy harvester should generate enough power from less than 1g acceleration level at frequencies less than 200Hz.

There are three basic mechanisms by which vibrations can be converted to electrical energy: electro-magnetic, electrostatic, and piezoelectric. In the first case, the relative motion between a coil and a magnetic field induces a current to flow in the

Table 2.2: Acceleration (m/s^2) magnitude and frequency of fundamental vibration mode for various sources (from [1,3]).

Vibration source	$A(m/s^2)$	$F_{peak}(Hz)$
Car engine compartment	12	200
Base of 3-axis machine tool	10	70
Blender casing	6.4	121
Clothes dryer	3.5	121
Person nervously tapping their heel	3	1
Car instrument panel	3	13
Door frame just after door closes	3	125
Small microwave oven	2.5	121
HVAC vents in office building	0.2-1.5	60
Windows next to a busy road	0.7	100
CD on notebook computer	0.6	75
Second story floor of busy office	0.2	100

Table 2.3: Comparison of the relative merits of three primary types of converters (from [1,3]).

Mechanism	Advantages	Disadvantages
Piezoelectric	No voltage source needed Output voltage (3-8V)	More difficult to integrate in microsystems
Electrostatic	Easier to integrate in microsystems	Separate voltage source needed Practical difficulties
Electromagnetic	No voltage source needed	Output voltage is 0.1-0.2 V

coil. Electrostatic generation consists of two conductors separated by a dielectric (i.e. a capacitor), which move relative to one another. As the conductors move the energy stored in the capacitor changes, thus providing the mechanism for mechanical to electrical energy conversion. Finally, mechanical strain in a piezoelectric material causes a charge separation across the material (which is a dielectric), producing a voltage. Table 2.3 gives a qualitative comparison of the merits of each energy harvesting methods.

2.2.1 Electrostatic Energy Harvesting

Electrostatic energy harvesters are very similar to the micro-machined capacitive accelerometers developed by Prof. Howe's team at UC berkeley and commercialized by Analog Device Inc. [75,76]. The mechanical motion changes the system's capacitance by moving one set of electrodes with respect to the other one. Consequently, the mechanical energy can be converted into electrical energy if the generated charge can be adequately extracted. This mechanism has been well developed at MEMS scale for inertial sensing applications. The whole MEMS structure can be fabricated using CMOS-compatible processes and can be well integrated with the electronics.

The main disadvantage of the electrostatic harvesters is the need for a separate voltage source. In addition, a practical harvester requires an additional mechanical motion-limiting mechanism. Otherwise, at large motion cases, the electrodes may touch each other and a short-circuit can happen as a result. This reliability issue should be considered in practical applications.

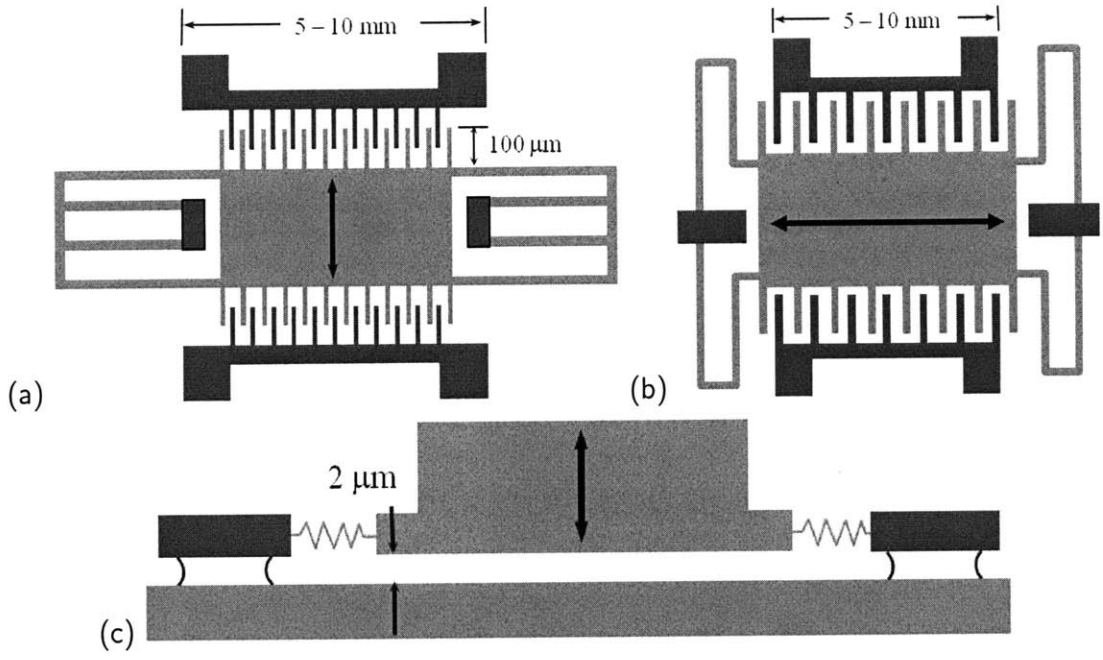

Figure 2-2: Three possible topologies for MEMS-scale electrostatic energy harvester: (a) in-plane overlap type, (b) in-plane gap closing type, (c) out-of-plane gap closing type [1–3].

Table 2.4: Comparison among MEMS electrostatic energy harvesting devices (from [16]).

Author	Frequency (Hz)	Input acceleration (m/s^2)	Volume (mm^3)	Power (μW)	Power density ($\mu W cm^{-3}$)
Menigner et al. [32]	2520		75	8*	106
Kuehne et al. [33]	1000	1.96		4.28*	
Chiu et al. [34]	1870	32.5	600	1.2	2
Hoffmann et al. [35]	1460	130		0.6	
Despesse et al. [36]	50	8.8	1800	1052	584
Basset et al. [37]	250	2.5	61.49	0.061	0.99
Arakawa et al. [38]	10	3.9	400	6	15
Lo et al. [39]	50	576.6	50000	18	0.36
Naruse et al. [40]	2	4		40	
Mitcheson et al. [41]	30	50	750	3.7*	4.93
Mizuno et al. [22]	743	13.9	600	7.4e-4	1.23e-3
Yang et al. [16]	63	2.5	39.4	0.39	9.9

*Simulated values

Typically, there are three configurations for the electrostatic harvesters based on how the capacitance changes with the motion. Figure 2-2 shows these typical configurations including in-plane overlap type, in-plane gap closing type, and out-of-plane gap closing type [1]. Table 2.4 is a recent comparison of the reported MEMS electrostatic energy harvesting devices.

Several novel electrostatic energy harvesters have been developed within the last few years. Naruse et al. developed an electrostatic micro power generator for low-frequency energy harvesting applications [40]. The reported electric power can be as high as $40\mu W$ at very low frequency vibration (2Hz) and the device dimensions are 20 mm 45 mm. Yang et al. proposed a MEMS capacitive energy harvester based on in-plane rotary combs [16]. The device is fabricated in SOI (silicon-on-insulators) wafers and the maximum electrical output power of $0.39\mu W$ is reported at 0.25g. However, due to the difficulties mentioned above, other two types of vibration energy harvesting seem to be more practical for real applications.

2.2.2 Electromagnetic Energy Harvesting

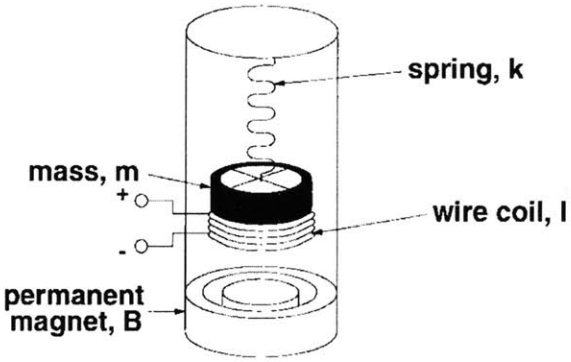

Figure 2-3: The mechanical schematic of a typical electromagnetic energy harvester [4].

Electromagnetic energy harvesting is basically similar to the mechanism used in large-scale generators. It is based on the relative motion of an electrical conductor in a magnetic field due to the vibration. This relative motion between the coil and magnetic field induces an electric current which flows in the coil based on the Faraday's law of induction. Typically a coil is used as the conductor to increase the electric current. The basic concept of EM energy harvesting is well demonstrated by Amirtharajah and Chandrakasan [4] as shown in Figure 2-3. Figure 2-4 depicts the structure of a more recent EM energy harvester developed by Marioli et al. [5].

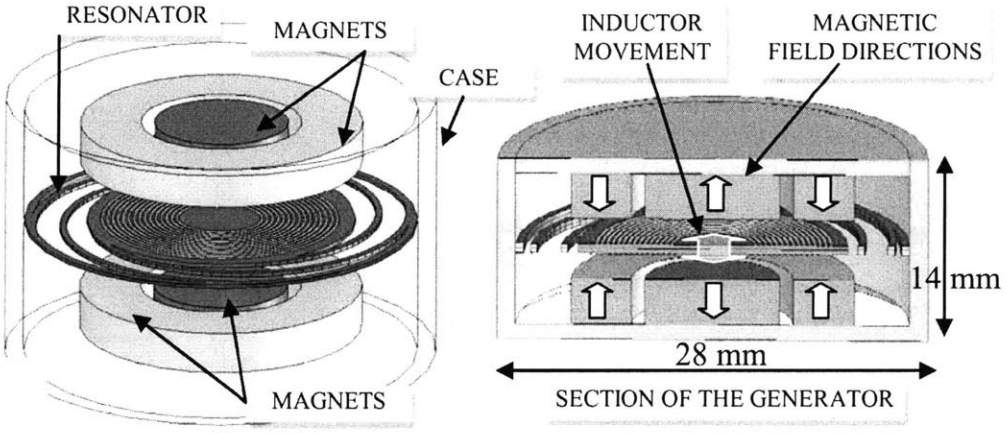

Figure 2-4: The structure of a typical electromagnetic energy harvester [5].

As listed in Table 2.3, EM energy harvesters have a significant advantage compared

Table 2.5: Summary of electromagnetic energy harvesters. (from [17]).

Reference	Power (μW)	Frequency (Hz)	A_{ex} (m/s^2)	Vol. (mm^3)	Material
Shearwood [19, 20]	0.3	4400	382	5.4	GaAs Polyimide
Amarithajah [4]	400*	94	-	-	Discrete components
El-hami [21]	530	322	-	240	Steel
Mizuno [22]	0.4e-3	700	12.4	2100*	Silicon
Glynne-Jones [23]	180	322	2.7	840	Steel
Perpetuum [24]	4000	100	0.4	30000	Steel
Kulah [25]	2.5*	11400	-	4	Silicon/parylene
Huang [26]	0.16	100	Finger tap	-	Copper
Rodrguez [27]	1.44	400	-	250	Polyimide
Beeby [28]	0.5	9500	1.92	-	Silicon
Li [29]	10	64	16.16*	1000	Copper/brass
Ching [30]	830	110	95.5*	1000	Copper/brass
Scherrer [31]	7000	35	-	9000	LTCC/Be/Cu

Simulated values.

to the electrostatic generators: no voltage source is required to start the process. Furthermore, the moving parts in an EM generator do not have any contact and the whole system can be packaged at a very low damping level. This property can be referred as another technical merit of the EM generators in general.

Nevertheless, EM generators suffer from three main problems compared to the other two methods. Although the current density can be very high, the induced voltage is limited to hundreds of Millivolts. This voltage level is too low for real applications and should be boosted before rectification to power typical electronics. In addition, EM generator structure requires large out-of-plane motion and also a bulky magnetic structure. In addition, inevitable assembly makes the production cost very high in comparison to monolithic MEMS. These two requirements make it very difficult to implement an EM energy harvesting in MEMS-scale.

2.3 Piezoelectric Energy Harvesting

Piezoelectric energy harvesters (PEHs) exploit the piezoelectric effect in converting mechanical energy into electrical energy. A resonator converts the mechanical motion into the strain in a beam or diaphragm. The mechanical strain is converted into electrical charge in the piezoelectric material. Piezoelectric energy harvesting can provide a very high power density (up to $3.6W/cm^3$ as explained in Section 3.1), high output voltage (2-10V), and can be implemented in MEMS-scale. Thereby, piezoelectric energy harvesting has become the most promising MEMS-scale energy harvesting approach and attracted a lot of attention from academic and industrial sectors. This work has been based on the piezoelectric energy harvesting; hence, the piezoelectric effect and energy harvesting will be investigated in more detail in the following sections.

2.3.1 Piezoelectricity

The piezoelectric effect couples electric fields to elastic deformation or strain. The energy conversion process works in either the forward or reverse direction:

- Mechanical strain within the piezoelectric material establishes an electric field in the material. A piezoelectric transducer that works in this mode is working in the sensor mode.

- The application of a voltage across the material will induce a mechanical strain in the actuation mode. In case of piezoelectric energy harvesting systems, we employ the piezoelectric effect in the sensor mode to generate electrical charge from elastic strain in the material.

The first demonstration of the direct piezoelectric effect was in 1880 by the brothers Pierre Curie and Jacques Curie. The converse effect was mathematically deduced from fundamental thermodynamic principles by Gabriel Lippmann in 1881 [6].

Perovskite phase

The electromechanical coupling in piezoelectric materials arises from charge asymmetry in the basic repeating cell of the crystal lattice. This spontaneous polarization is further exaggerated as the cell is flexed, twisted, or compressed, developing a potential difference across the crystal structure. The piezoelectric effect is particularly strong in ABO_3 perovskite type materials, including Barium Titanate ($BaTiO_3$), Lithium Niobate ($LiNbO_3$), and lead zirconate titanate $Pb(Zr,Ti)O_3$ (PZT) which has been used in this research. PZT is the most common piezoelectric ceramic and it is being widely used in sensors and actuators due to its remarkable piezoelectric properties.

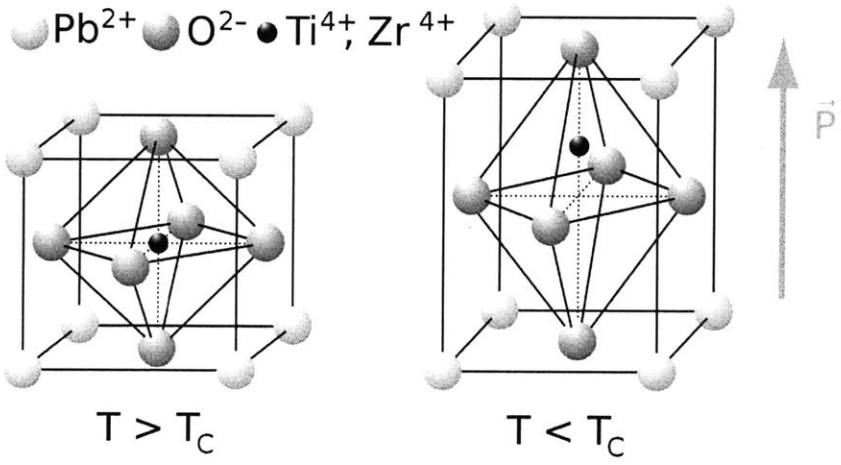

Figure 2-5: perovskite crystal structure: left) above Curie point cubic lattice, symmetric arrangement of positive and negative charges, right) below Curie point tetragonal (orthorhombic) lattice, crystal has dielectric dipole. [6]

A perovskite crystal has a tetragonal/rhombahedral structure very close to a cubic. Its charge asymmetry results from the displacement of a small tetravalent center ion, such as titanium or zirconium, from the surrounding lattice formed by a divalent metal ion such as lead. The cubic (unstrained) and tetragonal (strained) forms of the perovskite crystal phase are shown in Figure 2-5.

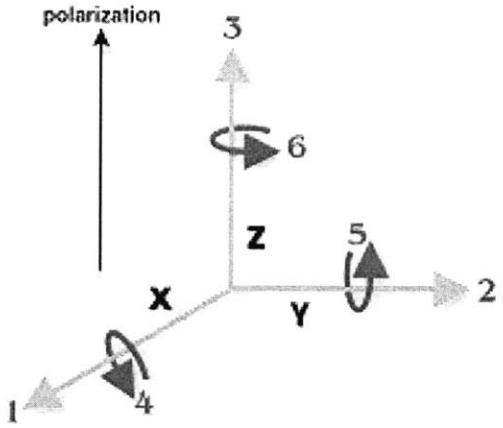

Figure 2-6: Direction conventions for PZT: direction of positive polarization coincides with Z-axis [7]

Constitutive equations

The mathematical nature of electro-mechanical coupling in the piezoelectric is described by the material's constitutive equation, which takes the form:

$$S = s_E.T + d^t.E \tag{2.1}$$

$$D = d.T + \epsilon_T.E \tag{2.2}$$

where the state variables T, D, S, and E represent the material stress, charge-density displacement, strain, and electric field, and ϵ is the material permittivity. The matrices d and s_E contain the material's piezoelectric and compliance constants.

Because a piezoelectric ceramic is anisotropic, physical constants relate to both the direction of the applied mechanical or electric force and the directions perpendicular to the applied force. Consequently, each constant generally has two subscripts that indicate the directions of the two related quantities, such as stress (force on the ceramic element / surface area of the element) and strain (change in length of element / original length of element) for elasticity.

The direction of positive polarization usually is made to coincide with the Z-axis of a rectangular system of X, Y, and Z axes (Figure 2-6). Direction X, Y, or Z is represented by the subscript 1, 2, or 3, respectively, and shear about one of these axes

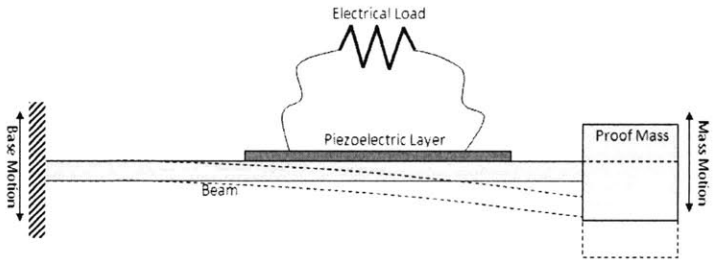

Figure 2-7: Linear piezoelectric energy harvesting scheme based on a simple cantilever

is represented by the subscript 4, 5, or 6, respectively. It is notable that orthogonal deflection in d_{31} mode is not a direct effect of piezoelectricity, but rather an effect of the material's tendency to conserve volume as deflects in the out of plane direction and it is almost half of the d_{33} value.

2.4 Cantilever beam design

Conventional piezoelectric energy harvesting devices use a simple cantilever structure with a proof mass. (Figure 2-7). There is a layer of piezoelectric material (e.g. PZT) mounted on top of the beam. The ambient vibration will be transferred to the device as the oscillating motion of its base. Consequently, the beam will be forced to vibrate as a result of the base excitation.

The beam bending results in alternating strain between tension and compression in the PZT layer. As a result, the PZT layer generates oscillating charge which should be rectified after collected from the electrodes. The generated power is proportional to the square of the induced strain at the PZT layer; hence, a good design should enable large enough strain at the piezoelectric layer.

d_{31} and d_{33} modes

Two piezoelectric modes (d_{31} and d_{33}) are commonly used in piezoelectric devices. They are distinguished by whether the electric field direction is perpendicular to the input strain direction (d_{31}) or parallel to it (d_{33}). d_{31} mode has been traditionally implemented in most of energy harvesters in which the electrodes span both the top

and bottom surface of the piezoelectric strip. To implement d_{33} mode, interdigitated electrodes span one surface of the PZT thin film, and polarization wraps from one electrode to the next in alternating directions. The d_{33} mode eliminates the need for a bottom electrode and gives much higher open-circuit voltage than the d_{31} type transducer at similar beam dimensions [10]. Devices that utilize these two modes are shown schematically in Figure 2-8.

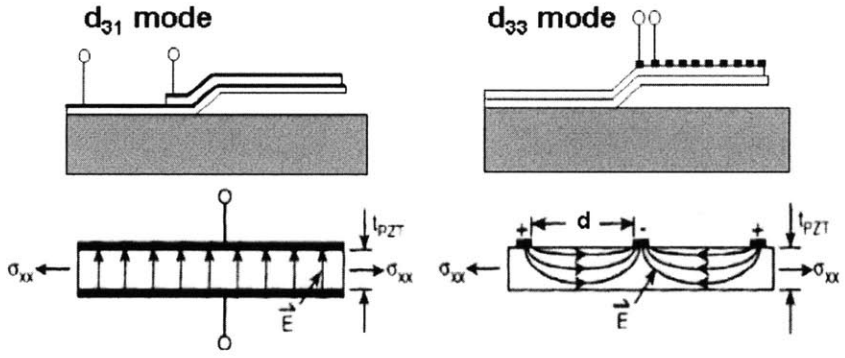

Figure 2-8: d_{31} and d_{33} modes in PZT thin film [8]

2.4.1 Previous Works

Several bulk piezoelectric generators have been developed and reported [17]. Mide Technology Corporation has developed a chain of Quick Pack, or bulk piezoelectric devices [77]. They are two layer bimorph devices that are designed for bending operation, and generate voltage when strained using d_{31} mode. They are constructed from four piezoceramic wafers embedded in a Kapton and epoxy matrix.

Other bulk size piezoelectric generators have also been developed. A study at MIT Media Lab constructed a shoe generator, by placing a sandwiched structure of metal midplate and two PZT unimorph layers on the sole of a shoe (Figure 2-9) [9]. Such shoe insert is capable of generating 8.4 mW of power in normal walking condition. Paul Wright group of UC Berkeley has constructed a power generator for RF transmitter using two layer piezoelectric bender mounted as a cantilever beam [1]. Such device has a total length of 3 cm and maximum power output of $375\mu W$ at 60

Figure 2-9: Parasitic power shoes project at MIT Media Lab (from [9])

Hz with driving vibration of $2.25m/s^2$ (Figure 2-10).

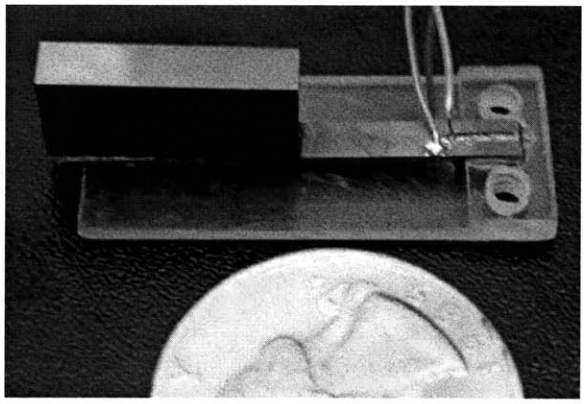

Figure 2-10: Picture of bulk piezoelectric energy harvester developed by Roundy et al. at UC Berkeley (from [1]).

However, most of these devices are too bulky for system integration. Power generator remains the largest part in a sensor node. Furthermore, these devices uses d_{31} mode which is not as efficient as d_{33} mode due to a lower coupling factor. The first d_{33} thin film piezoelectric energy harvesting device, known as "Piezoelectric Micro Power Generator" was fabricated at the MEMS scale in our lab (Micro and Nano Systems Lab, MIT) in 2005 [10]. Several other MEMS-scale piezoelectric energy harvesters have been reported within the last few years. Table 2.6 lists some of the reported piezoelectric harvesters and their specifications. The table is an updated version of

Table 2.6: Summary of piezoelectric energy harvesters. (updated from [17]).

Reference	$P(\mu W)$	$F(Hz)$	$A(m/s^2)$	Volume (mm^3)
Kymissis98 [9]	1300	0.9	-	16000*
Shenk01 [42]	8400	0.9	N/A	25000*
Ramsay01 [43]	2.3	1	-	1.1
White01 [44]	2.1	80.1	2.3*	125
Roundy03 [1]	375	120	2.5	1000
Sodano04 [45]	11.9	30	-	1947
Duggirala04 [46]	0.001	35	N/A	60*
Bayrashev04 [47]	80	5	N/A	2185
Marzencki05 [48]	0.6	900	9.81	2
Jeon05 [10]	1	13900	106	0.027*
Van Schaijk08 [49]	10	1155	80	2
Kim08 [50]	1.13	870	NA	3.75
Shen08 [51, 52]	2.15	462.5	19.6	0.652
Kok09 [53]	40	100	15	NA
Park09 [54]	1.1	528	0.39	0.95
Shen09 [55]	0.32	184	7.5	0.77
Lee09 [56]	2.765	260	25	0.375
Elfrink09 [57]	60	572	20	NA
Muralt09 [58]	1.4	870	20	0.50
Morimoto10 [59]	5.3	126	5	4.62
Park10 [60]	6.72	127	NA	0.16

the list reported in [17].

Recently, there has been a high interests in piezoelectric energy harvesting and extensive research and development have been carried out in this area. Several review articles have been published within the last few years that can be referred [78–86]. Anton and Sodano reviewed the piezoelectric energy harvesting developments from 2003 to 2006 [61]. This paper reviews the efficiency improvement through piezoelectric configurations including the choice of material, geometry and structure. The second part of the paper studies new methods of improvements by modifying the power harvesting circuitry and storage medium. In addition, the possibility of employing the piezoelectric energy harvesting as implantable and wearable power supplies has been investigated. Harvesting the mechanical energy from ambient fluid flows like wind energy or flowing water through piezoelectric harvester is another opportunity that has

been studied. Subsequently, the possibility of implementing the piezoelectric energy harvesting in small scale using micro-electromechanical systems (MEMS) especially to power wireless sensors has been presented. Finally, the efficiency of piezoelectric energy harvesting has been compared with other methods.

Beeby et al. reviewed the state-of-the art in vibration energy harvesting for wireless self-powered microsystems in 2006 [17]. Farmer has compared various power harvesting techniques including piezoelectric, thermoelectric, photovoltaic, electromagnetic and also hybrid systems [87]. A more recent review of the energy harvesting techniques, power conversion, power management, and battery charging can be found at [74], but it is very limited and incomplete. Park et al. reviewed the development of energy harvesting for low-power embedded structural health monitoring (SHM) sensing systems [88]. Furthermore, Sastry et al. reviewed the possible non-regenerative and regenerative power supplies for MEMS portable devices [89]. The review includes an overview of strategies for powering MEMS via energy harvesting techniques and also the fundamentals of piezoelectric energy harvesting, along with recent advancements.

In addition to the device structure, several studies have investigated the effect of piezoelectric material properties on the performance of PEH. Novel piezoelectric materials have been proposed as alternatives to PZT in PEH. Shen et al. compared three favorite piezoelectric materials including PZT, Polyvinylidene fluoride (PVDF) copolymer, and Macro Fiber Composite (MFC) for energy harvesting applications [90]. The power density of the PZT prototype is shown to be about 200 times higher than the other two in experiment.

Majidi et al. suggested the possibility of a shear-mode piezoelectric energy harvesting with ZnO nanoribbons, but the power generation density is limited to about 10 nW/mm^3 which is pretty small compared to that of PZT [91]. Song et al. investigated the performance of an energy harvester utilizing a single crystal lead magnesium niobate-lead titanate (PMN-PT) material [92]. The maximum DC power generated of 19 μW is reported for an excitation of 0.2g (power density of 0.73 mW/cm^3). Mathers et al. reported a vibration-based piezoelectric energy harvester made of a

Table 2.7: Coefficients of common piezoelectric materials. (from [17]).

Property	$PZT-5H$	$PZT-5A$	$BaTiO_3$	$PVDF$	AlN
$d_{33}(10^{-12}C/N)$	593	374	149	33	5.5
$d_{31}(10^{-12}C/N)$	274	171	78	23	3
$g_{33}(10^{-}3Vm/N)$	19.7	24.8	14.1	330	69
$g_{31}(10^{-}3Vm/N)$	9.1	11.4	5	216	37.6
k_{33}	0.75	0.71	0.48	0.15	0.33
k_{31}	0.39	0.31	0.21	0.07	0.18
Relative permittivity (ϵ_r)	3400	1700	1700	12	9

composite cantilever of a single crystal PMN-PT, PDMS base layer and also PDMS proof mass [93]. The harvester with a size of $7.4mm \times 2mm \times 110\mu m$ outputs a voltage of 10 V (0.3 mW power) under a base motion of 0.5mm at a frequency around 1.3 kHz. Nevertheless, this base motion corresponds to an acceleration level of 3000g which is not practical.

In addition, several articles have been investigated various aspects of piezoelectric energy harvesting. Prof. Inman at Virginia Tech and many other researchers have done a lot of theoretical studies on the PEH [63, 94–96]. Other researchers are investigating new applications such as implantable devices for piezoelectric energy harvesting. The possibility of a stimulated muscle powered piezoelectric generator system for extending the life of the batteries of implanted electronic devices has been studied by Lewandowski [97]. Saha et al. studied the possibility of harvesting energy from human motion using an electromagnetic generator [98]. Guan and Liao compared the performances of supercapacitors and rechargeable batteries as energy storage devices in the piezoelectric energy harvesting systems [99].

2.4.2 Type I: Piezoelectric Micro Power Generator

The first PMPG device was is designed for high-frequency applications and fabricated according to the layout shown in Figure 2-12 based on thin-film spin-coated PZT. The MEMS device is built on a Si substrate, which is later etched away to release the cantilever beam. The basic design of the multilayer cantilever consists

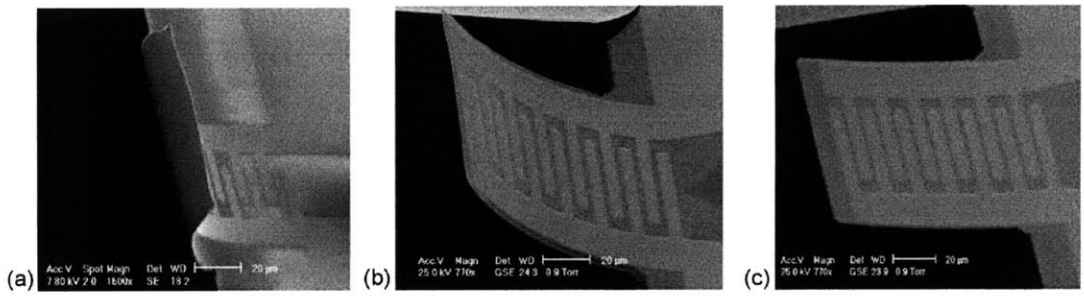

Figure 2-11: Type-I piezoelectric energy harvester (PMPG): SEM images of the stress-controlled cantilevers consisting of (a) PZT/ZrO2/SiO_2(thermal), (b) PZT/ZrO_2/SiO_2(PECVD) and (c) PZT/ZrO_2/SiO_2(PECVD)/SiN_x (from [10])

of five layers as follows: membrane layer (SiO_2 and/or SiN_x) for controlling bow of the cantilever structure, diffusion barrier/buffer layer (ZrO_2) for preventing electrical charge diffusion from the piezoelectric layer, piezoelectric layer (PZT), top IDT electrode (Pt/Ti), and optional proof mass layer (SU-8). Pt is the dominant material of the top electrodes, while Ti acts as an adhesion layer between Pt and PZT. The IDT electrodes are employed to take advantage of d_{33} mode of PZT material and generate much higher output voltage compared to conventional d_{31} mode.

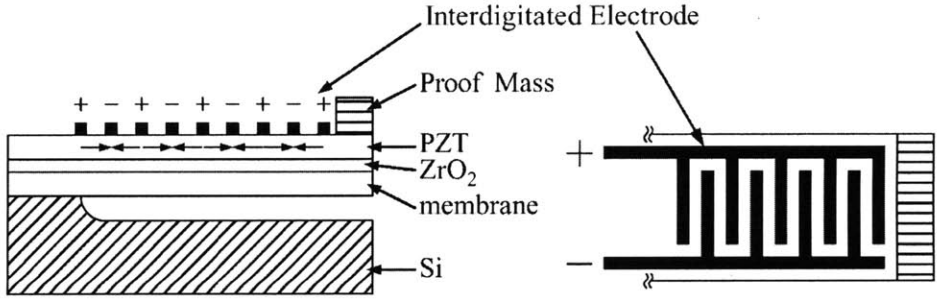

Figure 2-12: Schematic of the type-I PMPG structure based on d_{33} piezoelectric mode. (from [10])

Conventionally, it has been tried to match the natural frequency of the system to the frequency of parasitic vibration as much as possible and minimize the damping to achieve maximum power. However, considering that the bandwidth of the system is inversely proportional to the system's quality factor, the bandwidth of the high Q systems is extremely small and the system's robustness hasn't been taken into consideration. The power of low-damped PMPG will be dropped sharply up to less

than 1% of nominal value by a slight change in the excitation frequency.

Problem Description

Subjected to the external vibration, the cantilever beam vibrates and deforms as a result of inertial force exerted on the proof mass. The strain in PZT layer, originated from the beam's deflection, generates electrical charge in the form of an oscillating AC signal. In order to maximize the power, low-damped high-Q designs at resonance have been desired and pursued. Nevertheless, there are some intrinsic problems associated with this approach.

Bandwidth and Robustness

Linear systems suffer from gain $\times$ bandwidth limitation. It means employing high-Q design to improve the generated power results in a very narrow frequency bandwidth. Nevertheless, we cannot assume the input ambient vibration of the harvesters to be at a constant single frequency except in rare cases such as the vibration from electrical motors. Consequently, the generated power drops drastically from design value for small variations in the excited frequency. In addition, linear energy harvesters lack the robustness required for practical applications. The response is highly sensitive to the changes in the Q-factor (due to any change in mechanical damping or electrical load) and vibration condition (amplitude and frequency).

Power Density

The generated power density of the reported linear harvesters have been very small. Piezoelectric energy conversion should be able to provide very high power-density in theory. Its maximum limit is proportional to the excitation frequency, piezoelectric coefficient and the square of the strain (can be as high as 0.1%-0.2% before mechanical failure). Nevertheless, bending strain in the traditional cantilever structure is much smaller than the yield strain. In addition, cantilevers suffer from nonuniform

strain distribution. Bending in simple cantilever beam generates a non-uniform strain distribution across the beam's thickness and length (for rectangular cross-sections). Hence, the generated power density in cantilever-based piezoelectric energy harvesters is few orders of magnitude smaller than the maximum theoretical value.

2.5 Discussion and Motivation

There have been a few attempts to resolve some of these issues. To better match the electrical damping to the mechanical damping, Challa et al. have coupled a piezoelectric energy harvester to an electromagnetic harvester [100]. The coupled device generated a peak power of $332\mu W$ at the resonance frequency of 21.6Hz. The system is bulky (weights about 80 grams) and shows very limited power density ($9.5\ \mu W/cm^3$). Shahruz proposed improving the bandwidth of piezoelectric energy harvesting by employing a mechanical band-pass filter consisting of multiple benders with different geometries [68]. Similarly, an array of MEMS-based piezoelectric beams with different lengths has been developed by Liu et al. to improve the bandwidth [11]. The measured output power from the serial connection of the beams is about $3.98\mu W$ at 229Hz. Figure 2-13 shows the system which has been microfabricated by RIE and back silicon wet etching in KOH. Metal mass has been externally assembled to the beams [101].

Wischke et al. have tried to tune the resonance frequency of an electromagnetic vibration harvester by applying DC electric field and exploiting the elastostriction [102]. Mann and Sims investigated a novel energy harvester that use magnetic levitation to produce an oscillator with a tunable resonance [69, 103–106]. The form of equations is similar to a Duffing oscillator and nonlinear resonance is exploited to improve the bandwidth. Kulah and Najafi have tried to improve the efficiency of energy conversion from low-frequency vibrations by up-converting the vibrations with a mechanical frequency conversion technique [107].

In conclusion, no practical solution has been proposed up to this point and a totally new approach still seem to be required. In this work, we are trying to address

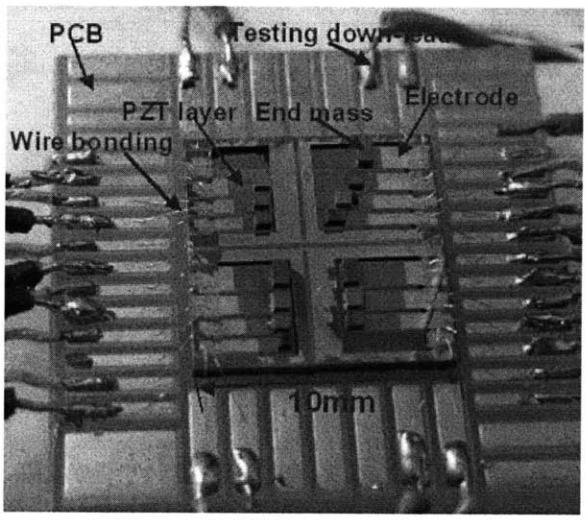

Figure 2-13: Picture of power generator prototype based on an array of cantilever beams (from [11])

these issues by presenting a simple but effective new design. This novel design is based on exploiting the stretching strain in doubly-clamped beams [70].

Recently, Marinkovic and Koser have employed a similar approach to our method to improve the bandwidth through the stretching strain in the doubly-clamped beams in a device called 'smart sand' [108]. They have developed an FEM model of the device and also developed a prototype based on SOI wafer. Initial prototype demonstrated operation between 160-400Hz. The power generation capability has been estimated based on the PZT model. Nevertheless, in reality the residual stress from the PZT would change the whole dynamics of the stress-free structure. Furthermore, the axis of the tethers do not pass the central axis of the proof mass. Therefore, any deflection will result in a rotational torque which can induce unwanted lateral and rotational motions.

The main objective of this research is to develop a novel piezoelectric energy harvester for practical applications that should have the following main features:

- Robust with large bandwidth to harvest ambient vibration in a wide range of frequencies (100Hz-1000Hz)
- Provides up to $100\mu W$ continuous electric power

- Small-scale, cheap and can be integrated to the wireless sensors

The design, fabrication, and testing of an ultra wide bandwidth MEMS-scale device based on the mentioned idea is proposed and pursued.

Chapter 3

Design and Modeling

3.1 Energy analysis

The basic concept of piezoelectric energy harvesting can be explained in energy domain, as shown in Figure 3-1. Energy analysis can show us the relationship between the harvested power and the design parameters. Ambient vibration injects kinetic energy into the system through the base excitation. The kinetic energy is converted into the potential elastic energy which is stored in the beam in the form of mechanical strain. Part of the elastic energy stored in the piezoelectric material is transformed into the electrical energy in the form of induced charge across the piezoelectric ceramics. This electrical energy can be harvested and dissipated directly in the resistive load or stored in a capacitor for future use. Therefore, a good design should maximize the dissipative electrical energy throughout the cycle for a wide range of frequency to reach a high-power and robust energy harvesting scheme.

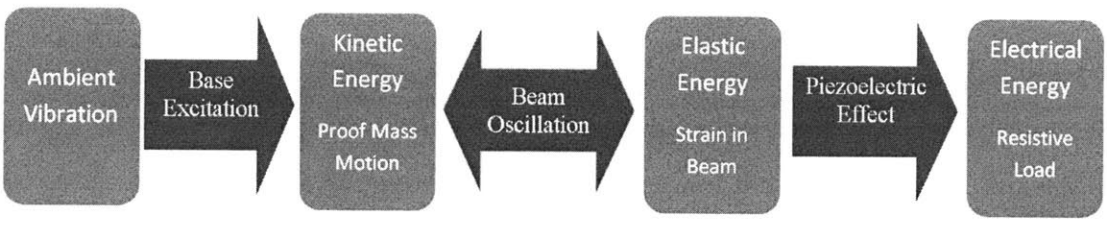

Figure 3-1: Piezoelectric energy harvesting concept in energy domain

The effect of base excitation,

$$\ddot{y}_{ex}(t) = A_{ex} \sin(\omega_{ex} t), \tag{3.1}$$

can be modeled as an external force,

$$F_{ex}(t) = -m_{pm} A_{ex} \sin(\omega_{ex} t), \tag{3.2}$$

applied on the proof mass in which y_{ex}, m_{pm}, A_{ex} and ω_{ex} are the base motion, the proof mass and the excitation amplitude and frequency, respectively. Close to the natural frequency, the linear system shows large gain, $|G(j\omega)| \gg 1$; therefore, we can simply approximate the beam deflection, $\delta = y_{pm} - y_{ex}$, with the linear response of the system, y_{pm}:

$$\delta(t) \approx y_{pm}(t) = |G(j\omega_{ex})| \frac{A_{ex}}{\omega_{ex}^2} \sin(\omega_{ex} t + \angle G(j\omega_{ex})) \tag{3.3}$$

, in which $\angle G(j\omega_{ex})$ is the phase delay. Subsequently, the average rate of kinetic energy that ambient vibration injects into the system can be calculated in each cycle:

$$\begin{aligned} \bar{\dot{E}}_{ex} &= \frac{1}{T}\left(\int_T -m_{pm} \frac{A_{ex}^2}{\omega_{ex}} |G(j\omega_{ex})| \sin(\omega_{ex} t) \cos(\omega t + \angle G(j\omega_{ex}))\, dt\right) \\ &= \frac{m_{pm} A_{ex}^2 |G(j\omega_{ex})| \sin(\angle G(j\omega_{ex}))}{2\omega_{ex}} \end{aligned} \tag{3.4}$$

Conservation of energy means that this energy is partly dissipated in each cycle due to the structural and aerodynamic damping and the rest is transformed into electrical energy via piezoelectric effect. Therefore, to maximize the output power, the electrical damping can be increased in comparison to the other sources of damping. Aerodynamic damping can be reduced by vacuum packaging. Structural damping is proportional to the stored elastic energy and also the properties of the structural material. Consequently, the ratio of the active piezoelectric layer's thickness to the total thickness of the structure should be increased. In other words, by increasing the PZT thickness, more energy can be harvested for a fixed amount of injected kinetic

energy.

In addition, Eq. 3.4 implies that the generated power is proportional to the linear gain, $|G(j\omega)|$, and subsequently high Q (low damped) design is desirable. However, the bandwidth is inversely proportional to the gain,

$$\frac{\Delta\omega}{\omega_n} = \frac{1}{Q}, \tag{3.5}$$

and power drops sharply for small deviation of excitation from the resonance. In other words, linear systems suffers from gain×bandwidth limitation which prohibits the use of linear harvesting systems from practical applications. The linear gain, $|G(j\omega)|$, known as the systems transmissibility for various damping coefficient is shown in Figure 3-2.

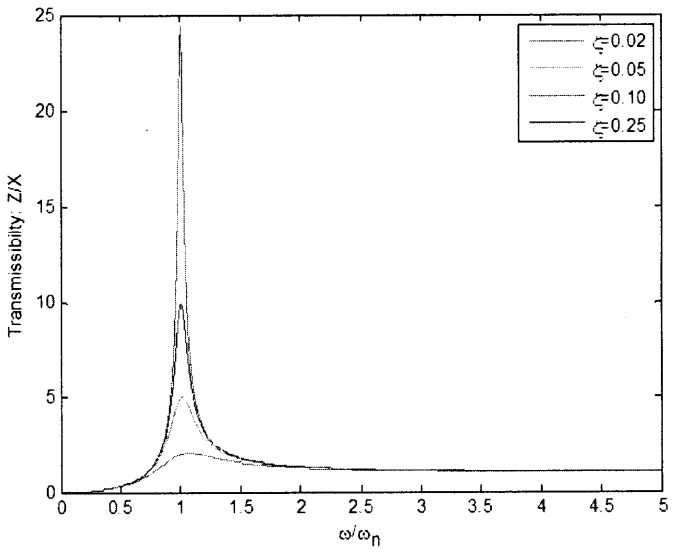

Figure 3-2: Transmissibility of a linear resonator as a function of its damping ratio shows gain × bandwidth limitation dilemma in linear systems

In an optimum case, a device should employ the maximum energy density of the piezoelectric material. For the case of PZT, it can safely function up to 0.1%-0.2% strain without significant fatigue and degradation. Consequently, we can find the

Table 3.1: Typical properties of PZT.

Young's Modulus Y	$60GPa$
Dielectric Constant ϵ_r	1700
Piezoelectric Coefficient d_{33}	$300 \times 10^{-12} m/V$
Maximum Strain S_{max}	0.1%
Coupling Coefficient k_{33}	0.60
Maximum Electrical Power Generation Density $\bar{\dot{e}}_{e,max}$	$3.6W/cm^3$

maximum electrical power generation density of PZT:

$$\bar{\dot{e}}_{e,max} = Y_{PZT} S_{max}^2 f_{ex} k_{33}^2, \tag{3.6}$$

in which Y_{PZT}, S_{max} and f_{ex} are the Young's modulus of PZT, maximum allowable strain, excitation frequency, respectively. Also, the coupling factor, defined as

$$k_{33}^2 = \frac{Y_{PZT} d_{33}^2}{\epsilon_{PZT}}, \tag{3.7}$$

is an indicator of the effectiveness with which the piezoelectric material converts mechanical energy into electrical energy. Accordingly, the maximum electrical power generation density of a typical PZT material at 100Hz would be considerably high (Table 3.1).

3.2 Redesign

Initially, an extensive study on different designs has been conducted to achieve a system that can offer all the aforementioned required properties.

3.2.1 Quality Factor

The effect of system's damping and the likelihood of implementing systems with lower quality factors that can provide a wider bandwidth without sacrificing the power was also investigated. As explained in Section 3.1, the maximum power is achieved at the

excitation frequency matched to the systems natural frequency. Furthermore, it is also proportional to the quality factor (Q) or inversely proportional to the damping of the system. However, the bandwidth of the system is inversely proportional to the systems quality factor. Therefore, the generator should be designed with a natural frequency as close as possible to the excitation frequency to achieve higher power if the excitation frequency is fixed or can be predicted..

Nevertheless, the selection of system's damping is more complicated. More power is achievable for a low-damped system, but a narrow bandwidth would limit the use of this system for widely varying input vibrations. Therefore, the possibility of achieving the maximum allowable strain (0.1%-0.2% strain for PZT) at a lower Q-factor was investigated. It can be shown that the maximum strain of a cantilever beam is proportional to (t/L^2):

$$\frac{t}{L^2} = \frac{|S_{max}|\omega_n^2}{QA_{ex}} \tag{3.8}$$

Therefore, (t/L^2) should be increased to achieve the maximum strain. The length for which the maximum allowable PZT strain (0.1%) is achieved is plotted versus the beam thickness for different Q-factor (Figure 3-3). It implies that it is possible to reach maximum power with a wider bandwidth by smartly choosing the geometry of the beam (large t/L^2). Increasing the thickness will increase the bending stiffness which is proportional to (t^3/L^3). Nevertheless, to keep the natural frequency constant, the proof mass should also be scaled up proportional to the bending stiffness as shown in Figure 3-4. For beams thicker than $15\mu m$, a proof mass heavier than 10 grams is needed which is not feasible compared to the size of the structure. Consequently, thickness would be limited to about $15\mu m$ considering the limitation on the proof mass. Finally, it is concluded that achieving maximum theoretical power density which requires reaching maximum strain is only feasible at MEMS-scale. That's why all the reported power density that have been reported from bulk piezoelectric harvesters are orders of magnitude smaller than that of MEMS-scale systems.

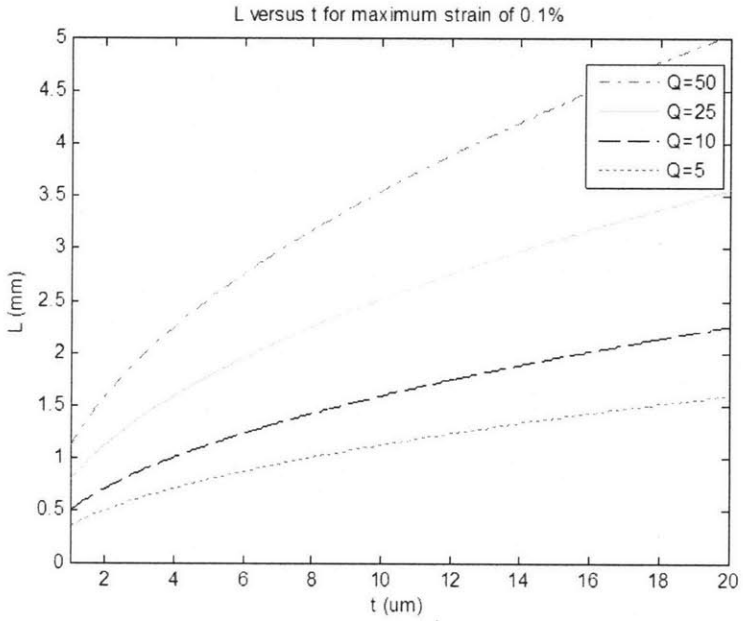

Figure 3-3: Beam length versus its thickness to achieve 0.1% strain at 1g level of acceleration (100Hz) for various Q-factor

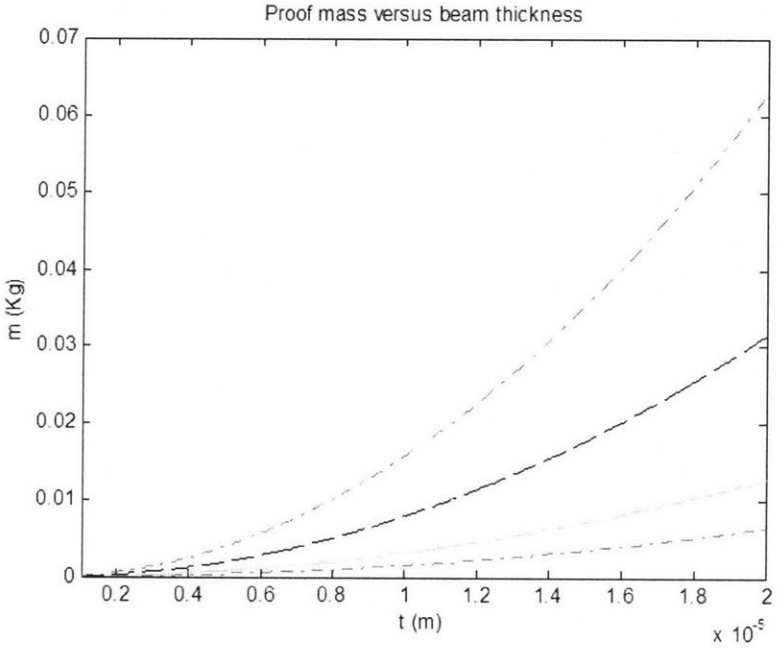

Figure 3-4: The proof mass required to reach 0.1% strain at a constant natural frequency constant (100Hz).

3.2.2 Strain Distribution

The possibility of changing the width of the beam as a function of its length to get a more uniform strain was studied. Unlike rectangular-shaped beams, triangular-shaped cantilevers generates uniform bending strain across its length. As depicted in Figure 3-5, this idea has been recently implemented by Goldschmidtboeing and Woias at IMTEK [12]. They have reported that triangular-shaped beams are more effective than rectangular-shaped ones in terms of curvature homogeneity independent of the proof mass. But, this effect is opposed by the adverse mass distribution and the increased stiffness of triangular-shaped beams. Therefore, the overall efficiency has only weakly influenced by the beam shape. Nevertheless triangular-shaped beams drastically outperform rectangular ones in terms of tolerable excitation amplitude and maximum output power.

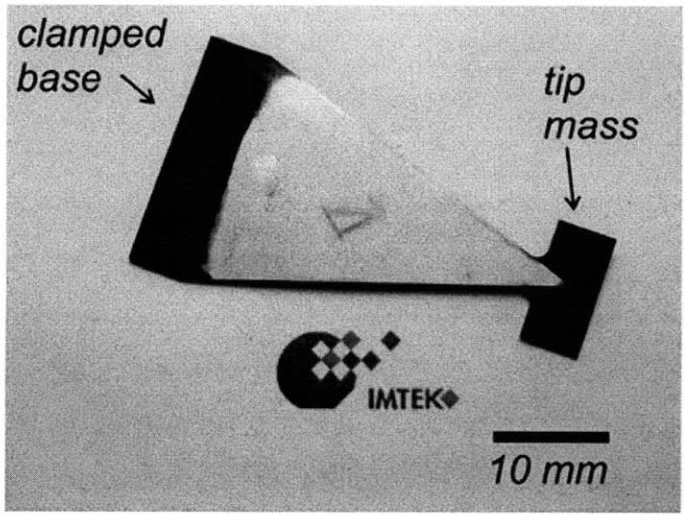

Figure 3-5: tri-angular shaped harvester by IMTEK are more effective than rectangular-shaped beam in terms of strain distribution. [12]

Furthermore, new geometries like spiral beams were considered to increase the effective length of the beam and consequently reduce the natural frequency. However, large deflection may deform the spiral beam in other directions instead of bending mode. Therefore, a tri-spiral beams with a heavy central mass was proposed and analyzed accordingly. Subsequently, the width of the beam was tailored as a func-

tion of angle to achieve uniform strain distribution as shown in Figure 3-6. Further

Figure 3-6: Strain distribution in geometry-optimized tri-spiral design with a heavy central proof mass.

investigation of the tri-spiral design at large deflection mode reveals the stretching mode associated with the doubly-clamped structures. Doubly-clamped structures demonstrate interesting properties such as tensile strain and nonlinear stiffness due to the stretching mode. These properties are explained in next section and a novel pie-shaped structure based on doubly-clamped beams is presented. This new harvester is optimized to tackle all the issues associated with the cantilever-based design simultaneously.

3.3 Doubly-clamped Structures

3.3.1 Stretching vs bending

Consider the large deflection of the proof mass as shown in Figure 3-7. Each beam is clamped between the support and the proof mass. The symmetry of the beams around the proof mass prevents any lateral and rotational motion of the proof mass other than its main translation motion. In case of pure bending (shown in red in Figure 3-7), each beam should have an elongation perpendicular to the proof mass

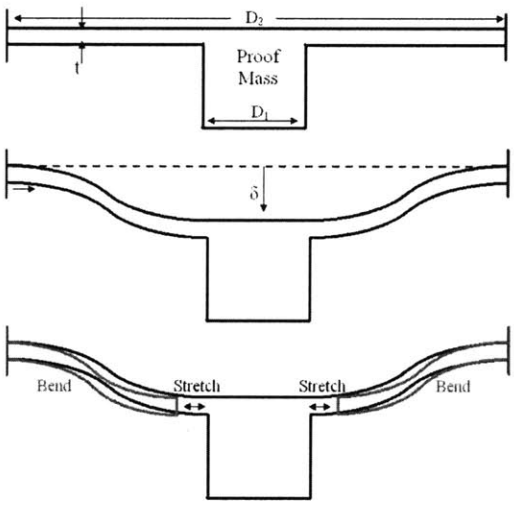

Figure 3-7: Bending vs stretching in a doubly-clamped beam

motion to become geometrically compatible. However, this lateral motion is not allowed by the symmetric proof mass and therefore a stretching force is applied to the beams to compensate their length increase. Consequently, two sources of strain should be included for large deflection of the proof mass: bending strain, S_B, and stretching strain, S_S [71, 109].

$$S_T = S_B + S_S \tag{3.9}$$

As shown in Figure 3-7, the bending strain is not uniform and it varies along the beam. When the proof mass deflects, it generates bending strain that is not uniform and varies across the beams' length and across the thickness with opposite sign in reverse motion. Contrarily, the stretching strain is always tensile and almost uniform across the length and thickness for both upward and downward motion.

3.3.2 Load-deflection Characteristics

To analyze the large-amplitude load-deflection behavior of this beam, we can use variational methods to get approximate solution [109]. We can use a trial function in the form of a cosine:

$$u(x) = \frac{\delta}{2}\left(1 + cos\frac{2\pi x}{L}\right) \tag{3.10}$$

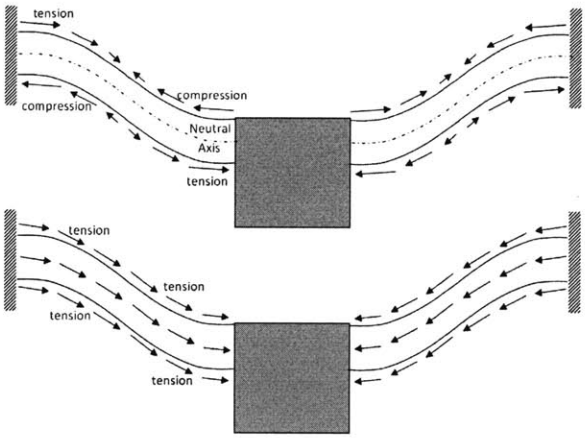

Figure 3-8: Strain distribution in doubly-clamped structures: Bending vs stretching

Accordingly, we can find the total axial strain in the beam as a function of beam deflection:

$$S_T = -z\frac{d^2u(x)}{dx^2} + \frac{1}{L}\int_{-L/2}^{L/2}\frac{1}{2}\left(\frac{du(x)}{dx}\right)^2 dx \tag{3.11}$$

Second term is the average stretching strain in the beam. We can substitute the trial solution of Eq. 3.10 into Eq. 3.11, evaluate the total strain energy, and apply the variational method to reach the load-deflection characteristic of the doubly-clamped beam shown in 3-8:

$$S_S = \frac{\pi^2}{4L^2}\delta^2 \tag{3.12}$$

$$F = \left(\frac{\pi^4}{6}\right)\left[\frac{Ywt^3}{L^3}\right]\delta + \left(\frac{\pi^4}{8}\right)\left[\frac{Ywt}{L^3}\right]\delta^3 \tag{3.13}$$

This is a very interesting result, worthy of close examination. The first thing we notice is that the relation between the virtual applied point load at the proof mass, F, and the resulting deflection δ is nonlinear. Therefore, the doubly-clamped beam can be modeled as an amplitude-stiffened Duffing spring and the dynamic model of the system's motion is nonlinear Duffing equation. Additionally, the response can be divided into two pieces. The first term, linear in δ, is the result of the small-deflection bending, which is proportional to the moment of inertia (i.e. to wt^3). The second term, proportional to δ^3, is the stretching term, which is proportional to wt. Next, it

can be seen that thicker beams will be more likely to be dominated by the bending term, and the thinner ones by the stretching term. Furthermore, the transition from bending-dominated behavior to stretching-dominated behavior occurs when $\delta \approx t$ and the stretching stiffening force dominates the bending stiffness.

In case of PMPG, we can conclude that the system shows linear bending-dominated behavior for high-frequency vibrations which have naturally small amplitude. Nevertheless, large amplitude oscillations at low frequencies transform the PMPG into a highly nonlinear device with stretching-dominated behavior. Contrast to the bending strain which oscillates between tensile and compressive, the stretching strain is always tensile and proportional to the square of the deflection.

Residual stress in doubly-clamped structures

Residual axial stress σ_0 in MEMS-scale clamped structures is of great importance in modifying the axial stress in bending. The most direct way to handling residual stress in the structural analysis is to modify the strain energy from the deformation:

$$\tilde{W} = \int_0^{\epsilon_a} (\sigma_0 + E\epsilon)^2 \, d\epsilon \tag{3.14}$$

Applying the variation method to this new form of the strain energy will result in a new term in load-deflection relationship, Eq. 3.13, due to the residual stress:

$$F = \left\{ \left(\frac{\pi^2}{2}\right) \left[\frac{\sigma_0 wt}{L}\right] + \left(\frac{\pi^4}{6}\right) \left[\frac{Ywt^3}{L^3}\right] \right\} \delta + \left(\frac{\pi^4}{8}\right) \left[\frac{Ywt}{L^3}\right] \delta^3 \tag{3.15}$$

The presence of residual stress directly affects the linear stiffness term. In addition, the linear term is estimated to become stress-dominant when

$$\sigma_0 \approx \frac{Yt^2}{L^2} \tag{3.16}$$

The longer the beam, the more important is the residual stress in determining its bending stiffness. In the limit of large residual stress or very thin and long structures (diaphragms), the structure behaves like a tensional wire. Especially, in case of MEMS

structures like the pie-shaped harvester, the membrane is sufficiently thin (according to the Eq. 3.16) that the bending term may be neglected.

Bi-axial strain

When considering elastic energy in beams, it is sufficient to consider only axial strains. In two-dimensional plates and membranes like the pie-shaped harvester, it is necessary to include the Poisson effects that couple strain in different directions. The subject is fully covered in standard texts on elasticity [110]. Nevertheless, the effect of Poisson ratio can be approximated by replacing Young modulus with plate modulus, $Y/(1-\nu^2)$ and biaxial modulus, $Y/(1-\nu)$, in case of bending stiffness and stretching stiffness, respectively.

$$F = \left\{ \left(\frac{\pi^2}{2}\right) \left[\frac{\sigma_0 wt}{L}\right] + \left(\frac{\pi^4}{6}\right) \left[\frac{Ywt^3}{(1-\nu^2)L^3}\right] \right\} \delta + \left(\frac{\pi^4}{8}\right) \left[\frac{Ywt}{(1-\nu)L^3}\right] \delta^3 \qquad (3.17)$$

3.4 2nd Generation: Pie-shaped Design

A new pie-shaped design is introduced which employs trapezoidal beams forming the perimeter of a common central proof mass (Figure 3-9). This design exploits doubly-clamped beams and therefore is a huge departure from the conventional design which employs simple fixed-free cantilever beams as the resonating structure. Unlike the bending strain which oscillates between tension and compression, this design gives always tensile stretching strain which is a key feature especially in large deflections.

The heavy central proof mass is designed specifically to provide enough strain and scale up the generated power (Eq. 3.4). It also reduces the natural frequency from kHz range which is typical of MEMS structures to few hundreds of Hertz to match the typical spectrum of ambient vibration. Furthermore, the stretching-dominance realization requires a symmetric design in which all the beams coincide at the center of the proof mass to avoid lateral/rotational motions. In addition, the thickness of the beams should be smaller than the deflection amplitude of the beam to achieve

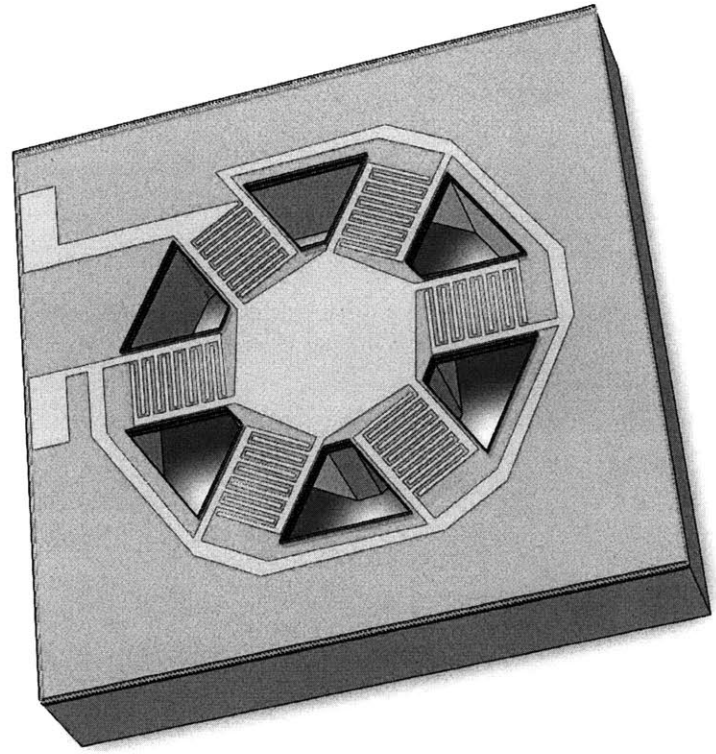

Front side

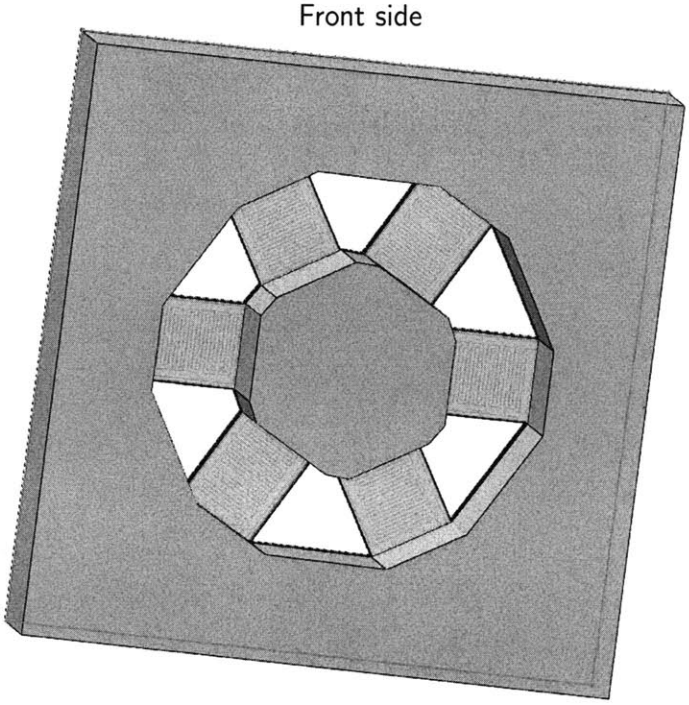

Back side

Figure 3-9: Schematic structure of pie-shaped design with interdigitated electrodes.

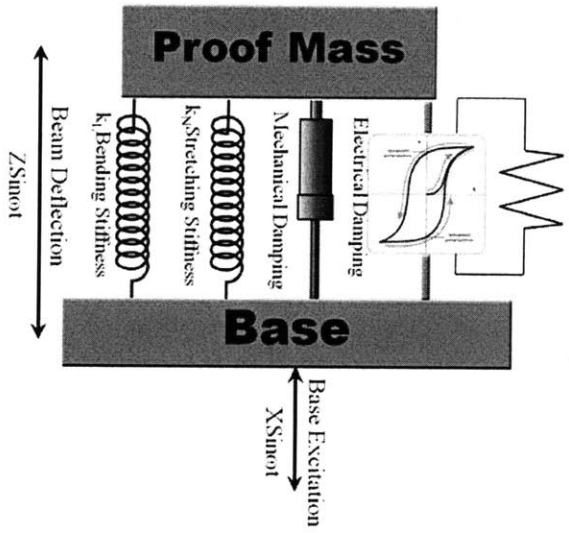

Figure 3-10: Lumped model of the system: a nonlinear stiffness due to the stretching in the doubly-clamped structure is added to the typical linear model

the stretching mode.

3.4.1 Mechanical Model

As depicted in Figure 3-10, all the energy storage and dissipation components can be lumped to obtain a simple single degree of freedom (SDOF) model for further analysis. Nevertheless, the nonlinear stiffness due to the stretching of the beam should be modeled as a nonlinear spring in parallel to the other linear elements. Considering the Eq. 3.15, the lumped parameters are obtained for the pie-shaped device as a function of Young's modulus of the beam (Y_{beam}), beam's thickness (t_{beam}), inner diameter (D_{in}), outer diameter (D_{out}), filling factor ($\eta_{filling}$), mass density of the proof mass ($\rho_{proof\,mass}$) and its thickness ($t_{proof\,mass}$):

$$k_B = \left(\frac{\pi^5}{24}\right)\left[\frac{\left(Y_{Si_3N_x}t_{beam}^3 + 3Y_{PZT}t_{beam}^2 t_{PZT}\right)\left(D_{out}+D_{in}\right)\eta_f}{\left(D_{out}-D_{in}\right)^3}\right] \tag{3.18}$$

is the linear stiffness due to the bending strain in the beam. D_{in}, D_{out}, η_f, $Y_{Si_3N_x}$, Y_{PZT}, t_{beam}, t_{PZT} are inner and outer diameter of the device, filling factor, Youngs modulus of the beam and the PZT layer, and the thickness of beam and PZT, re-

spectively. Moreover,

$$k_{\sigma_0} = \left(\frac{\pi^3}{4}\right)\left[\frac{\left(\sigma_{Si_3N_x} t_{beam} + \sigma_{PZT} t_{PZT}\right)\left(D_{out} + D_{in}\right)\eta_f}{\left(D_{out} - D_{in}\right)}\right] \tag{3.19}$$

is the second linear stiffness term due to the initial residual stress in the beam which is much bigger than k_B in thin-film structures like our case as explained before. The nonlinear stiffness,

$$k_S = \left(\frac{\pi^5}{16}\right)\left[\frac{\left(Y_{Si_3N_x} t_{beam} + Y_{PZT} t_{PZT}\right)\left(D_{out} + D_{in}\right)\eta_f}{\left(D_{out} - D_{in}\right)^3}\right], \tag{3.20}$$

is resulted from the stretching strain in the beams. System's proof mass,

$$m_{pm} = \frac{\pi^2}{4}\rho_{Si} t_{pm} D_{in}^2, \tag{3.21}$$

is formed by the central silicon mass.

$$S_S = \frac{\pi^2}{4\left(D_{out} - D_{in}\right)^2}\delta^2 \tag{3.22}$$

The differential equation of the system's motion in response to the base excitation at acceleration level of A_{ex} and frequency of ω_{ex}would be:

$$\left(k_B + k_{\sigma_0}\right)\delta + k_s\delta^3 + C\left(\dot{\delta}, I_{Load}\right) + m_{pm}\ddot{\delta} = -m_{pm}A_{ex}\sin\omega_{ex}t, \tag{3.23}$$

in which $C\left(\dot{z}, I_{Load}\right)$ shows the total damping force applied on the system [111]. It is a nonlinear function and includes structural damping, $C_{str}\left(\dot{z}\right) = i\eta\left[\left(k_B + k_{\sigma_0}\right)z + k_S z^3\right]$, aerodynamic damping, $C_{aero}\left(\dot{z}\right)$, and electrical damping exerted from the PZT layer due to inverse piezoelectric effect, $F_e\left(z, I_{Load}\right)$ which is proportional to the shunting current across the resistive load. Finally, the right side of the Equation 3.23 shows the excitation force coming from the base vibration at specific amplitude and frequency of A_{ex} and ω_{ex}, respectively.

Ignoring the nonlinear terms, the system's undamped natural frequency can be

derived for very small motion as a function of total linear stiffness, $k_L = k_B + k_{\sigma_0}$:

$$f_n = \frac{1}{2\pi}\sqrt{\frac{k_L}{m_{pm}}} \tag{3.24}$$

However, for large deflections, the nonlinear term of the stiffness becomes dominant and its corresponding stiffness hardening would increase the natural frequency of the system. To approximate the effect of nonlinear terms, the nonlinear stiffness can be modeled as an equivalent linear stiffness that stores equal elastic energy in one cycle:

$$\int_0^{\frac{T}{4}} \left[k_S.\left(\delta sin\left(\omega t\right)\right)^3 - k_{eq}.\delta sin\left(\omega t\right)\right].d\left(\delta sin\left(\omega t\right)\right) = 0 \tag{3.25}$$

which gives us

$$k_{eq} = \frac{3}{4}\delta^2 k_S \tag{3.26}$$

Consequently, an equivalent undamped natural frequency can be defined for a system oscillating at maximum deflection of δ:

$$f_{n,eq} = \frac{1}{2\pi}\sqrt{\frac{k_L + k_{eq}}{m_{pm}}} = \frac{1}{2\pi}\sqrt{\frac{k_L + \frac{3}{4}\delta^2 k_S}{m_{pm}}} \tag{3.27}$$

Similarly, an equivalent linear damping, c_{eq}, can be defined that dissipates the same amount of energy as $C\left(\dot{z}, I_{Load}\right)$ does in a similar cycle:

$$\oint \left[C\left(\dot{z}, I_{Load}\right) - c_{eq}.\delta\omega cos\left(\omega t\right)\right].d\left(\delta sin\left(\omega t\right)\right) = 0 \tag{3.28}$$

The following expression can be used to estimate the equivalent damping considering the damping from bending, stretching and electrical circuit:

$$c_{eq} = c_a + c_s\left(1 + \frac{3}{4}\delta^2\frac{k_S}{k_L}\right) + c_E \tag{3.29}$$

, in which c_a, c_s and c_E shows the linear aerodynamic damping, linear structural damping and the electrical damping resulted from the piezoelectric effect which depends on the circuit side.

Finally, the frequency response of the system is also a function of oscillation's amplitude due to the nonlinearity in the stiffness. Eq. 3.23 can be rewritten in phasor representation as a function of equivalent stiffness and damping:

$$\left(k_L + k_{eq}\right) Z + c_{eq}.j\omega_{ex} Z + m_{pm}.\left(j\omega_{ex}\right)^2 Z = -m_{pm} A_{ex} \tag{3.30}$$

;therefore, the oscillation's amplitude can be calculated:

$$\begin{aligned} \delta &= \frac{m_{pm} A_{ex}}{\sqrt{\left(k_L + k_{eq} - m_{pm}\omega_{ex}^2\right)^2 + c_{eq}^2 \omega_{ex}^2}} \\ &= \frac{m_{pm} A_{ex}}{\sqrt{\left(k_L + \frac{3}{4}\delta^2 k_S - m_{pm}\omega_{ex}^2\right)^2 + \left[c_a + c_E + c_s\left(1 + \frac{3}{4}\delta^2 \frac{k_S}{k_L}\right)\right]^2 \omega_{ex}^2}} \end{aligned} \tag{3.31}$$

Unlike the linear systems, the right side of the equation is also a function of δ. Rearranging the 3.31, a cubic equation with respect to δ^2 can be obtained that may have up to three positive real roots:

$$\begin{aligned} \frac{9k_S^2}{16}\left(1 + \frac{{c_s}^2}{{k_L}^2}\omega_{ex}^2\right)\delta^6 + \frac{3k_S}{2}\left[k_L + \frac{\left(c_a + c_E + c_s\right)c_s}{k_L}\omega_{ex}^2 - m_{pm}\omega_{ex}^2\right]\delta^4 \; + \\ \left[\left(c_a + c_E + c_s\right)^2\omega_{ex}^2 + \left(k_L - m_{pm}\omega_{ex}^2\right)^2\right]\delta^2 - m_{pm}^2 A_{ex}^2 = 0 \end{aligned} \tag{3.32}$$

3.5 Frequency Response

3.5.1 Deflection

Using Eqs. 3.18-3.21, the equivalent proof mass, linear and nonlinear stiffness of pie-shaped structure can be estimated. Subsequently, the cubic equation of motion, Eq. 3.32 should be solved numerically to find the frequency response of the pie-shaped harvester. To demonstrate the concept, the response has been evaluated for the typical design parameters listed in table 3.2.

Figure 3-11 shows the positive roots of the Eq. 3.32 for the pie-shaped structure (at the conditions specified in Table 3.2) as a function of frequency. Drastic changes compared to the frequency response of linear systems can be identified.

Table 3.2: Typical design parameters of pie-shaped energy harvester that has been used in the simulation.

Inner Diameter D_{in}	$2mm$
Outer Diameter D_{out}	$4mm$
Total Thickness t	$2.7\mu m$
Filling Factor η_f	66%
Acceleration Level A_{ex}	$0.5g$
External Proof Mass	$196mg$
Quality Factor Q_0	90
Linear Stiffness k_L	$476N/m$
Stretching Stiffness k_S	$6.4 \times 10^{12} N/m^3$
Total Proof Mass m_{pm}	$200mg$
Linear Natural Frequency f_n	$245.6Hz$

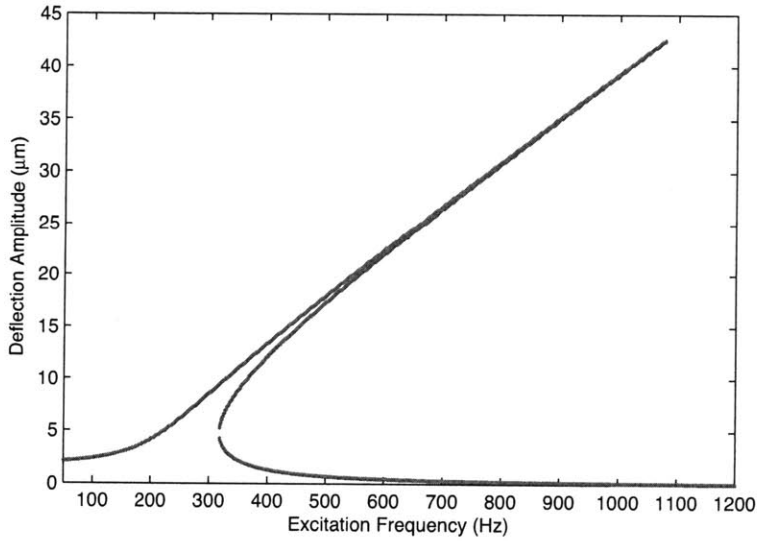

Figure 3-11: Simulated frequency response of the pie-shaped structure.

The sharp peak of resonance is tilted to the right and the amplitude of vibration is increasing steadily from low-frequencies up to about 1100Hz. Furthermore, instead of a single solution, three different roots are available for the frequencies from 350Hz up to 1100Hz. This type of response which is also known as the response of Duffing oscillator shows the result of the nonlinear stretching stiffness on the system dynamics.

3.5.2 Multiple equilibrium points

Nonlinear systems may have multiple equilibrium points which may be stable or unstable. Depending on the initial conditions of the system, the response may converge to one of the stable solutions.

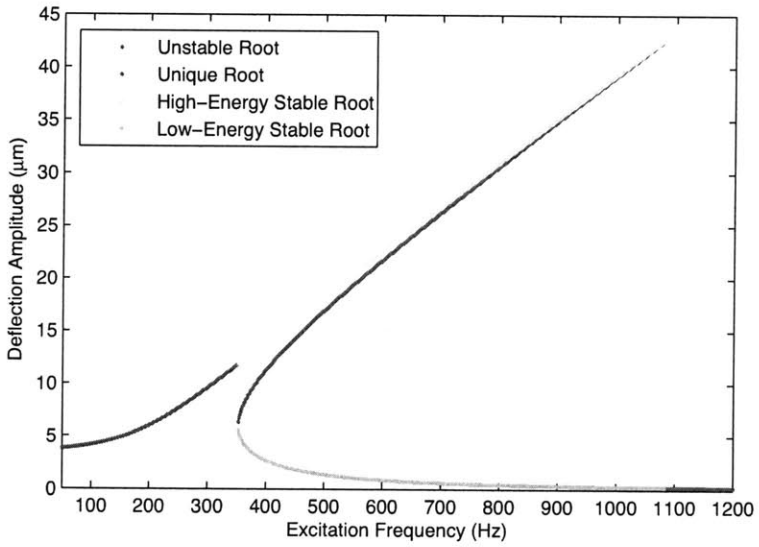

Figure 3-12: Pie-shaped harvester shows unique solution at low frequency and high frequency ranges (red). But more than one equilibrium points is possible in the mid-range frequencies (350Hz-1100Hz): high-amplitude stable response (cyan), unstable response (blue) and low-amplitude stable response (green). Convergence to each of these regions depend on the initial conditions or the excitation pattern.

Various types of equilibrium points are highlighted in Figure 3-12. Red points which span the low-frequency range up to 350Hz and also frequencies higher than 1100 are the unique possible solution of the harvester. Excited harvester at these frequencies will oscillate at the amplitude shown in red color independent of the initial

conditions. Contrarily, three different amplitudes are possible for the oscillation of the harvester in mid-range from 350Hz to 1100Hz. The middle solution, highlighted in blue, can be shown to be the unstable equilibrium point. The system is supposed to stay there as long as there is no perturbation, but in reality the harvester sees a lot of noise and disturbances and this mode cannot be observed.

The harvester has two other solutions which have totally different vibration amplitude. The solution which shows a higher amplitude is shown in cyan and represents the stable points associated with high-energy initial conditions. Furthermore, the harvester will oscillate at a very small amplitude if it converges to the low-energy stable root shown in green. The cyan region is way more desirable than the green region for energy harvesting applications and should be targeted during the operation.

3.5.3 Jump phenomenon

Jump phenomenon is a special effect that occurs only in nonlinear dynamic systems. Subjected to a sinusoidal input, the amplitude of the forced oscillation can jump upward or downward as the input frequency is varied slightly. The graph of the forced amplitude versus the input frequency follows a hysteresis loop and the system's response depends on the past trajectory. More explanation on jump phenomenon can be found in nonlinear dynamic textbooks [112].

As shown in 3-13, this phenomenon can be easily seen in the response of the nonlinear harvester and will impose the physical limitation on the maximum harvestable power at any given conditions. Furthermore, the power bandwidth and the proper performance of the system is highly dependent on the jump effect and will be fully investigated throughout the thesis.

The dash-dotted path shows the response of the system excited by a sinusoid input for which the frequency is ramping up slowly from low frequencies. The amplitude of oscillation is increasing steadily up to about $43\mu m$ at 1100Hz. Afterwards, the high-energy stable response doesn't exist anymore and suddenly the amplitude of oscillation is jumping down to very limited vibration levels which makes the harvester pretty quiet.

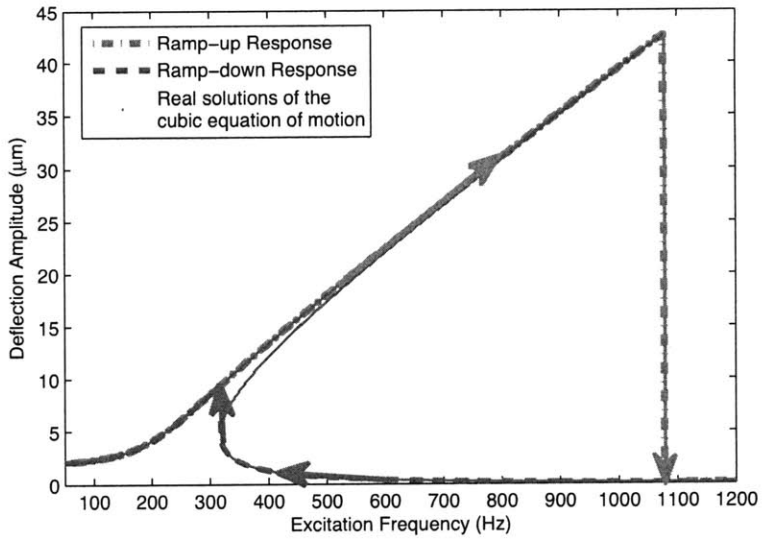

Figure 3-13: Jump phenomenon in ramp-up (green) and ramp down (red) response due to the Duffing nonlinearity.

Now, if the excitation frequency ramps down back to the low frequency range, the solution will follow a totally different path which is shown in dashed line. The harvester will oscillate at the low-energy stable solution amplitude which is much smaller than the ramp-up response. Subsequently, at about 350Hz, the low-energy stable solution is not possible anymore and the system jumps up to the unique solution and oscillation amplitude will suddenly increased to about 12 μm.

3.5.4 Strain vs Frequency

Considering the deflection evaluated in the Figure 3-12, the bending and stretching strain can be evaluated using beam theory [109, 110] and Eq. 3.22. It is assumed that the harvester is excited at its higher energy level at each frequency. Figure 3-14 depicts the trend of each component. Bending strain which is linearly proportional to the deflection increases linearly with frequency up to about 0.03% at 1080Hz and becomes negligible afterward. Stretching strain is a quadratic function of deflection and increases quadratically up to 0.11% at 1080Hz. Furthermore, the stretching term becomes the dominant term after 370Hz or in the high-energy stable solution region.

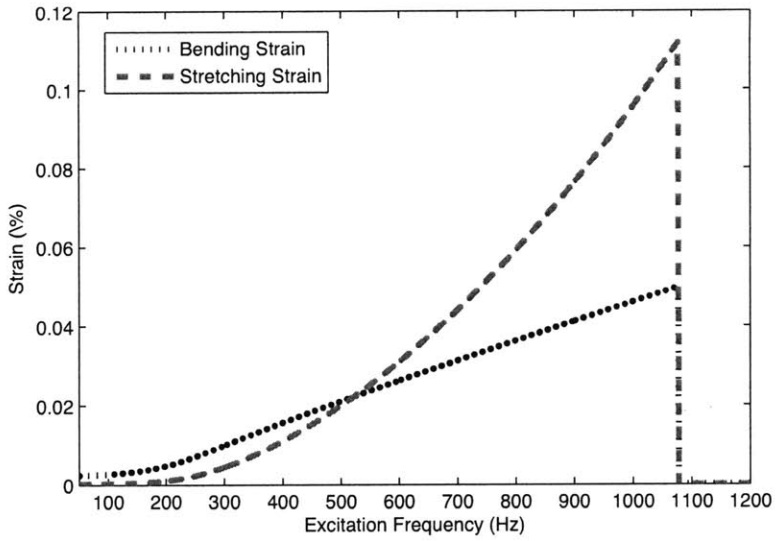

Figure 3-14: Resulting stretching strain versus bending strain in the PZT layer as a function of frequency at a constant excitation amplitude.

3.5.5 Robustness

The nonlinear nature of the harvester enables a large deflection in a wide range of frequency as shown in Figure 3-14. It ensures a considerable energy harvesting power density in a wide range of frequency unlike the linear harvesting schemes which are limited to the resonant frequency. In addition, the system's nonlinearity, which is resulted from the stretching stiffness of the doubly-clamped beams, provides a robust harvesting system in which the output signal is less sensitive to the changes in the amplitude of vibration, mechanical damping and electrical loading. This robustness is extremely desirable for a practical harvester and will be explained here.

Figure 3-15 shows the deflection of the harvester as a function of frequency for different values of excitation amplitudes. As long as the system stays in the high-energy stable region, the deflection is almost constant. It means that the generated electric power which is proportional to the square of the stretching strain will remain almost constant even if the vibration amplitude changes.

In addition, the system shows a similar robustness and insensitivity to the total damping ratio which is defined as the ratio of damping coefficient to the critical

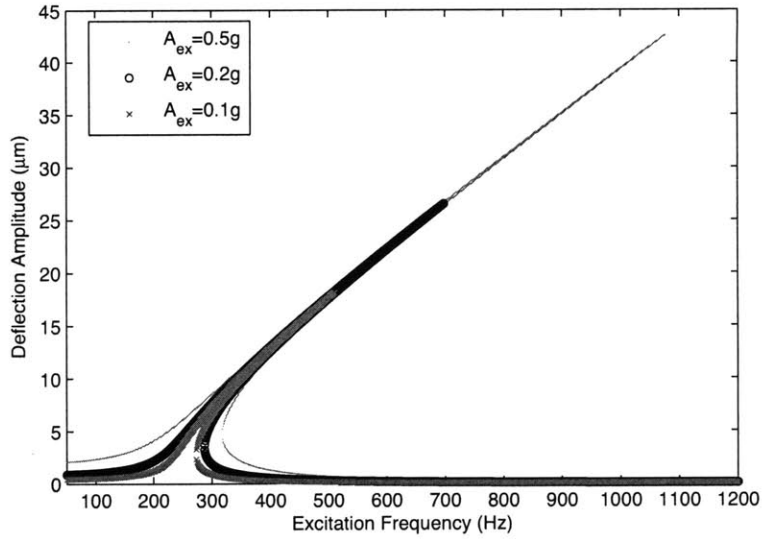

Figure 3-15: The amplitude of vibration is pretty robust to the excitation amplitude as long as it is larger than the jump-down threshold.

damping:

$$\zeta = \frac{1}{2Q} = \frac{c_T}{c_c} = \frac{c_E + c_M}{2\sqrt{k_L m}} \tag{3.33}$$

The damping coefficient consist of mechanical damping, c_M, (including structural damping and aerodynamic damping), and also electrical damping, c_E. The electrical damping is the result of electrical power extraction at the circuit side due to the piezoelectric effect. As shown in Figure 3-16, the deflection of the beam is very much constant for different damping ratios as long as it stays below the jump-down frequency.

This type of robustness would be appreciated by the electronic circuits which should be powered by the harvester. The electrical loading may change a lot and the circuit designer prefers a power source which is less dependent on the loading conditions. In other word, a robust energy harvester will act as a DC voltage source with very small internal resistance in series or a current source with a huge internal resistance in parallel.

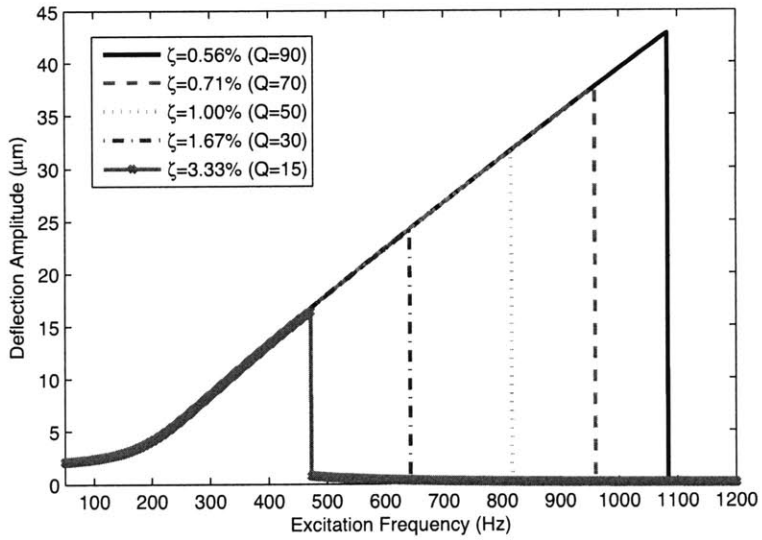

Figure 3-16: The effect of the total damping including mechanical damping and electrical damping on the frequency response of the system.

3.5.6 Bandwidth

Considering the stretching strain evaluated in Figure 3-14, normalized elastic energy due to the stretching can be estimated as a function of frequency. This curve also represents the normalized available electrostatic charge generated in the piezoelectric electrodes based on the open-circuit voltage. So it may be inferred that the ratio of extractable electric power to the maximum power would follow a similar pattern. The output power will drop to half the peak value at 900Hz which may suggest 190Hz bandwidth as shown in Figure 3-17. However, this bandwidth has been estimated assuming a fixed resistor as a load which is not the best method to extract the power.

Du Toit et al. have shown that by matching the electrical damping to the mechanical damping the maximum power can be harvested from a linear device [113]. The amplitude of vibration is linearly proportional to the Q-factor; hence, it will be decreased by increasing the total damping via electrical damping. From the other side, the extracted power is proportional to the electrical damping times the square of vibration amplitude. Accordingly, the optimum power harvesting scheme can be achieved at the matched condition in which the vibration amplitude in electrically-

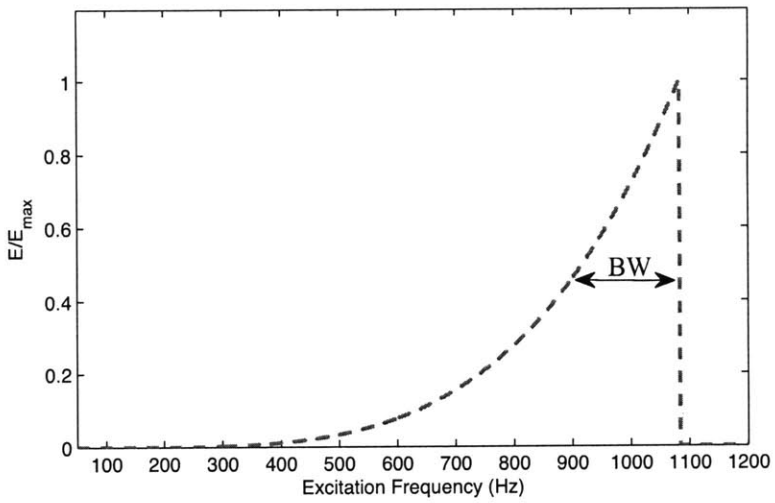

Figure 3-17: The ratio of harvestable power to the maximum power as a function of frequency based on the strain level evaluated in Figure 3-14.

loaded device is half of the unloaded one. Nevertheless, the nonlinear harvester shows a totally different response to the electrical loading. As mentioned in Section 3.5.5, the nonlinear harvester is robust to the damping ratio and the vibration amplitude doesn't change with the electrical damping. This property of the nonlinear harvester has been exploited here to achieve a much higher and more uniform electrical power in a wide range of frequency.

The aforementioned balanced energy harvesting scheme can be achieved by implementing better electronic circuits like SSHI circuit (will be explained in Chapter 6 [114, 115]). By increasing the electrical damping, the amplitude of vibration won't change that much as long as it stays in high-energy stable region. Therefore, the ultimate limit of extracting energy at each frequency is defined by the maximum electrical damping which keeps the system at the high-energy stable region. Therefore, the limiting factor on the maximum extractable power is set by the jump-down effect.

Figure 3-18, estimates the vibration amplitude and also the jump-down frequency under various electrical loading conditions. The response of the system has been simulated numerically for various loading conditions and the maximum electrical damp-

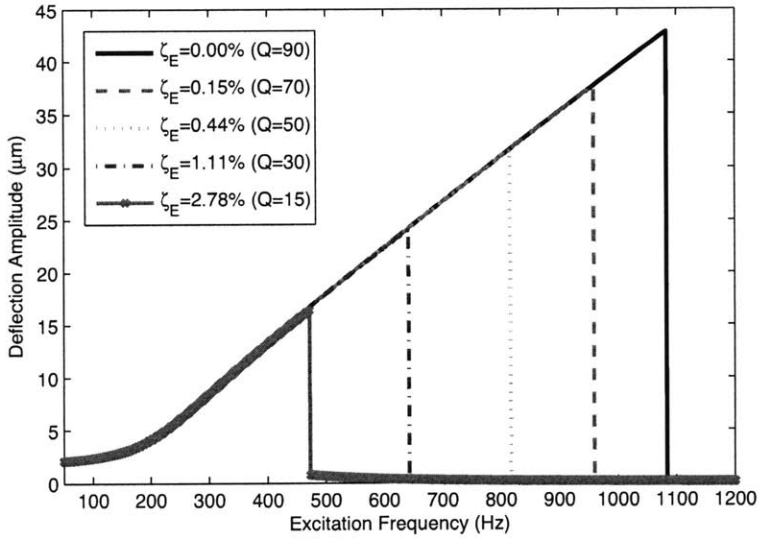

Figure 3-18: At every frequency below the jump-down frequency, the upper limit of the electrical power harvesting is defined by the maximum electrical damping at the threshold of the jump-down.

ing that can cause the jump-down has been estimated as a function of frequency as shown in Figure 3-19. It can be observed that although the harvester is vibrating at a smaller amplitude level at low frequencies, much larger electrical loading can be implemented without pushing the harvester to jump-down. Conversely, at frequencies over 1kHz, the upper limit for the electrical damping is less than 0.1%. Consequently, the harvester may easily jump down even for very small electric damping (electric current×voltage combination).

Therefore, by designing a smart electronic interface like adaptive SSHI, the harvester can be pushed to much higher voltage at lower frequencies to accomplish a more balanced power generation. The extractable electrical power at a given condition is proportional to the electric damping coefficient, frequency, and the square of vibration amplitude ($\dot{E_{elec}} \propto \sigma_E \times \delta^2 \times f_{ex}$). Accordingly, the maximum extractable electric power has been simulated in Figure 3-20. This simulation is based on an ideal electronic interface that can pump the voltage as much as needed. Nevertheless, as it will be explained later, there is a physical limit on the performance of such a circuit and the practical harvestable power may not reach this level. Using this scheme,

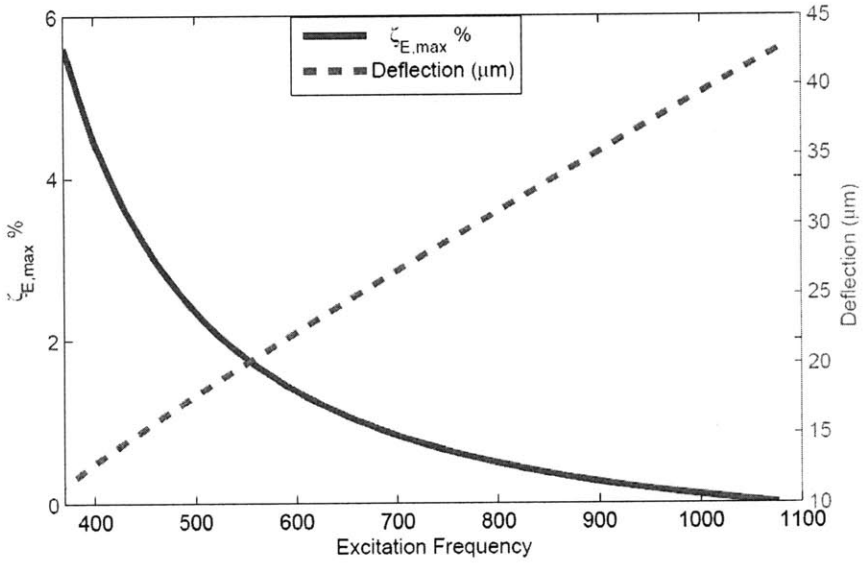

Figure 3-19: The maximum vibration amplitude and electrical damping ratio as a function of frequency.

600Hz of bandwidth is achievable around the peak frequency of about 770Hz. Therefore, for the first time an ultra-wide bandwidth energy harvester is achievable that can provide a fractional bandwidth of more than 75% in theory.

Another Viewpoint: Nonlinear Feedback

Through Sections 3.5.1-3.5.6, unique properties have been mentioned for the pie-shaped harvester which may look unusual compared to the linear designs. It is interesting to see how the nonlinearity resulted from the stretching doubly-clamped beams can change the whole dynamics of the system and enable an ultra-wide bandwidth (UWB) energy harvesting scheme. The main role of the stretching stiffness can be modeled as a nonlinear feedback which keeps the systems close to resonance independent of the excitation frequency, amplitude of vibration, and the damping forces. Figure3-21 depicts the main idea schematically.

Suppose that the system has been stabilized close to resonance (pre-resonance) and vibrates at a large deflection amplitude, Z. The equivalent stiffness of the system is mainly controlled by the stretching stiffness as derived in Eq. 3.27. Now, let's

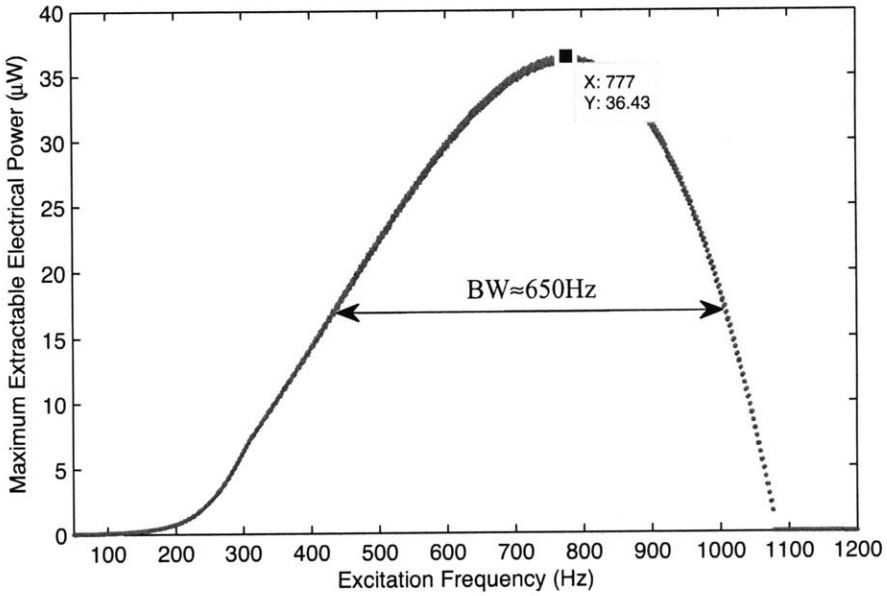

Figure 3-20: The maximum electrical power extractable as a function of frequency. This power is calculated based on the maximum electrical damping that may push the vibration to jump-down. Therefore its realization requires an ideal electrical interface.

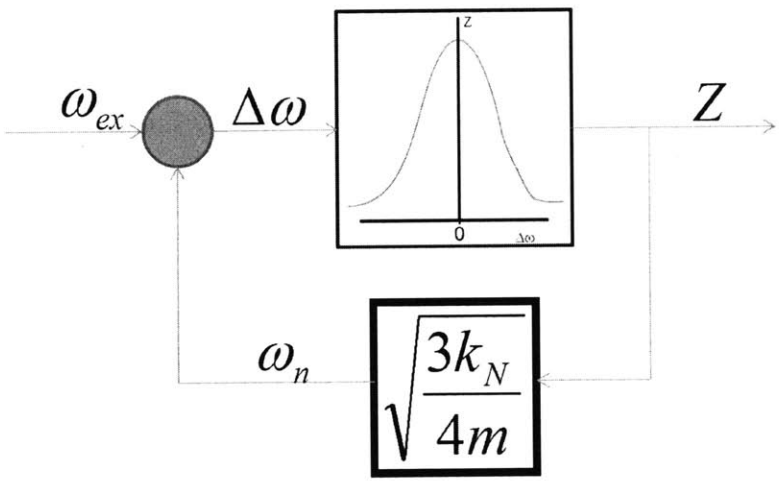

Figure 3-21: The wide-bandwidth resonance of the system can be explained by the negative feedback resulting from Duffing stiffness. Stretching stiffness induces an amplitude-dependent stiffness which forces the equivalent resonance frequency to track the excitation frequency.

assume that the excitation frequency is decreasing. For a linear oscillator, the amplitude of vibration would have been decayed quickly as the system goes off-resonance. Nevertheless, the amplitude-dependent stretching stiffness also decays in the case of pie-shaped harvester and push the natural frequency down as well. Consequently, the system will be back to resonance due to the close-loop negative feedback provided by the stretching stiffness. Therefore, the amplitude of vibration only slightly drops as a function of frequency change. The same type of negative feedback is also active in case of variations in the vibration amplitude and the damping forces. The nonlinear feedback from the stretching term and its effect on the equivalent resonance frequency always try to keep the vibration amplitude, Z, constant. This type of negative feedback is active in the high-energy stable regions shown in Figure 3-12. That's why the system will go automatically into the high-energy stable regions if the frequency ramped-up slowly from very low frequency. As long as it stays pre-resonance, the stretching stiffness stays active as a negative feedback to keep the system close to resonance for a wide range of frequencies.

Conversely, the stretching term would act like a positive feedback in case of the unstable region. The system is also close to resonance, but unlike the previous case it is stabilized post-resonance. Let's say the excitation frequency increases a little. The resonator becomes more off-resonance and the amplitude of vibration goes down slightly. Accordingly, the equivalent natural frequency would decrease which will make the system even more off-resonance. The amplitude of vibration goes down even more and the same cycle will be continued till the vibration become pretty quiet and the stretching stiffness becomes negligible. Finally, the system will act like a linear resonator which is operated at a frequency higher than its resonance. Therefore, very small deflection would be achievable and the harvester will converge to the low-energy stable solution. Consequently, when the harvester is ramped-down from high frequencies or after any jump-down, it is already in the low-energy stable regions (post-resonance) and the stretching term is negligible without any tuning effect. Suddenly, at the jump-up frequency, the system is close to the resonance and the amplitude of vibration is large enough to activate the stretching term and push

the system pre-resonance.

To better understand the effect of nonlinear feedback on the system's robustness and its UWB behavior, let's consider a mid-frequency working point of the harvester (e.g 650Hz). Based on Figure 3-11 or 3-19, the amplitude of vibration should be about $24.5\mu m$ and the maximum allowable electrical damping before the jump-down, $\zeta_{E,max}$ is about 1.06%. First, consider the linear equivalent of the system around this point for pure mechanical damping and no electrical damping ($Q = Q_0 = 90, \zeta_E = 0$).

The maximum displacement of the system has been evaluated based on the equivalent quality factor. It is notable that the dominant damping force is aerodynamic damping (and electrical damping in future cases) which is a linear function of amplitude and doesn't scale up with the stretching mode. Conversely, the total internal energy of the system scaled up nonlinearly with the amplitude due to large amount of elastic energy which will be stored in the stretching stiffness. Therefore, considering the definition of Q-factor,

$$Q_{eq} = 2\pi \times \frac{\text{Energy Stored}}{\text{Energy dissipated per cycle}} = \frac{\sqrt{mk_{eq}}}{c_{eq}} \tag{3.34}$$

the equivalent Q-factor of the system scales up at larger amplitude for a nonlinear harvester. Accordingly, the maximum displacement of the system can be evaluated:

$$\begin{aligned} \delta_{peak} &= \frac{A_{ex}}{(2\pi\omega)^2} Q_{eff} = \frac{A_{ex}}{(2\pi\omega)^2} \frac{\sqrt{k_{eq}m}}{c} \\ &= \frac{A_{ex}}{(2\pi\omega)^2} \sqrt{\frac{k_{eq}}{k_L}} Q_0 = \frac{5}{(2\pi(652))^2} \sqrt{\frac{3353}{476}} 90 = 71.5\mu m \end{aligned} \tag{3.35}$$

Knowing the peak amplitude, Q-factor, and the amplitude at 650Hz ($24.5\mu m$), an equivalent linear system can be estimated. This equivalent linear system approximates the behavior of the system due to the nonlinear feedback. The same process has been repeated for three systems with average electrical damping and finally for the maximum allowable electrical damping ($Q_T = 31, \zeta_E = 1.06\%$). This approximation for 5 different cases has been simulated and shown in the same graph (Figure 3-22)

for comparison.

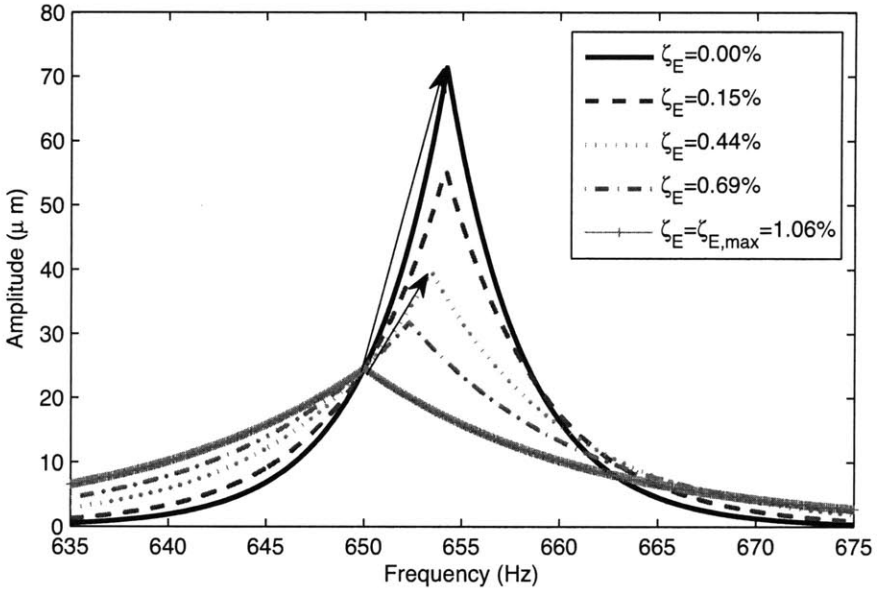

Figure 3-22: The nonlinear feedback keeps the resonator pre-resonance by acting like a barrier. The resonator needs a strong disturbance to climb this barrier. The arrows show qualitatively how large is the barrier (due to the nonlinearity) which keeps the system in the high-energy stable region. Increasing the electrical damping weakens the nonlinear feedback and decreases the barrier size. Finally at $\zeta_{E,max}$ there is no barrier and the system jumps down to the low-energy level without any external disturbance.

First, all the systems at 650Hz are slightly below the resonance and therefore the negative feedback is active. In case of no electrical damping, the amplitude of the vibration is much lower than the peak value. Therefore, the nonlinearity provides a much larger room for the negative feedback to keep the system stable in the high-frequency stable region. By increasing the electrical damping, the stability domain shrinks and the resonator has a higher probability of jumping over the resonance to the post-resonance region (unstable region).

Finally, at the jump-down damping, the system is semi-stable and any perturbation and disturbance can push the system to the post-resonant frequency. Unlike the pre-resonance which has a negative feedback, the post-resonance suffers from a positive feedback which will push the resonator further and further from the resonance.

In reality this happens almost instantly as a jump-down. Therefore, for the safe performance of the harvester at any frequency, the effective electrical damping should be smaller than the maximum allowable electrical damping to keep some stable region in spite of the possible disturbances.

The nonlinear feedback can similarly explain the the robustness to the vibration amplitude. Suppose the system is stabilized pre-resonance and vibrates at a large deflection amplitude due to the input vibration. Subsequently, let's assume the external vibration amplitude is increased. The output amplitude is trying to increase proportional to the input amplitude. However, the equivalent stiffness of the system will be increased also at higher amplitudes which pushes the resonance frequency higher. Subsequently, the gap between the excitation frequency and the resonance frequency becomes wider and the amplitude of vibration will drop as a result. This cycle shows the effect of nonlinear stretching stiffness as a negative feedback to keep the amplitude of vibration almost constant independent of vibration conditions.

3.6 Design considerations

Exploiting the stretching strain in the doubly-clamped beams, the pie-shaped design provides a number of unique properties compared to the linear harvester:

- Ultra-Wide Bandwidth
- Robustness
- Very high power harvesting density exploiting up to 0.1% strain of PZT

Nonlinearity Criteria

To fully materialize these features, the nonlinear mode should be reinforced through some design considerations. The harvester needs to be activated in its high-energy stable region which requires the dominance of the stretching force compared to the other linear elastic forces:

$$(k_B + k_{\sigma_0})\,\delta \ll k_s \delta^3 \tag{3.36}$$

Replacing the values for k_B, k_{σ_0} and k_S from Eq. 3.17, the nonlinearity criteria can be expressed as a function of design parameters:

$$\left(\frac{\pi^2}{2}\right)\left[\frac{\sigma_0 wt}{L}\right] + \left(\frac{\pi^4}{6}\right)\left[\frac{Ywt^3}{(1-\nu^2)L^3}\right] \ll \left(\frac{\pi^4}{8}\right)\left[\frac{Ywt}{(1-\nu)L^3}\right]\delta^2 \tag{3.37}$$

Structural Properties

The linear stiffness is determined by the residual stress stiffness, k_{σ_0}, if

$$\frac{\sigma_0}{Y} \gg \left(\frac{t}{L}\right)^2 \tag{3.38}$$

;otherwise, the bending stiffness would determine the linear stiffness for the harvester. The main structural materials of the harvester consist of silicon nitride, silicon oxide, PZT and ZrO_2 which have Young's modulus in the range of 60GPa (oxide) up to 300GPa (nitride). In addition, the minimum residual stress can only be controlled up to tens of MPa in the structure. Therefore, the linear term would be determined mainly by the residual stress in the structure unless the thickness becomes thicker than 1%-2% of the length which is not the case in our harvester. Therefore, the linear stiffness is mainly determined by the residual stress in the beams and the nonlinearity criteria can be simplified and approximated by the following condition:

$$\frac{\delta}{L} \gg \sqrt{\frac{Y}{\sigma_0}} \tag{3.39}$$

This relationship implies that the nonlinear properties of the system can be improved by employing stiffer materials with high Young's modulus as the structural material, reducing the residual stress in the structure as much as possible, increasing the deflection of the structure and finally using shorter beams. The selection of structural material and engineering a low-stress structure will be discussed in Chapter 4.

Beam Length

Selecting the right length for the beams is not straightforward. The linear natural frequency of the system is determined by

$$f_n \approx \sqrt{\frac{\sigma_0 wt}{8m_{pm}L}} \tag{3.40}$$

, and should be minimized to satisfy the design requirements for the frequency range of operation and also increase the deflection amplitude. Therefore, decreasing the length of the beam to improve the nonlinearity will adversely increase the natural frequency. Consequently, it should be optimized in a mid-range value to satisfy both conditions. Accordingly, typical length of the beams in the harvester is selected to be in the order of a few millimeters to keep the resonance frequency low enough (about 100Hz) without sacrificing the nonlinearity. In general, the length of the beams should be selected first based on the the design frequency range.

Proof Mass

The choice of proof mass is clear: the heavier, the better! A heavy proof mass will decrease the natural frequency, inject more inertial energy into the system and consequently improve the power generation level and bandwidth. As a result, the whole thickness of the wafer is used as the proof mass in the pie-shaped harvester. Nonetheless, the heaviest proof mass that can be achieved by this method is limited to 10s of milligrams. Heavier proof masses (100s of milligrams) is required to enable the ultra widebandwidth (UWB). This range of mass is only feasible by attaching an external structure to the harvester. This approach has been pursued in the new generation of harvester (Section 3.7).

Thickness

The thickness seems not to affect the system's nonlinearity directly (Eq. 3.39) and to increase the natural frequency (Eq. 3.40). Nevertheless, as it will be explained in Section 4.2.1, the average residual stress can be controlled better for thicker structure

by adding stress-cancellation layers. Consequently, in practice the average controlled residual stress, $\bar{\sigma}_0$, can be decreased by increasing the thickness while keeping the natural frequency constant. Furthermore, a thicker structure can support a heavier external proof mass without failure. Hence, a general design guideline is to increase the thickness as much as possible if it can decrease the average residual stress without disrupting the fabrication process. The theoretical upper limit for thickness is defined by the Eq. 3.38.

Number of beams

The concept of beam geometry and its effect on the bending strain distribution was presented in Section 3.2.2. A triangular-shaped beam was proposed as the optimum geometry to get uniform bending strain in bending mode. Nevertheless, the stretching strain distribution would be uniform across the beam's length in case of rectangular-shaped beam with constant width according to the beam theory. Consequently, the trapezoidal-shaped beams in the pie-shaped harvester will provide a balance of strain distribution in doubly-clamped beams with respect to both stretching and bending components. The bending strain would be more uniform than the rectangular-shaped beam across the length at the expense of some non-uniformity in the stretching strain. Nevertheless, if stretching strain is targeted as the main mode of energy harvesting, the rectangular-shaped beams will provide a better uniformity. Employing rectangular beams in pie-shaped structure would result in the waste of active area due to the free space between the beams (Figure 3-23).

3.7 3rd Generation

To reach a higher level of performance such as output power and bandwidth, the pie-shaped harvester was fully reviewed and a new harvester is designed based on the design considerations reviewed in Section 3.6. Furthermore, new process considerations and electrode configurations are implemented to improve the system. The lessons from the fabrication and testing of the pie-shaped harvester have been the

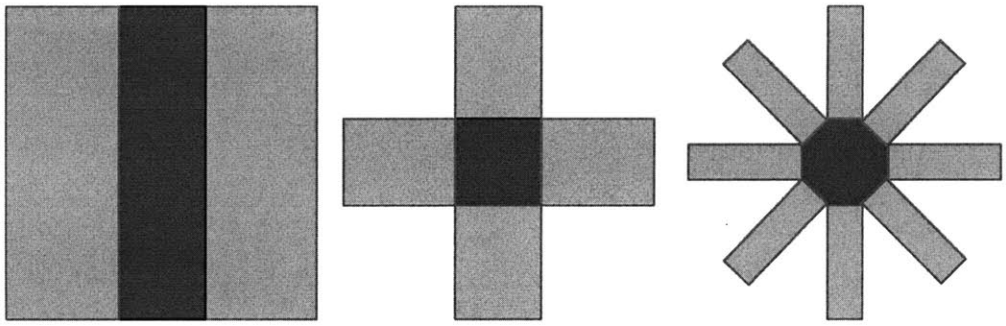

Figure 3-23: Increasing the number of rectangular beams in the pie-shaped structure decreases the active area. Wide doubly-clamped rectangular-shaped beams with central proof mass is a more efficient topology (75% active) compared to the pie-shaped designs (37.5% and 30% active area in case of 4-beam and 8-beam topologies, respectively)

main motivation for redesigning the system and have been implemented in the new generation.

The mechanical structure of the new design is depicted in Figure 3-24. The arrangement of the beams has been changed from pie-shaped to simple wide rectangular-shaped beams with small central masses. In each device, 4 beams have been placed to increase the power. Therefore, the harvester consists of four identical cells which will be connected to an external proof mass. The motion of every beam will be synchronized by a single external mass.

The mechanical properties of all cells should be almost identical because they will be fabricated in the same batch close to each other in a wafer. The external mass can be fabricated by any manufacturing technique and will be connected to the main part by any possible assembly method like bonding or gluing. This design would decouple the fabrication of proof mass from the main structure. In addition, any beam length can be selected only based on the frequency constraints and independent of the total device size. Subsequently, the number of cells is not limited to 4 and should be determined based on the total power requirement and the size of the device.

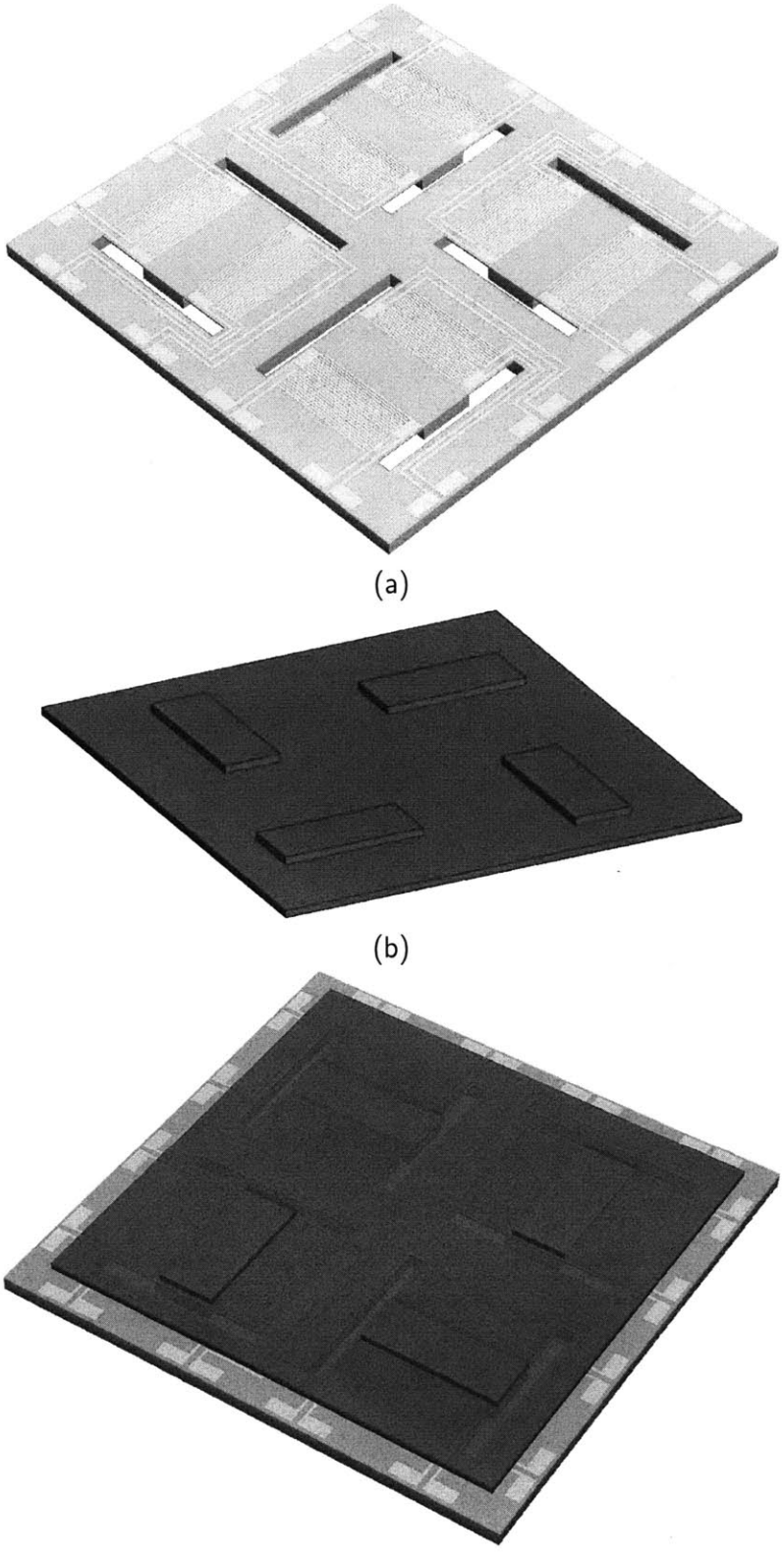

Figure 3-24: The schematic structure of 3rd generation energy harvester: a) the main part consists of four doubly clamped beams, b) the external proof mass, c) the assembled part

3.7.1 Electrode Configuration

As explained in Section 2.4, typical bulk piezoelectric energy harvesters use top and bottom electrodes to extract the charge from the PZT. Nevertheless, the direction of strain would be perpendicular to the electric field direction. Hence, the weaker mode of piezoelectric effect, d_{31} mode, would be used for energy harvesting which is less effective than the d_{33} mode. Since the piezoelectric micro power generator [10], top interdigitated electrodes have been deposited on top of the thin-film PZT to align the direction of mechanical strain and the polarization in order to exploit the more effective d_{33} piezoelectric mode. A similar interdigitated electrode pairs have been adapted to the pie-shaped structure as shown in Figure 3-25.

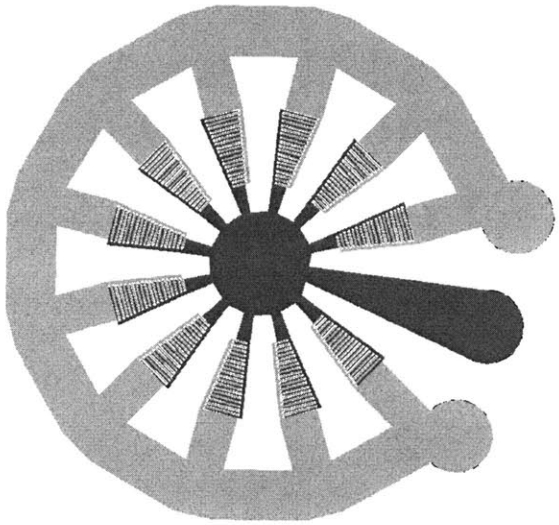

Figure 3-25: Interdigitated (IDT) electrodes extract the generated charge from PZT using d_{33} mode of piezoelectric effect. All the electrode have been electrically connected in parallel to increase the output current.

Figure 3-26 shows the distribution of both strain components, bending and stretching, across the length of the beams. The stretching component is almost uniform across the beam, but the bending strain is changing from highly tensile at one end gradually to highly compressive at the other end. Therefore, the average bending strain in the beam would be zero and the IDT electrodes shown in 3-25 only collects the electrical charge generated by the stretching strain. The stretching strain is the dominant component in the high-energy stable region of performance which is the tar-

geted region of pie-shaped energy harvester. Consequently, the configuration shown in 3-25 seems satisfactory for the energy harvesting purpose and was implemented in the pie-shaped design.

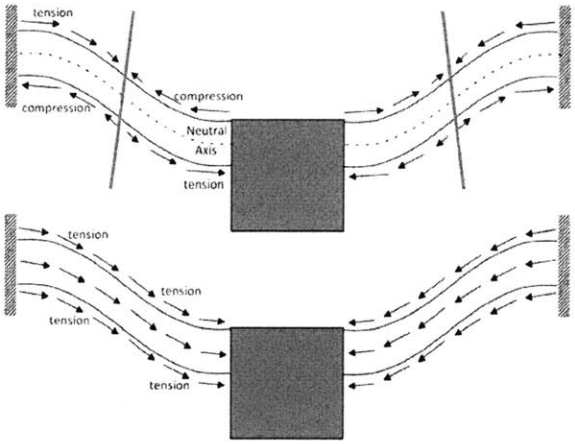

Figure 3-26: Bending strain (top) and stretching strain (down) distribution across the length and thickness of the doubly-clamped beams. Half of the beam's length would undergo a compressive bending strain while the other half is in tension.

A new configuration has been proposed and implemented in the 3rd generation of energy harvester. It is based on spanning the length of each beam by two pairs of electrode. The concept of dual-electrode placement has been shown graphically in Figure 3-27. Using separate electrodes per half enables us to access the bending mode for measurement, energy harvesting at low-amplitude vibration, and actuation mode which is required for start-up circuit (will be explained in Section 6.2).

Furthermore, increasing the number of separate electrode pairs in the harvester provides a redundant electrical configuration. Consequently, shorted and unhealthy sections of the harvester can be electronically eliminated from the circuit to avoid electrical shortage during the testing and development stages of the project. In addition, the connection between the electrodes can be reconfigured from parallel connection to serial connection or any mixed parallel/serial combination to achieve the right voltage/current combination required for the application. Figure 3-28 shows the idea of redundant connectivity implemented in the 3rd generation of energy harvester.

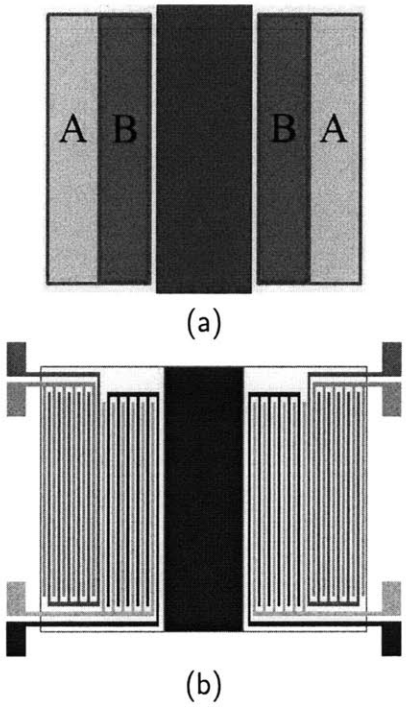

Figure 3-27: Splitting the length of the beam into two pairs of electrodes: a) d_{31} mode electrodes, b) d_{33} mode electrodes (IDT)

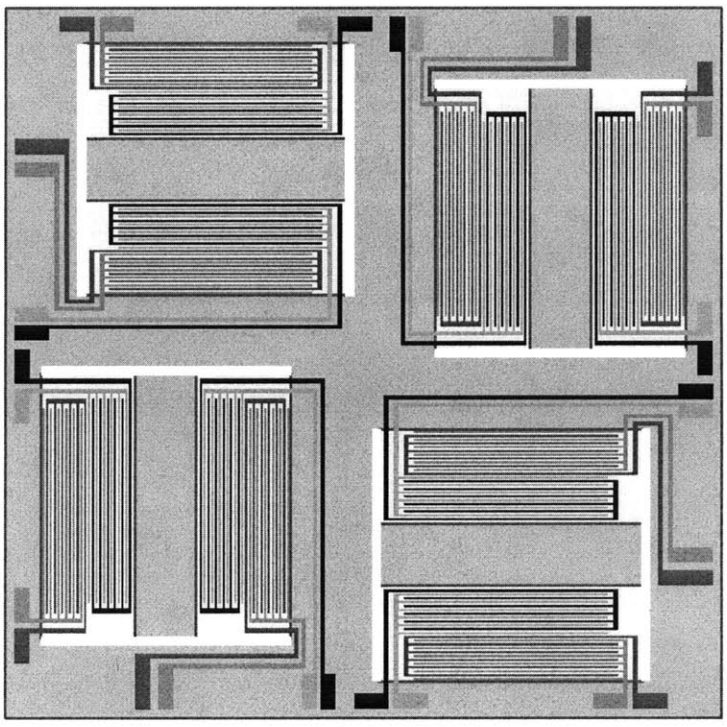

Figure 3-28: IDT electrodes configuration in the 3rd generation device

3.7.2 Properties

In summary, the main improvements aimed by the 3rd generation of energy harvester is listed below:

- **Ultra-Wide Bandwidth and Robustness**

  The fractional bandwidth has been improved from less than 1% up to more than 75% (UWB) in theory. The negative feedback from the nonlinear stretching stiffness decreases the sensitivity of the output to unknown conditions such as vibration amplitude, electrical loading, and mechanical damping.

- **Decouple Fabrication**

  The fabrication of the main device has been decoupled from the proof mass which can be fabricated separately by any fabrication technique. Heavy proof masses (100s-1000s milligrams) can be implemented accordingly.

- **Power Level**

  The total extractable power has been increased through: a) achieving maximum strain level (0.1%) uniformly across the beam, b) increasing the active area, c) increasing the inertial force by using heavier proof mass, d) smart electronic interface using active elements (SSHI method).

- **Electric Connection**

  Spanning the length of the beams by two pairs of electrodes decouples the stretching/bending components and enables the actuation mode required for the start-up circuit. Furthermore, the redundancy in the electric connection between cells improves the electrical robustness to shortage and provides an adaptive voltage/current reconfigurability.

- **Printable MEMS Design**

  A new digital fabrication method is applicable to the new generation. Active elements (PZT/electrodes) can be printed directly on the released structure and subsequently the external proof mass will be assembled [116].

Chapter 4

Fabrication

4.1 2nd Generation: Pie-Shaped Structure

Device fabrication includes a combination of surface micro-machining steps to form the active layer and also bulk micro-machining to shape up the structure (Figure 4-1). Carving the whole thickness of the silicon wafer makes it possible to get a heavy proof mass which is not otherwise possible by surface micromachining techniques.

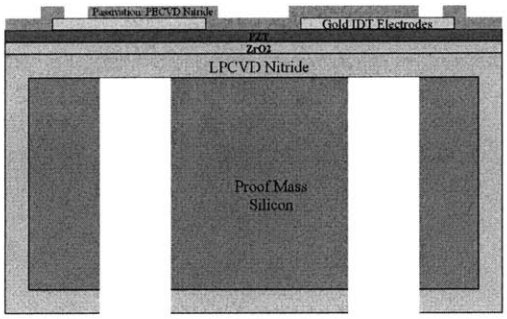

Figure 4-1: Schematic cross-section of the device

4.1.1 Structural Layer

The doubly-clamped beams in the structure are thin and long and should be able to hold a heavy proof mass. Therefore, a low-stress and high quality structural material is essential and critical to withstand large strain during the device fabrication and

performance.

Thermal Oxide

First candidate as the structural material was thermal oxide as it had been used in type-I PMPG. The maximum practical thickness that the thermal oxide can grow is up to $1\mu m$-$2\mu m$. Afterward, the slow diffusion rate of oxygen through the oxide layer will limit the oxidation. However, a thermal oxide layer at this thickness level couldn't hold the heavy proof mass due to its porosity and high residual compressive stress.

PECVD Oxide

Up to $10\mu m$ of PECVD oxide was deposited to increase the structural strength so that the structure can survive various sorts of stress throughout the fabrication and device release steps. However, a thickness of $10\mu m$ was much bigger than the design value (2-$5\mu m$) required for low-frequency stretching mode of vibration. Furthermore, the device has a high risk of buckling due to the residual compressive stress. In addition, PECVD oxide does not provide the stiffness which is required for nonlinear behavior of the system.

Silicon

Single crystal silicon can be a great material to form the structure. It has very high structural strength, almost no defects, and zero-initial stress by its nature. Nevertheless, its implementation in the process plan requires an etch stop layer beneath it. SOI wafers can be used for this purpose, but they cost much more than normal silicon wafers. Furthermore, another possibility is to diffuse or ion-implant boron at certain depth to form an etch stop in case of KOH etching. This approach can be pursued in future works to achieve very high-quality commercial devices at a low cost.

LPCVD Nitride

Low pressure chemical vapor deposited (LPCVD) silicon nitride has been widely used as the diaphragm and structural material in MEMS fabrications. It shows large fracture strain (3%), large Young's modulus (250GPa-300GPa), and high etch selectivity to silicon and silicon oxide. Its residual stress can be controlled by changing the gas ratio during the deposition. LPCVD nitride can easily be deposited in a reproducible, very pure and uniform way. This leads to layers with good electric features, very good coverage of edges, high thermal stability and low etch rates. However; high temperatures are necessary for deposition and reaction rate is slow. Considering all these properties, LPCVD nitride has been finally chosen as the structural material that can satisfy the required conditions.

Process

Thermal silicon oxide is grown on RCA-Cleaned 4-inch silicon wafers as the first layer which acts as the etch stop to DRIE and XeF_2 etching steps.

Equipment	tube 5D-ThickOX at ICL
Oxidation condition	wet at $1000°C$
Oxidation time	23mins 45secs
Thickness target	$200nm$

Subsequently, the wafers are immediately transferred to a low pressure chemical vapor deposition (LPCVD) vertical thermal reactor. $2\mu m$ thick silicon nitride is deposited as the main structural layer. The recipe is optimized by the staff to reach the maximum etch selectivity to oxide for semiconductor research and cannot be changed:

Equipment	SVG/Thermco 7000 Series
Deposition temperature	$775°C$
Gas flow	250 mT, 25 sccm NH_3, 250 sccm SiH_4
Deposition time	11hrs 9min
Thickness target	$2\mu m$-$2.2\mu m$

Subsequently, $200nm$ of PECVD oxide is deposited on top of the nitride layer to get a symmetric structure. The oxide layer is necessary to prevent the chemical reaction between silicon and the lead that diffuses from the active layers. Up to this point, all the steps are high-temperature CMOS-compatible processes and performed in the Integrated Circuit Laboratory (ICL). Subsequently, the wafers are transferred to Technology Research Laboratory (TRL) for further gold-compatible processes. The active layer is formed and the structure is patterned throughout the next steps at TRL.

4.1.2 Active Layer

Unlike the macro scale energy harvesters that employ slabs of bulk PZT, a layer of thin-film PZT should be deposited and patterned in the MEMS-scale versions. In our case, the thin-film PZT has been deposited by sol-gel spin-coating method and then patterned via wet or dry etching processes. Well-controlled rapid thermal annealing transforms the pyrolyzed ceramics into its Perovskite phase to ensure a strong piezoelectric performance. A large percentage of Perovskite phase PZT is required in order to perform the required energy conversion.

It is tricky to deposit thin-film PZT on silicon substrate for MEMS applications. Several methods such as sputtering, pulse laser deposition, and screen printing have been reported to deposit thin-film PZT layer. The challenge is to preserve the exact stoichiometry needed to reach good piezoelectric performance. Sol-gel spin-coating is proved to be a suitable option to deposit stoichiometric and uniform PZT and has been used by authors for various PZT/MEMS applications [10,117,118]. Therefore, sol-gel spin coating has been used to deposit thin-film ZrO_2 and PZT layers throughout this research.

Zirconia (ZrO_2)

Conventionally, Platinum is being used as the top and bottom electrodes of PZT for d_{31} mode. Contrarily, the d_{33} piezoelectric mode uses top IDT electrodes and requires

a dielectric as the bottom layer. Platinum is a conductive metal and cannot be used as the diffusion barrier in d_{33} mode. Since the first PMPG, ZrO_2 has been chosen as the diffusion barrier and bottom layer for PZT. ZrO_2 has a crystal structure which is similar enough to that of PZT that can be used as its seed layer. Its function is to block the diffusion of the lead from PZT to the structural layer and its reaction with silicon.

First, the ZrO_2 solution developed by Mitsubishi Material is coated, dried, and pyrolyzed and then cooled down back to room temperature on hot-plates to obtain about $80nm$-$100nm$ of ZrO_2 per coat. The process is repeated twice to reach the thickness of $0.15\mu m$-$0.25\mu m$ which is necessary to avoid reaction between PZT and silicon oxide. The ZrO_2 layer is difficult to be etched after annealing and therefore is patterned and wet etched in BHF solution after pyrolysis and before annealing.

Subsequently, the resist is stripped in the microstrip solution. Finally, cleaned wafers are annealed at $700°C$ for 3 hours in box furnace. This process has been optimized to obtain high quality PZT without cracks. To avoid thermal shock, the furnace is ramped up gradually from room temperature to $700°C$ and vice versa. Pyrolysis time is increased to ensure the burning of all organic material before annealing to avoid any residual stress or crack.

Solution	9%wt ZrO2 solution by Mitsubishi Materials
Spin-coat	500rpm(5secs)-2500rpm(25secs)
Drying/Pyrolysis	$80°C$(150 secs)/$200°C$(150secs)/$380°C$(300 secs)
Target thickness	$80nm$-$100nm$ per coat
Etch	BHF solution(10secs)
Anneal	$700°C$(3hrs), Thermolyne Furnace, 6000

Lead-Zriconium-Titanate (PZT)

The PZT sol is a colloidal suspension of Lead Acetate ($Pb(CH_3CO_2)_23H_2O$), Zirconium-tetra-n-butoxide ($Zr(n\text{-}OC_4H_9)_4$) and Titanium-tetra-iso-propoxide ($Ti(i\text{-}OC_3H_7)_4$) in a 2-Methoxyethanol solvent. The solid solution is spun onto the wafer at 2000-3000 RPM and quickly dried (pyrolyzed) to remove the solvent, causing the suspended

particles to precipitate to an amorphous thin film.

Several thin films can be deposited on top of one another to develop a total film thickness up to several hundred nanometers, though the increased thermal cycling tends to degrade the quality of the final film. The perovskite phase of PZT forms during a high temperature (approximately $650°C$-$700°C$) anneal following deposition. Extensive investigation has been done to reach the optimal recipe that gives a high-quality crack-free PZT in its piezoelectric perovskite phase.

A layer of PT solution on top of ZrO_2 is proved to be a good seed layer for PZT. Furthermore, it improves the yield rate of the process by providing extra lead to the PZT. The thin PT layer followed by three to four layers of PZT is spin-coated to create a thick layer of PZT ($0.2\mu m$-$0.4\mu m$). The same pyrolysis, cooling, patterning, wet-etching and resist-stripping procedures as that of the zirconium oxide are utilized.

Previously, reactive ion etching using BCl_3:Cl_2 etchant was being used to pattern the ZrO_2 and PZT layers. However, the RIE step is too aggressive and the PZT layer would have been attacked even with a double coat thick photo-resist. Consequently, the RIE step is replaced with wet etching of each film after pyrolysis and before the annealing step to achieve a high-quality crack-free PZT. Finally, the patterned PZT is rapid-thermally annealed at $700°C$ for 60secs which highly improves the reliability of the process compared to the traditional box-furnace annealing.

Solution	1%wt PT/15% PZT E1 solution, Mitsubishi Materials [119]
Spin-coat	500rpm(5secs)-2500rpm(25secs)
Drying/Pyrolysis	$380°C$(300 secs)
Target thickness	$80nm$ per coat
Repeat	1 coat PT + 4 coats PZT
Etch	dip in DI Water(1000ml)+HCL(300ml)+BOE(50ml)
Anneal	$700°C$(60secs), RTA AG Associates Heatpulse 410

Top interdigitated electrodes

Instead of top and bottom electrodes, top interdigitated electrodes are employed in d_{33} mode to collect the electrical charge generated in the PZT as a result of strain.

2000Å of Platinum on top of 200Å of Titanium as adhesion layer are e-beamed. The electrodes are patterned by lift-off method using AZ5214 photoresist and soaking in the acetone overnight. Few minutes of ultrasound shaking can ensure a complete liftoff which is necessary in avoiding electrode shortages. (Figure 4-2).

Lithography	AZ-5214 coat (2000rpm) / Exposure 1.4 secs
	Flood Exposure 48secs
Electrodes	Ti/Pt (200Å/2000Å)
Equipment	EBeamFP Temescal Model FC2000
Liftoff	Overnight acetone bath+ultrasound shaking (2 mins)

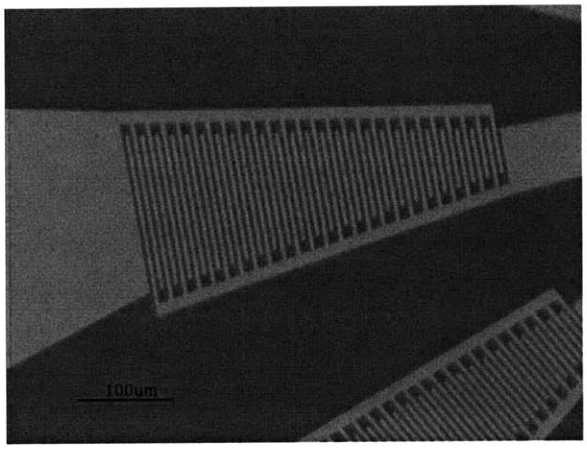

Figure 4-2: 200Å Ti/2000Å Pt are e-beamed and patterned by lift-off. IDT electrodes collect the electrical charge generated in the PZT layer in d_{33} mode.

4.1.3 Passivation

Device shortage has been a serious challenge that can dramatically reduces the yield rate of the process. Each device has thousands of parallel interdigitated electrodes and can be easily shorted by particles or electrode delamination. To address this issue, a passivating layer is added that electrically and chemically passivates the electrodes and the PZT layer throughout the fabrication and testing steps. With the passivation layer, a device can be easily cleaned after dry etching in Piranha solution. Piranha cleaning is not possible without the passivation due to the reaction between

the electrodes and the solution. Furthermore, long time etching in XeF_2 has the risk of attacking the titanium layer and delamination of electrodes in a non-passivated device (Figure 4-14). Finally, encapsulated active layer will enhance the robustness of the device in harsh environments.

Passivating layer consists of $150nm$ thick PECVD silicon nitride followed by $150nm$ thick PECVD silicon oxide. Silicon nitride has a better adhesion to PZT and electrodes compared to PECVD oxide. Moreover, it encapsulates the active layer in a silicon nitride sandwich. Silicon oxide, unlike silicon nitride, is almost inert to the XeF_2 etching and the combination of both layers gives us a pretty reliable passivating properties. Finally, to access the wire-bond pads of the electrodes for wire-bonding and packaging, vias are etched in the passivating layer (Figure 4-3).

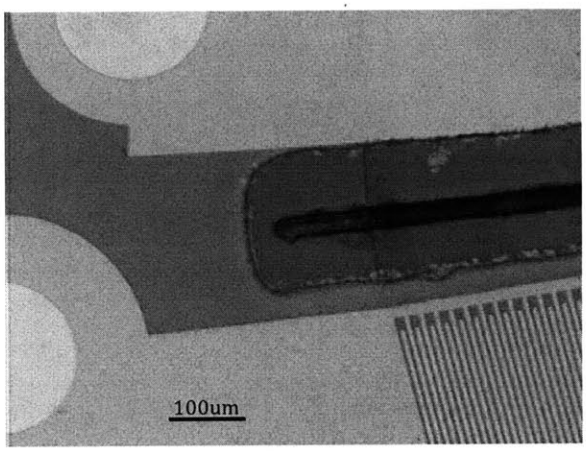

Figure 4-3: dry-etched vias (yellow circles) in the passivating layer provides access to the pads for wire-bonding

4.1.4 Etching and Release: Issues and Challenges

PZT etching

Etching the structure and releasing the device faces many challenges. Active layer should be carefully preserved throughout the etching steps. The PZT layer or the top interdigitated electrodes can be attacked by the etchants. At the release stage and afterward, the device faces enormous stress components like ion bombardment,

stiction, overheating, and capillary forces. It is really hard to perform any processing on thin and fragile beams after being released. Long time reactive ion etching may burn the photoresist and makes it extremely difficult to be stripped.

Various etching and releasing schemes have been tried to overcome these challenges. As it mentioned before, both ZrO_2 and PZT layers were wet etched and patterned in BOE solution before the annealing and after the pyrolysis to avoid the difficulties in etching the annealed ceramic. The PZT wet etching may cause severe undercut that can be 3 to 10 times bigger than the etching depth (Figure 4-4).

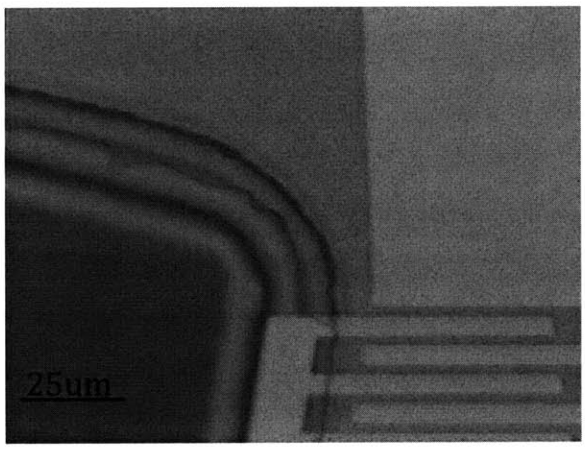

Figure 4-4: Large undercut in PZT during the wet-etching with BOE solution.

Dry etching using BCl_3:Cl_2 is another possibility. Nevertheless, that process needs substrate heating up to $80°C$ to make the reaction products volatile. The ion bombardment often burns the resist, which is really difficult to be stripped, and even attacks the underneath PZT layer.

Fabrication restrictions at Microsystems Technology Labs (MTL)

There are some fabrication restrictions associated with the equipments in Micro Technology Laboratory that add some extra limitations on the fabrication design. For example, Some machines accept special wafer sizes like the DRIE machines and the PZT spin-coater which can only handle 6" wafers and 4" wafers, respectively. Some machines called 'green' machines are allocated for CMOS processing in which no

gold-contaminated wafer is allowed vs the others that are gold contaminated ('red' machines).

Deep Reactive Ion Etching (DRIE)

The structural layer and the excessive silicon should be patterned and etched to define the beams and the proof mass, respectively. Wet-etching should be avoided at this stage to avoid extra undercut and damage to the PZT layer. Deep Reactive Ion Etching (DRIE) machines have nice features like efficient cooling systems, high etching rate, and directional etching and can be used to carve the structure of the device. Nevertheless, the DRIE machines in MTL only load 6" wafers and skillful wafer mounting of 4" wafers on the 6" carrier wafer is extremely essential to ensure a sufficient heat transfer from the wafer to the carrier.

The nitride etching and OLE3 recipes are employed to etch the structural layer from the wafer's top side and whole silicon wafer from its back, respectively. The thermal oxide layer acts as the etch stop layer for the OLE3 recipe to some extend, but the etch rate nonuniformity across the wafer requires an extremely ideal etch stop. Additionally, the ion bombardment associated with DRIE can invoke excessive heat and stress on the active layer and break the device. The stiction of the released device to the carrier wafer can also increase the chance of device breakage during the release. Consequently, a final low-stress release step that can trim the residual silicon from the device would be extremely helpful to circumvent these drawbacks.

KOH Etching

KOH etching has been a well-developed micro-fabrication technique for releasing MEMS structure. It etches silicon very fast and stops at silicon nitride. We tried the KOH bath for final trimming and releasing the device by adding the PECVD nitride layer as the passivating layer, but the solution delaminated the porous nitride layer. In addition, extremely thin and fragile beams were frequently cracked by the capillary force of the solvent and also hydrogen bubbles.

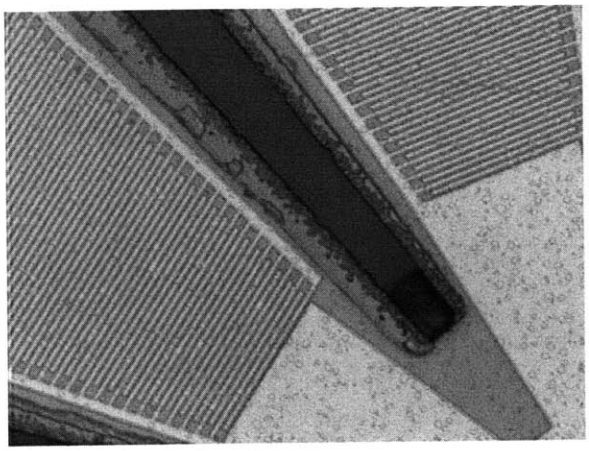

Figure 4-5: Optical image of a released device (top view)

Xenon Difluoride (XeF_2)

Xenon difluoride, XeF_2, has a remarkable ability in etching silicon at a relatively high rate with no ion bombardment or external energy source requirement. These characteristics make it a favorable solution in our case. We modified the process accordingly to make it compatible with a final XeF_2 etching release step. Originally gold electrodes were replaced by platinum which is more inert to the XeF_2 etchant. PECVD oxide passivating layer was added to prevent the PECVD nitride etching during the release.

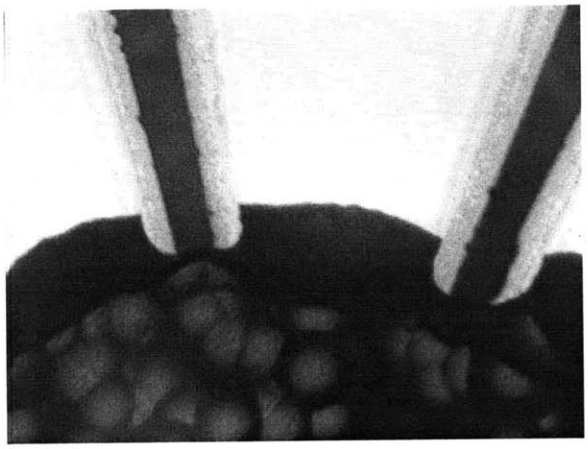

Figure 4-6: Undercuts in the silicon proof mass (dark brown), the IDT electrodes behind the transparent LPCVD nitride, and the openings between beams can be easily seen in the optical image of a released device taken from its back.

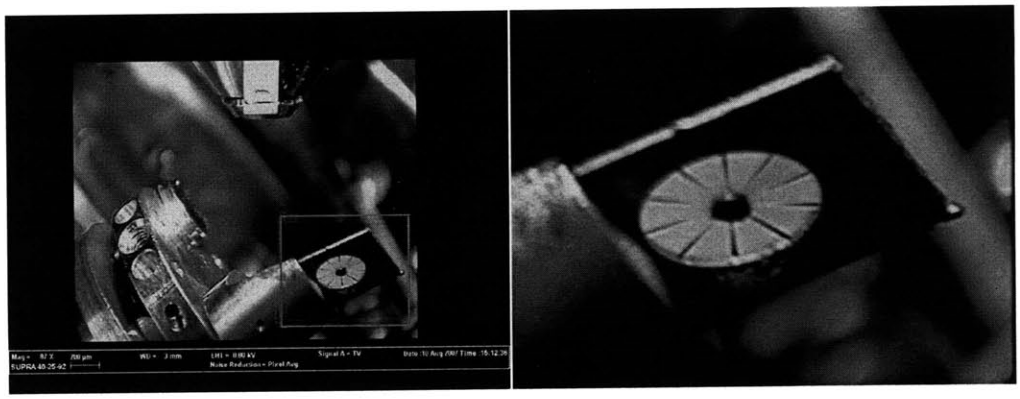

Figure 4-7: Fully released device (back side)

4.1.5 Released Device

The optical images of the released pie-shaped energy harvester have been shown in Figure 4-5 and Figure 4-6. Furthermore, a picture of the whole device has been captured by external camera of the SEM machine as shown in Figure 4-7. The device is healthy without any crack and the central proof mass is suspended by the beams. Figure 4-8 depicts the SEM image of the pie-shaped device. The undercut during the wet-etching of the PZT can be clearly identified in this figure.

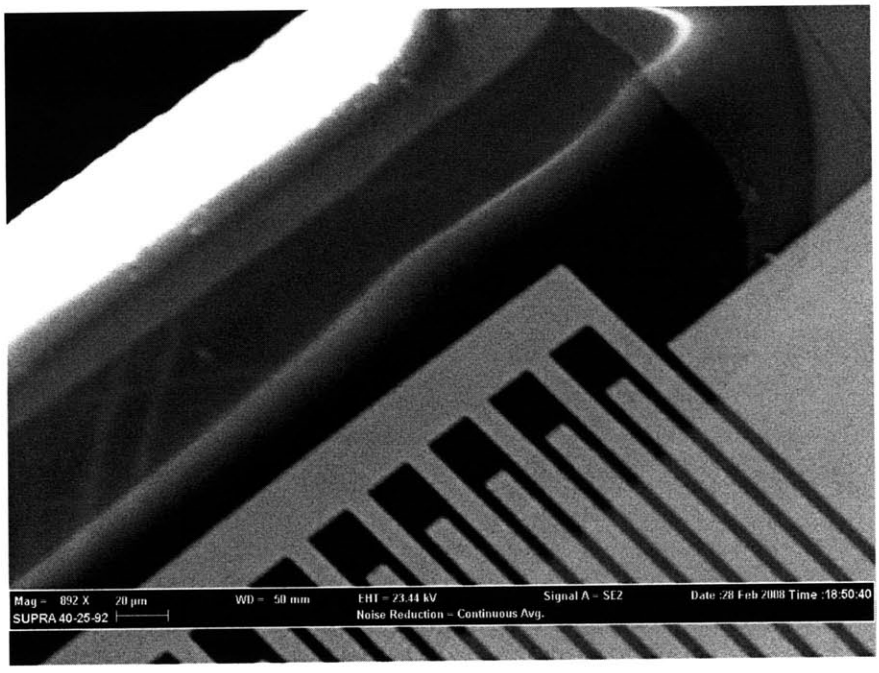

Figure 4-8: SEM image of a released device shows the interdigitated electrodes

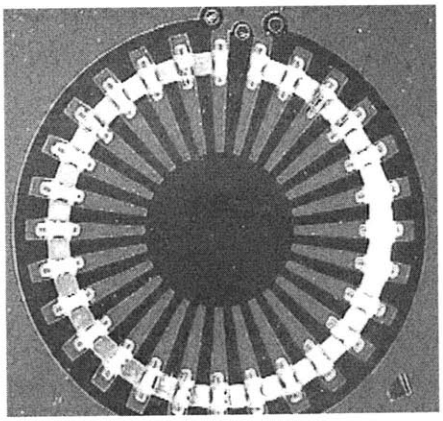

Figure 4-9: Optical image of a released device (top view)

The process plan for this process has been schematically shown in Figure 4-10.

4.2 3rd Generation

After testing and reviewing the pie-shaped energy harvester, few issues and problems associated with its design and fabrication were identified. A new design, called 3rd generation, was presented and described in Section 3.7. The structure and its fabrication process has also been modified to enhance the performance of the device and also to improve the fabrication yield rate.

The average residual stress in the structure and also its distribution across the thickness has been the most important factor that affects the device's performance and fabrication. Therefore, it has been targeted in the 3rd generation and an extensive investigation and analysis has been performed accordingly. A very low-stress (less than 10MPa) structure has been engineered by precisely controlling the composition of the beams.

In addition, some minor modifications in the electrode material, PZT processing and the release process have been implemented to increase the yield rate. Furthermore, the 3rd generation requires the assembly of external proof mass which requires a different packaging procedure. Also, the micro-machining of the proof mass has been explained. The general process plan is similar to the Figure 4-10, but the details of every step has been modified to improve the fabrication quality.

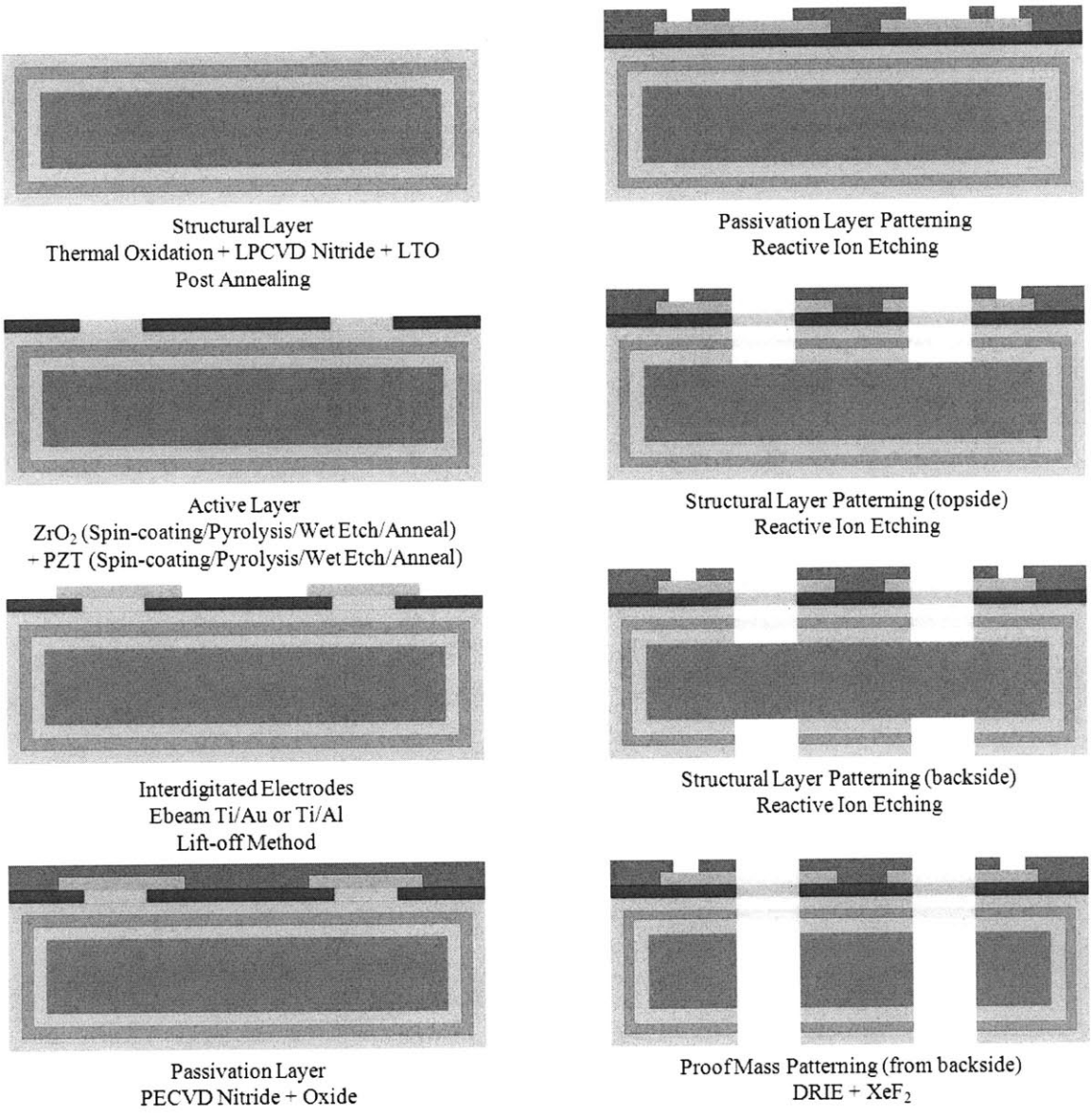

Figure 4-10: Fabrication process plan

4.2.1 Stress Engineering

As explained in Section 3.6, the average residual stress in the beams defines the linear stiffness, natural frequency and the bandwidth of the harvester. Consequently, it should be minimized as much as possible to reach a low-frequency harvester with UWB performance. In the fabrication of the pie-shaped harvester, the use of low-stress structural material was emphasized. Nevertheless, the first device showed a very high natural frequency (about 2.4kHz) during the vibration tests. Such a high natural frequency suggests that the structure suffers from a high average residual stress (100MPa) which is out of the design range.

Consequently, a complete stress analysis and control process has been conducted during the fabrication of the 3rd generation device to engineer the average stress down to less than 10MPa. To achieve such a low residual stress in the structure, it is required to select the appropriate deposition method for each layer and measure the effective stress from each step. To estimate the stress from each film, the curvature of every wafer has been monitored by the wafer curvature measurement system (KLA-Tencor FLX 2320) before and after every step [120–122]. Some steps such as thermal oxidation and LPCVD deposit the film symmetrically on both side of the wafer. Therefore, the film should be stripped from one side of the monitor wafers to measure the average stress from the corresponding film. After a comprehensive sets of measurements and analysis, the residual stress from each layer was estimated (Table 4.1).

Although the average residual stress is the main parameter that should be controlled in the doubly-clamped structures, the distribution of the residual stress is also important. If the residual stress distributes unsymmetrical with respect to the neutral axis of the beam, a bending moment will be formed as a result. This bending moment may apply a large strain on the anchors. A crack can be generated at the stress-concentration points and will be propagated during the release and result in device failure.

Figure 4-11 shows a device that has been broken and buckled as a result of un-

Table 4.1: Measured average change in the bow of the wafer from the films in the structure. The KLA-Tencor FLX 2320 system has been off-calibration during the measurements and all the values have been updated accordingly.

Film	Thickness (nm)	Measured ΔBow(μm)	Calibrated ΔBow(μm)	Avg. Stress (MPa)
Thermal Oxide Wet @1050°C	970	63	27.4	-300
LPCVD Nitride VTR Tube	1560	-91	-39.5	+275
Annealed LTO @700°C for 1hr	700	6	2.6	-40
RTAed ZrO_2 @700°C for 60s	260	-20	-8.7	+365
RTAed PZT @700°C for 60s	270	-35	-15.2	+695
LF-PECVD SiO_2 STS-CVD	1000	80	34.8	-380
HF-PECVD SiO_2 PlasmaTherm	805	NA	20	-268

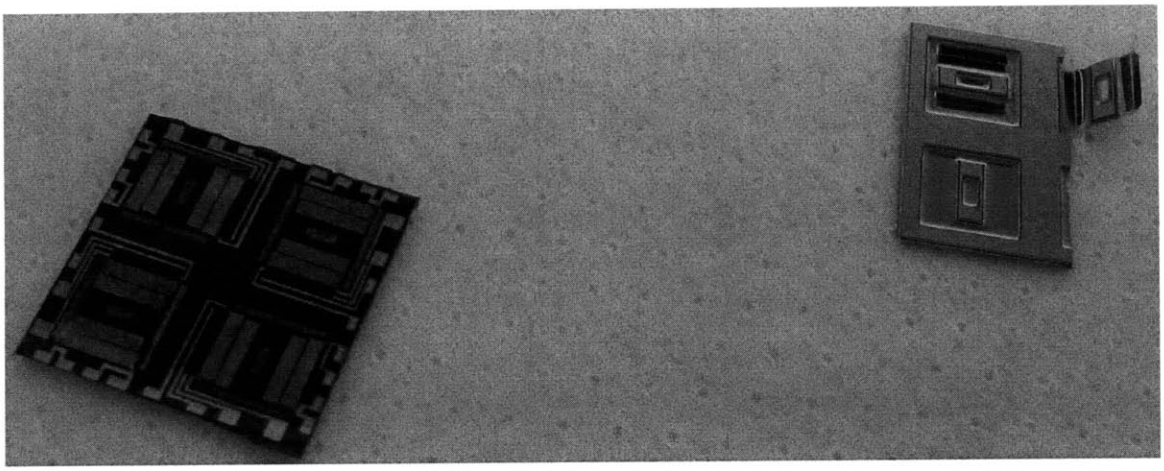

Figure 4-11: Asymmetrical distribution of residual stress with respect to the neutral axis may generate a crack at the anchors and brake the device. The released device (right) is broken and buckled upward to release the bending moment resulted from the stress distribution.

balanced stress distribution. Highly compressive PECVD oxide on top of the beam cancels out the axial force from the tensile LPCVD nitride on the backside of the beams. Nevertheless, the resulting bending moment has broken the beam exactly at its anchor point. The beam has buckled upward (in the picture) in such a way that both bending components can be relaxed accordingly. Therefore, the composition of the structure has been changed and a thick layer of compressive thermal oxide ($1\mu m$ thick) is grown on the silicon wafer to partially cancel out the tensile nitride and PZT. A final compressive PECVD nitride/oxide layer which acts as the passivating layer has been tuned carefully to fully cancel out the rest of the axial stress and also make a symmetric stress distribution with respect to the neutral axis.

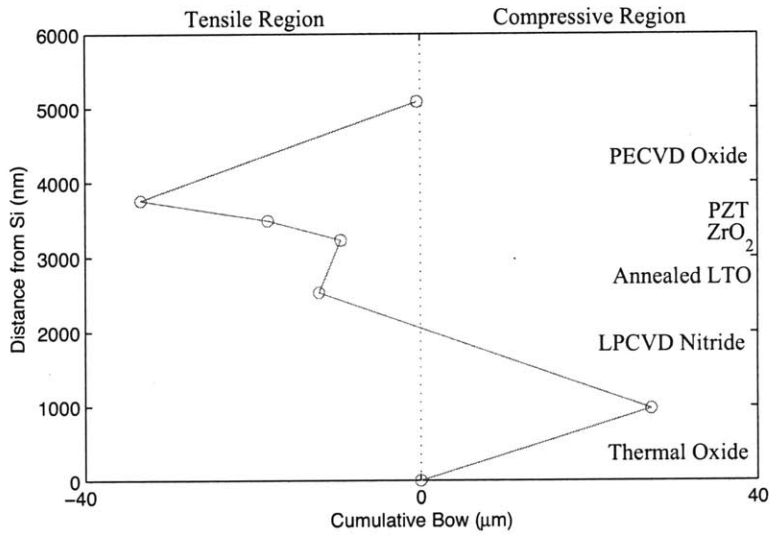

Figure 4-12: The stress distribution across the thickness of the structure.

4.2.2 Structural Layer

As explained in Section 4.2.1, the composition of the structural material is re-engineered to control the stress in the beams. The thickness of the thermal oxide has been increased from $200nm$ to $1\mu m$ to partially cancel out the stress from tensile layers including the LPCVD nitride and the PZT layers. Growing such a thick layer of oxide requires wet oxidation at high temperature ($1050°C$) for a long time (186 mins).

Subsequently, the same recipe used in the pie-shaped structure (4.1.1) was implemented to deposit about $2\mu m$ thick LPCVD nitride. Nevertheless, the tube went out of a supply gas during the operation and the actual thickness of the film was $1.561\mu m$. Therefore, the rest of the steps was adjusted accordingly to control the stress.

The wafers transferred directly from the VTR tube to the LTO tube to avoid intermittent contamination or RCA-cleaning.

Equipment	tube 6C-LTO at ICL
Recipe	400C 53A SPK
Deposition time	2hrs 12mins 5secs
Thickness target	$700nm$

Afterward, all the layers have been annealed in the tube 5B at 700°C for one hour. This annealing step densifies the porous LTO and also stabilizes its residual stress. Otherwise, the residual stress of the LTO layer may change due to the next high-temperature steps including the annealing of the ZrO_2 and PZT layers [123,124]. Consequently, the stress measurement from stripping the LTO layer from the annealed structure can give us a reliable estimate of its effect on the final device. The annealing step can be done at a higher temperature and for a longer time to improve the density and the stability of the stress levels. Nevertheless, it will add some undesirable tensile stress to the nitride and LTO layers.

Equipment	tube 5D-Anneal at ICL
Recipe	2A700
Annealing time	1hr

4.2.3 Active Layer

The 3rd generation employs an active layer which is similar to that of the pie-shaped design with some modifications. Both ZrO_2 and PZT solutions were syringed through $0.2\mu m$ syringe filters on the substrate to minimize particulate contamination. In addition, three pyrolysis steps have been replace by two steps to minimize the processing time and improve the film quality. In case of ZrO_2, the box furnace annealing has

been replaced by the rapid thermal annealing to decrease the processing time and avoid the contamination from the residues in the box furnace.

Solution	9%wt ZrO2 solution by Mitsubishi Materials
Spin-coat	500rpm(5secs)-2500rpm(25secs)
Drying/Pyrolysis	$200°C$(60secs)/$390°C$(300 secs)
Target thickness	$80nm$-$100nm$ per coat
Etch	Diluted (1:20) BHF solution(10secs)
Anneal	$700°C$(60secs), RTA AG Associates Heatpulse 410

PZT Processing

In case of PZT, a totally new solution, G3-type by Mitsubishi Materials, has been used for the first time. This solution is supposed to deposit a very thick film of PZT (up to 800nm/layer) in a single coat. Nevertheless, our measurements showed a much lower thickness (about 265nm/layer) can be achieved in reality. Nevertheless, even this thickness is equal to total PZT thickness achieved by 3-4 coats of E1 solution. Furthermore, at least one extra coat is possible to obtain a PZT film thicker than $0.5\mu m$.

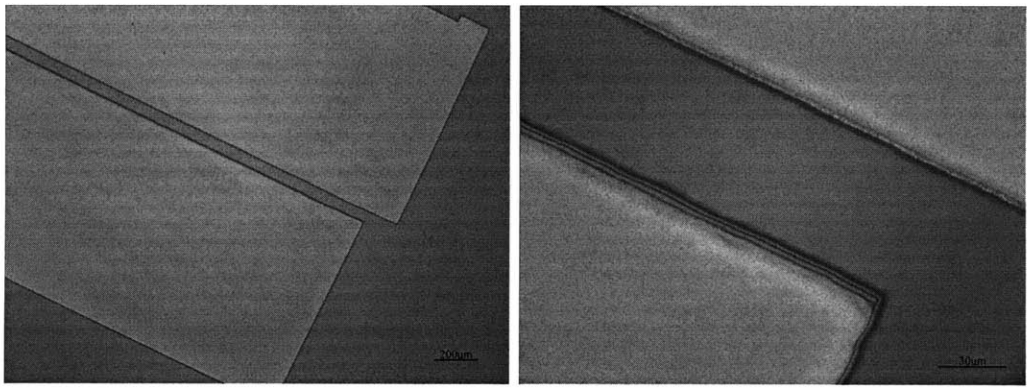

Figure 4-13: Patterned ZrO_2/PZT after annealing.

In case of G3-type solution, the pyrolysis temperature (450°C) is higher than the maximum range of the hot-plates in the TRL. Therefore, the PZT box furnace has been used for the final step of the pyrolysis. The previous wet-etching process using diluted BOE solution seems to suffer from deep undercut and also some PbO residual

on the substrate. Therefore, Hydrochloric Acid has been added to the etching solution to solve these issues and reach a high-quality patterning.

Solution	25%wt G3-type PZT solution by Mitsubishi Materials
Spin-coat	500rpm(5secs)-2500rpm(55secs)
Drying/Pyrolysis	$200°C$(60secs)/$450°C$(300secs-600 secs)
Target thickness	$270nm$ per coat
Etch	DI Water (1000cc):HCl (300cc): BHF (100cc)
	dip in the etching solution/spray by DI water repeat few times
Anneal	$700°C$(60secs), RTA AG Associates Heatpulse 410

Top IDT Electrodes

The configuration of IDT electrodes has modified from the pie-shaped design to the redundant configuration explained in Section 3.7.1. More redundancy has been implemented by providing separate pads for every pairs of electrode. Therefore, the total number of pads have been increased from 2 in pie-shaped design to 32 in the 3rd generation. This requires a substantial amount of wire-bonding during the packaging step.

Figure 4-14: XeF_2 can attack the IDT electrodes especially by undercutting the adhesion layer (Ti).

Titanium/Platinum and Titanium/Gold electrodes were tried in the pie-shaped

structure. Nonetheless, the electrodes were attacked and delaminated during a long XeF_2 exposure as shown in Figure 4-14. This problem was solved by adding the passivation layer on top of the active area. However, the XeF_2 still can attack the electrode at the pad areas which makes the wire-bonding impossible in some devices. Consequently, Aluminum electrodes with Titanium as the adhesion layer was tested in the 3rd generation. Unlike gold and platinum, Aluminum doesn't form any volatile fluoride and thereby provides an extremely well selectivity to the XeF_2 etching. Further processing of the 3rd generation is slightly affected by changing the electrode material from gold or platinum to aluminum. After the lift-off, no high-temperature processing is allowed due to the low melting point of Aluminum (660°C). Moreover, Piranha solution attacks aluminum and cannot be used anymore for cleaning the wafer.

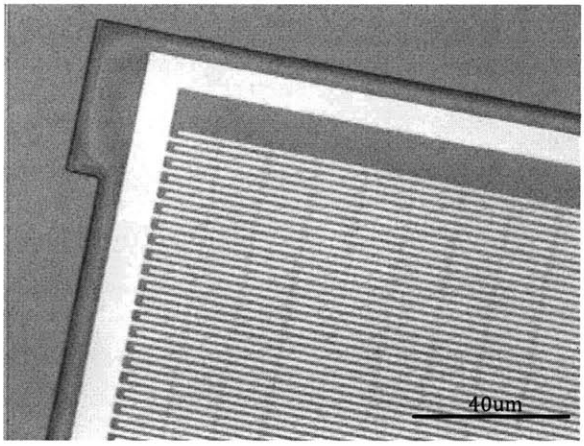

Figure 4-15: 200Å Ti/2000Å Au are e-beamed and patterned by lift-off to form the IDT electrodes. The electrode material has been switched to Aluminum in further batches to avoid the attack by XeF_2.

Another modification has been the change in the finger width (w_f) and also the gap size between the fingers (w_g). Wide fingers ($w_f = 10\mu m$) and gap size ($w_g = 5\mu m$) were implemented in the pie-shaped harvester. Nevertheless, only the PZT underneath the gaps are active and contribute to charge generation in d_{33} mode. To increase the active area and the power density of the device, the width of the electrodes has been decreased to $4\mu m$ in the 3rd generation. Furthermore, the PZT layer in the pie-shaped device did not show the expected performance after poling.

It suggests us that an smaller gap distance is needed to improve the poling and piezoelectric properties. Therefore, $4\mu m$ gap size has been implemented in the 3rd generation which results in improvement in poling and charge generation capabilities.

Lithography	AZ-5214 coat (2000rpm)/Exposure 1.4 secs/Flood Exposure 48secs
Electrodes	Ti/Al (200Å/1000Å)
Equipment	EBeamFP Temescal Model FC2000
Liftoff	acetone bath+ultrasound shaking (10 mins)

4.2.4 Passivation Layer

The passivation layer plays more functions in the 3rd generation of energy harvester compared to the pie-shaped one. It passivates the active layer from any electrical shortage and chemical reaction, acts as the etch stop and most importantly has been used as the tuning knob for stress engineering. A double layer of PECVD nitride/oxide has been used in the 3rd generation as well, but the thickness is much higher and the deposition method has been carefully controlled.

The PECVD machine at TRL, STS-CVD (by Surface Technology Systems), has a dual-frequency deposition capability which makes it a powerful tool for controlling the film stress. The machine has the possibility of alternating the frequency between high frequency plasma (13.56MHz) and low frequency mode (380kHz). The ion bombardment in the deposition is different for each of these two modes. Consequently, the residual stress in the film would be changed accordingly. Especially in case of silicon nitride, the stress can be controlled anywhere from 1100MPa compressive (0%HF-100%LF) up to 400MPa tensile (100%HF-0%LF) by varying the time intervals during each mode. The experimental residual stress as a function of mode ratio is shown in Figure 4-16.

In Section 3.6, a guideline is presented in choosing the structural properties to improve the system performance. It implies that the nonlinear properties can be enhanced by employing stiffer materials and also reducing the average residual stress. The same argument can be made for the passivation layer. Considering the fabrication limitations, the device should be passivated with a layer of nitride followed by a layer

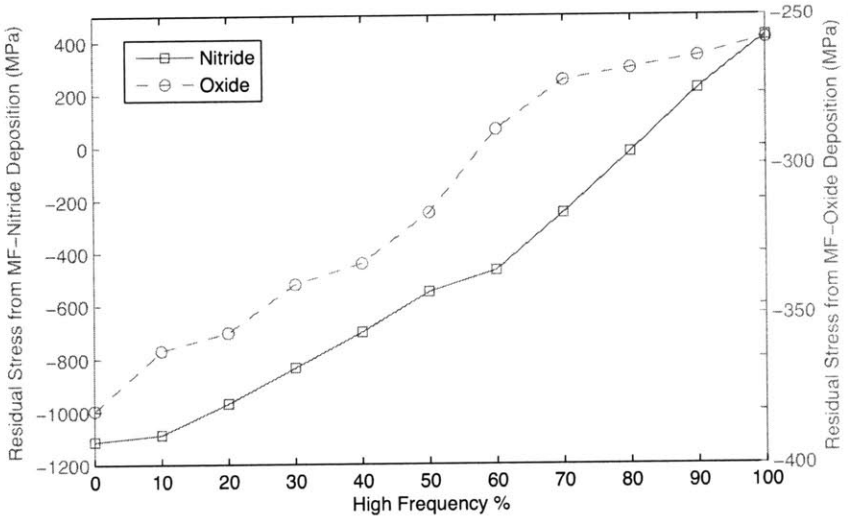

Figure 4-16: The residual stress of the Plasma Enhanced Chemical Vapor Deposited (PECVD) films can be controlled by changing the ratio of high frequency mode interval to the total time. (Data courtesy of Donal Jamieson from MTL).

of oxide. Nevertheless, the thickness of each layer and its corresponding deposition method are yet to be determined. Nitride has a higher stiffness ($Y_{SiN_x} \approx 200GPa - 300GPa$) compared to the oxide ($Y_{SiO} \approx 50GPa - 70GPa$). In addition, a wide range of residual stress is achievable only in case of the PECVD nitride as shown in Figure 4-16. Therefore, the PECVD nitride gives the designer more control knobs in tuning the stress and also the nonlinear stiffness. Nevertheless, there are some fabrication limitation on the maximum achievable thickness of the PECVD nitride layer without cracking.

From the other side, the PECVD oxide layer has a lower stiffness and provides a much smaller range of possible residual (250MPa-350MPa compressive). Nevertheless, the PECVD oxide provides some other opportunities. The thickness of the PECVD oxide can be increased up to several microns without any crack in the film. In addition, unlike the nitride, the oxide layer is very selective to the XeF_2 etching. Furthermore, the stress of the film is pretty much fixed and doesn't variate with small variations in the process. Finally, the PECVD oxide can support a higher electric field without breakdown compared to the nitride layer.

During the fabrication of the 3rd generation device, the STS-CVD machine was down due to some part problem and couldn't be used. Accordingly, a Versaline PECVD machine (by PlasmaTherm) at the Integrated Sciences Cleanroom and Nanofabrication Facility (Boston College) has been used as the only alternative to deposit the passivation layer. Nevertheless, the machine only provides a single frequency mode of deposition (High Frequency) and the stress of the deposited film can only be controlled by changing the gas ratios and also the plasma condition [125]. Considering the machine limitations, two recipe were developed for the nitride layer and the oxide layer.

Dielectric	Compressive Nitride
Equipment	Versaline LoadLock, PlasmaTherm
Deposition Temperature	$300°C$
Gas flow	SiH_4=200sccm, NH_3=6.3sccm,
	He=1050sccm, N_2=350sccm
Gas Pressure	1000mTorr
RF Power	100W
Deposition Rate	24-26nm/min

Dielectric	Compressive Oxide
Equipment	Versaline LoadLock, PlasmaTherm
Deposition Temperature	$300°C$
Gas flow	SiH_4=200sccm, N_2O=900sccm, N_2=500sccm
Gas Pressure	1000mTorr
RF Power	25W
Deposition Rate	40nm/min

The final passivation layer consists of a thin layer of PECVD nitride (100nm-130nm) followed by a thick layer of PECVD oxide ($1.2\mu m - 1.8\mu m$) has been deposited for stress cancellation. The final thickness of the oxide layer is subsequently trimmed and controlled by reactive ion etching using PlasmaQuest. This process requires intermittent stress measurements to ensure a very well controlled final stress.

4.2.5 Etching and Release

To etch the structure and release it in the final form, a fabrication process similar to the pie-shaped harvester has been used. Nevertheless, some minor modifications have been implemented to improve the process yield rate.

Reactive Ion Etching

Reactive Ion Etching (RIE) has been employed as the main method for etching and patterning the structure with straight sidewalls. PlasmaQuest is the only available electron cyclotron resonance (ECR) plasma etcher that can be used at TRL for etching dielectrics. The basics of ECR plasma etching has been explained in [126].

The original etching recipes have been modified and a new recipe has been introduced that can provide a very high dielectric etch rate (100nm/min) and considerably slow photoresist etching. This recipe has been used to pattern all the dielectric layers including passivating PECVD oxide and nitride, annealed LTO, LPCVD nitride and finally the thermal oxide.

Process	Fast dielectric RIE
Equipment	PlasmaQuest ECR/RIE
Etching Temperature	$25°C$
Gas flow	O_2=5sccm, He=15sccm, CF_4=40sccm
Plasma power	200W (microwave) + 50W (RF Chuck)
Etch rate	100nm/min

The passivation layer has covered the surface of the device. The dielectric should be patterned to leave some opening to access the pad area for further wafer-bonding purposes. A mask has been used especially for patterning the passivation layer which defines the openings in the PECVD layers (Figure 4-17). The etching can be controlled by time and also by visual inspection of the wafer till no dielectric remains on the aluminum pads. Some electrical testings can also be helpful to determine the completion of the etching. Furthermore, a wet etching step (BOE etching) can be

used initially to completely pattern the oxide layer and then a short time-based RIE can pattern the thin PECVD nitride.

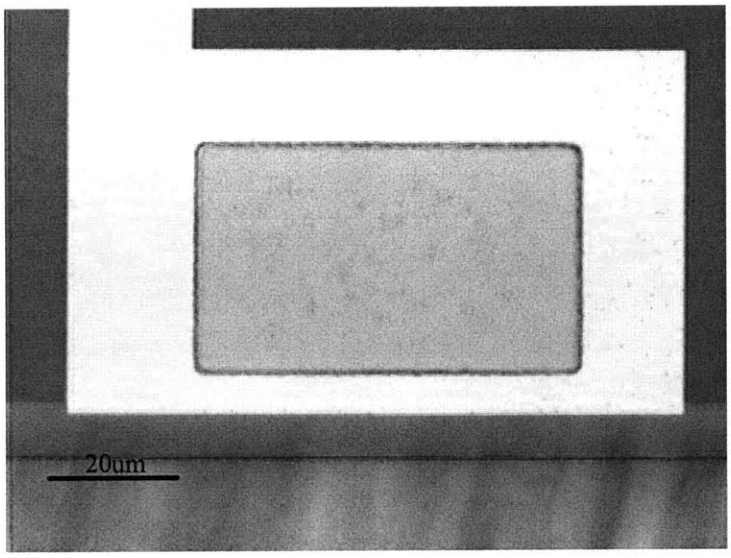

Figure 4-17: An opening has been etched in the passivation layer at the pad areas. Each device will be connected electronically to the package through wire-bonding to these pads. Gold pads have been slightly over-etched by the XeF_2 etchant, but this problem has been solved by using Aluminum pads.

Subsequently, the structural layers should be patterned from top and back of the wafer. The wafers are cleaned in microstrip solutions and ashed for one hour before the lithography. Both sides of the wafers are coated with a thick layer of photoresist. The RIE using the new recipe can etch through the whole thickness of the structural layer within less than an hour. The wafers are flipped and the backside is also etched and patterned similarly.

Shallow silicon etching

An optional short step has been added to the process after dry etching the structural layer. About 10-15μm silicon is etched from the wafer's front side using XeF_2 or DRIE. This shallow etching ensures a smooth automatic device separation during the final DRIE step. Each device has been isolated by a square-shaped trench in the wafer which is being etched from both sides during the fabrication. Consequently, each device will be separated from the whole wafer by etching through these trenches before

the final release of the beams. Figure 4-18 shows the automatic device separation process which eliminates the need for a harsh process like die-sawing.

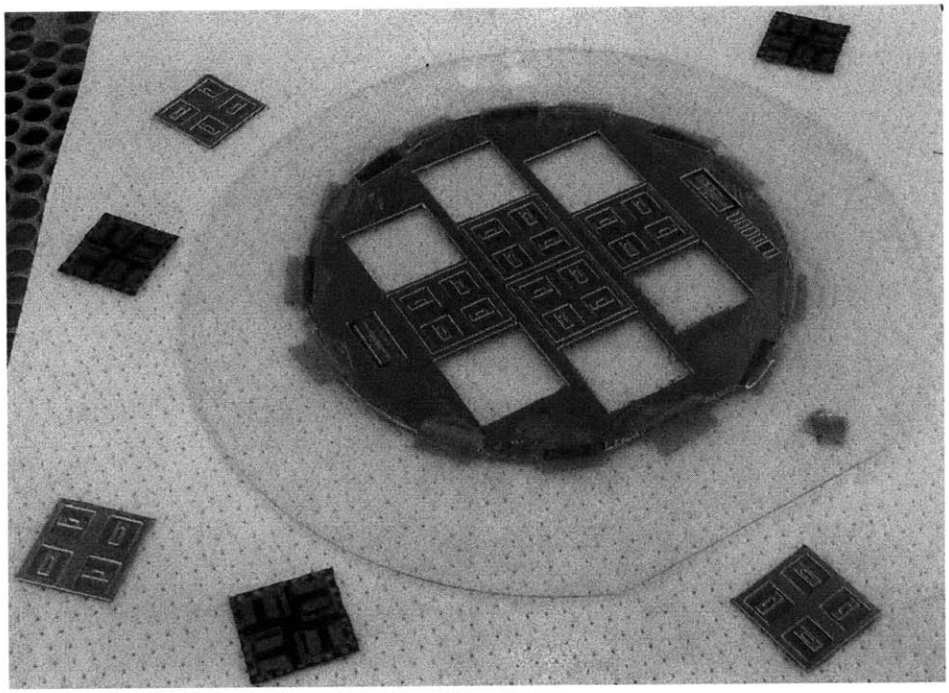

Figure 4-18: Pre-released devices are cut and separated from the main wafer automatically at the end of DRIE step. Each device will be fully released later by XeF_2 etchant. The 4" wafer is simply mounted on a 6" glass wafers by Kapton tape.

Deep Reactive Ion Etching

Deep reactive ion etching (DRIE) has been used to etch the silicon through the thickness of the wafer and form the structure. Among various etching recipes, *MIT56* has a uniform and high etch rate and has been used. The etch rate is about $3\mu m/min$, but it changes with the mounting conditions and also it varies across the wafer. *STS1* is the only DRIE machine that accepts gold-contaminated wafers. The wafer diameter is limited to only 6-inch wafers and a wafer-mounting procedure is required for 4-inch wafers as explained in Section 4.1.4. Conventionally, annular rings of photoresist was coated on a 6" glass wafer. Subsequently, using acetone-soaked brushes some radial channels were made that allow the outgas of photo-resist during the process and also the flow of acetone for final release.

Recipe	MIT56
Equipment	STS1
Gas flow	switching SF_6=105sccm (15s)/C_4F_8=40sccm (9s)
RF plasma power: Coil	800W etch / 600W passivation
RF plasma power: Plate	120W etch / 60W passivation
Chamber process pressure	27mTorr
APC angle	60°
Etch rate	$3\mu m/min$

Nevertheless, even with a perfect wafer-mounting, the detachment of the wafer after the process is very troublesome and some devices may break meanwhile. Consequently, the 4" wafers are simply mounted on 6" glass wafers using Kapton tape as shown in Figure 4-18. Nevertheless, the heat conduction is worse and the photoresist can be burned and etched away very fast. Nevertheless, the patterned thick dielectric layers on back of the wafer would act as a hard mask afterward. Using this method, each device is easily separated from the wafer as the silicon is etched completely at that spot while the rest of devices can be further etched. Accordingly, the problem of etching non-uniformity (which can be up to 10%-20% across the wafer), can be alleviated.

Each device undergoes a cleaning process which includes solvent-based cleaning in micro-strip and also ashing in oxygen plasma (1000W) for 1-2 hours.

XeF_2 Etching

XeF_2 has been used as the final etching step which can smoothly release the beams and finalize the process. Implementing thick oxide layers ($1\mu m$ TOx and $1-2\mu m$ PECVD oxide) on both sides of the beams provides a very high selectivity to a long XeF_2 etching step which was not possible before. This selectivity makes it possible to completely etch the silicon underneath the beams remained from the nonuniform DRIE etching without etching the device structure.

Figure 4-19 shows the optical image of a device after XeF_2 etching which has been fully released. No defects or problem can be seen in the structure and a prefect

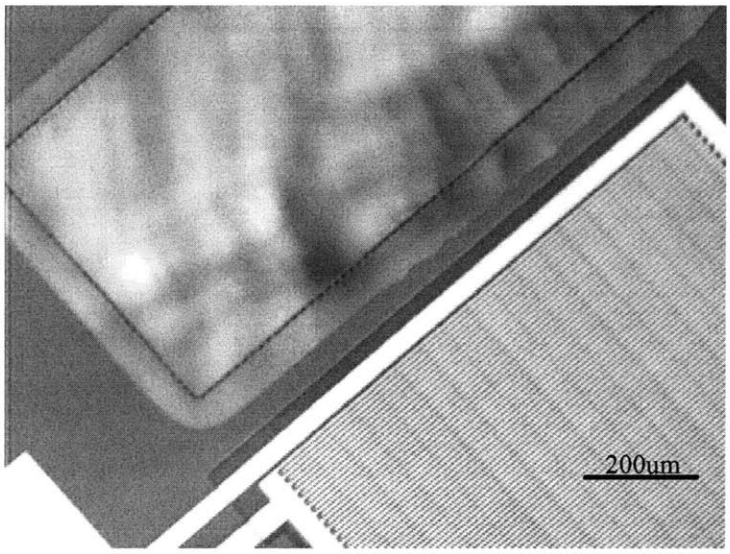

Figure 4-19: The optical image of a fully released 3rd generation device.

fabrication process is demonstrated. Another optical image (Figure 4-20) depicts the active area of the device from the other side of the device. The diaphragm is optically transparent and the IDT electrodes can be clearly seen through the diaphragm. The edge of the beams are very sharp and clear and no defects can be seen.

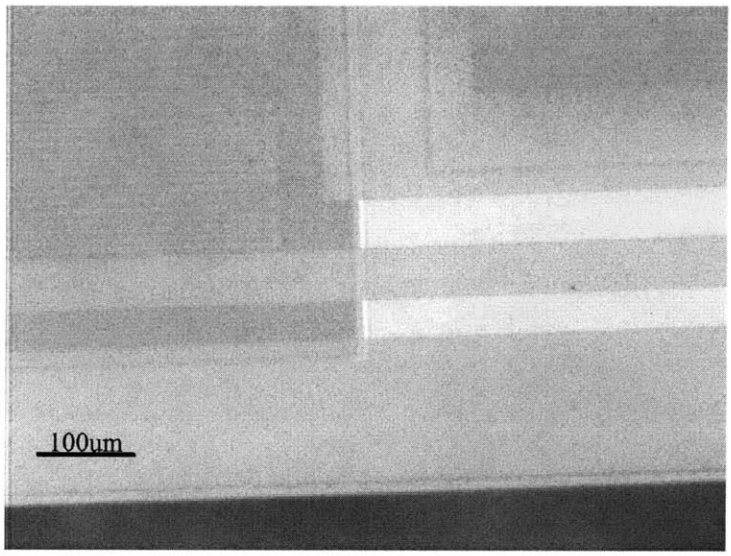

Figure 4-20: The optical image of a fully released 3rd generation device from its backside. The IDT electrodes are visibly through the optically transparent structural layer.

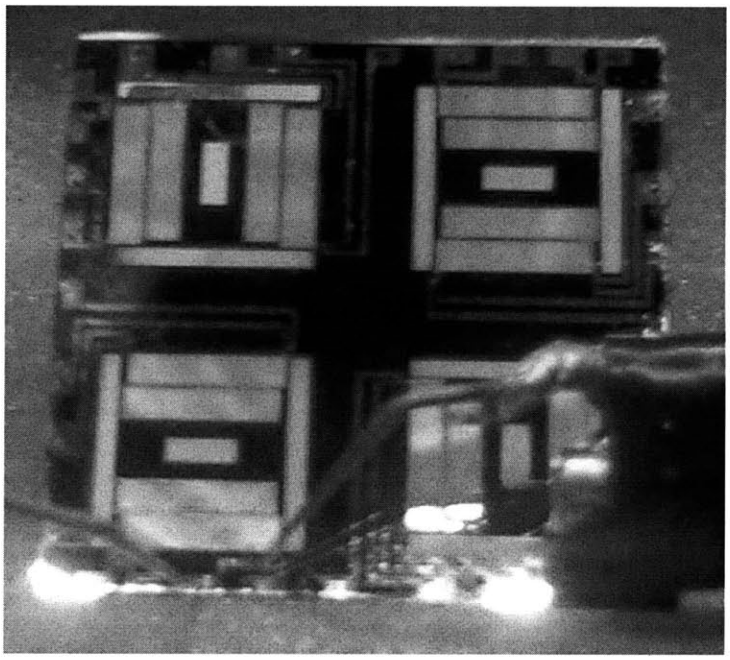

Figure 4-21: A complete device under the probe-station.

Chapter 5

Testing and Discussion of Results

5.1 XRD Crystallography

X-ray crystallography is a method of determining the crystal structure based on Bragg's law. A beam of X-rays strikes the sample at different angles and the diffracted signal is collected in a detector. The crystal structure can be determined based on position and the intensity of the peaks in the collected signal. A healthy PZT structure with a strong perovskite phase is necessary for the MEMS-scale piezoelectric energy harvesting. At early stages of the processing, XRD can be used to determine the crystal structure of the annealed thin-film PZT.

A Rigaku RU300 diffractometer at the Center for Materials Science and Engineering (CMSE) has been used for evaluating the crystal structure of the PZT film. The XRD results for type-E1 and type-G3 PZT have been measured and shown in Figures 5-1 and 5-2, respectively. Both samples show strong peaks of perovskite phase which verifies the healthiness of the annealed PZT. Type-E1 PZT gives a strong peak at the $< 110 >$ orientation plus a mixture of weak $< 100 >$, $< 111 >$, $< 200 >$, $< 201 >$ and $< 211 >$ orientations. Type-G3 PZT shows a perovskite phase which is highly concentrated at $< 111 >$ direction.

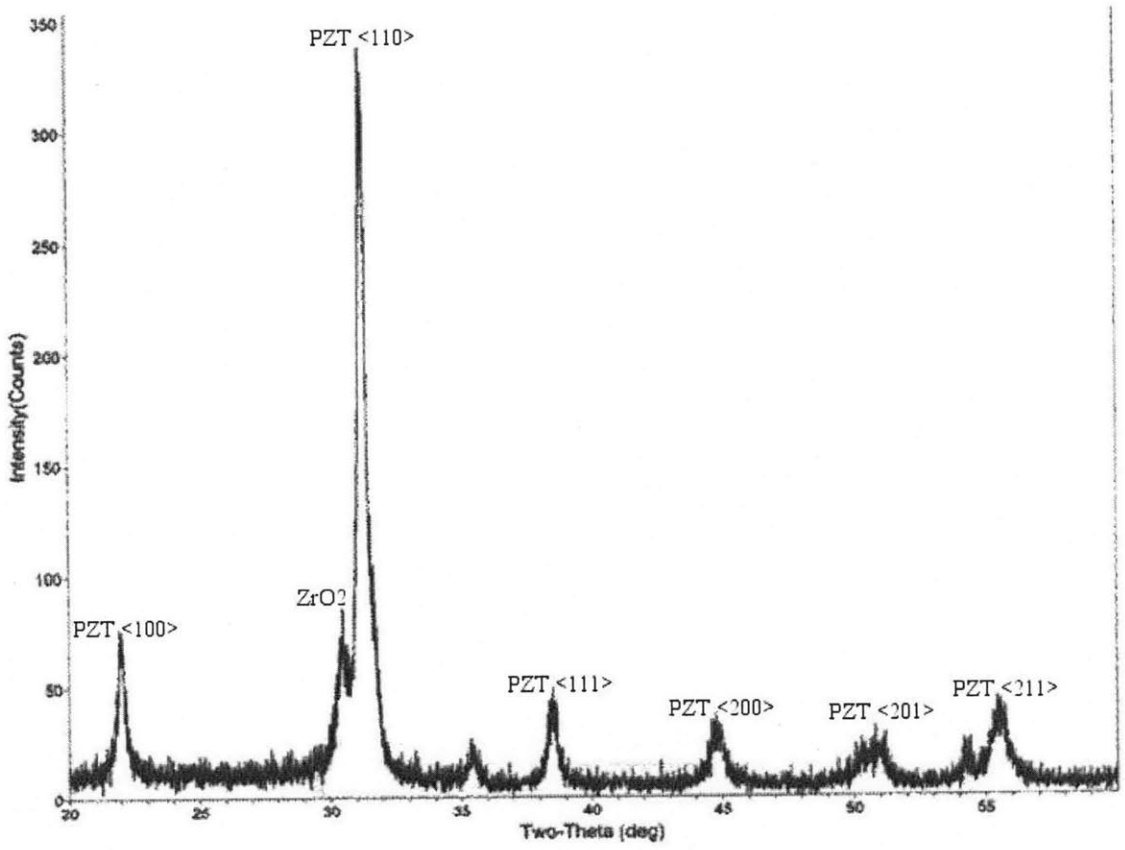

Figure 5-1: X-Ray diffraction crystallography shows strong < 110 > perovskite peak for type-E PZT.

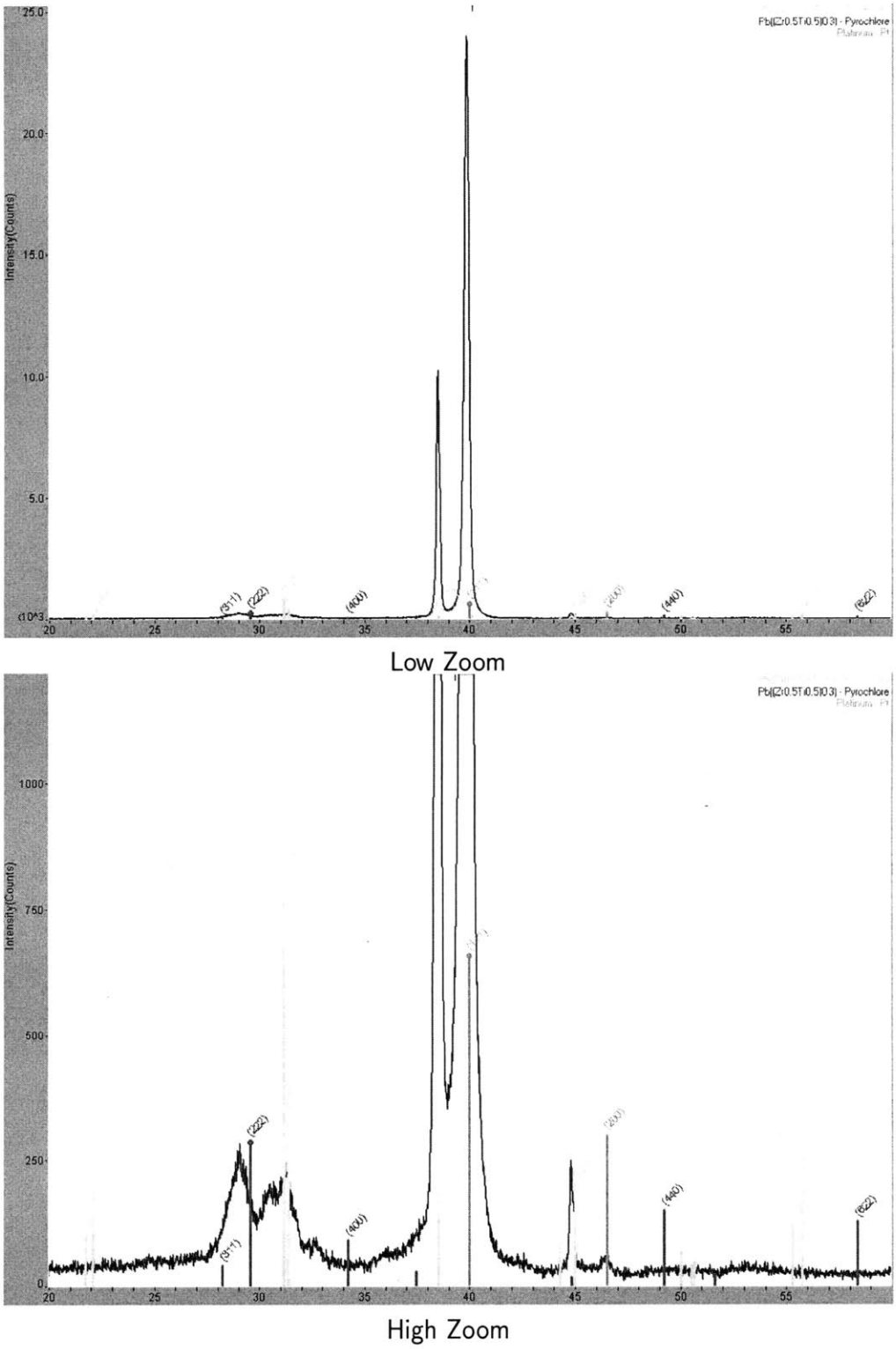

Figure 5-2: Type-G3 PZT (thick film) crystallized mainly at the < 111 > Perovskite phase.

5.2 Packaging

5.2.1 Pie-shaped device

A complete released device should be packaged for further electrical and electromechanical testings. Based on the size of the device, various sizes of Ceramic Pin Grid Array (CPGA) packages have been used in this work. The main parameter in selecting the right package has been the cavity size. The pie-shaped harvesters have been fabricated at various sizes without specific consideration of the packaging process.

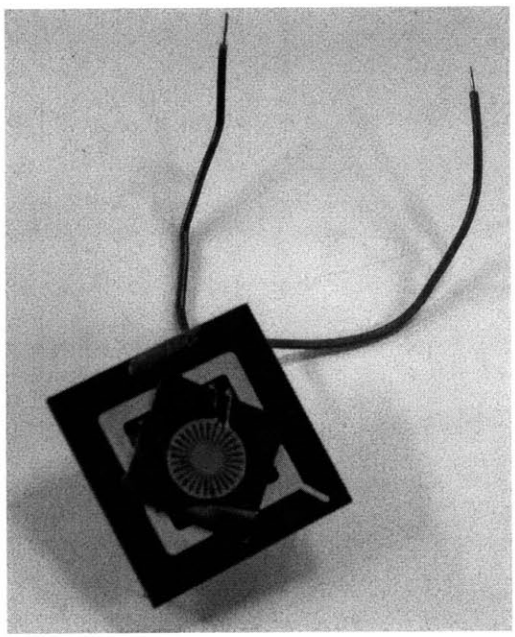

Figure 5-3: Released device is super glued to a PGA package. Electrodes are wire-bonded to the package's pads.

As shown in Figure 5-3, each released device is super glued to a CPGA package in such a way that the proof mass is being located on top of the cavity. It gives the proof mass enough space for motion in response of the base vibration. During the electromechanical-test, the package acts as the vibration base for the beams and transfer the ambient vibration to the device. The pads on the device are gold wire-bonded at the opening areas to the package's pads. Heating the substrate up to $100°C$ can facilitate the bonding to the platinum pads.

5.2.2 3rd generation

Based on the experiences from the pie-shaped device, the packaging has been considered in the design of the 3rd generation device. The device has been designed based on the *CPG14447* package by *Spectrum Semiconductor Materials Inc.* [127]. The package has a cavity size of 0.700"x0.700"x0.02" [17.78mm x 17.78mm x 0.51mm].

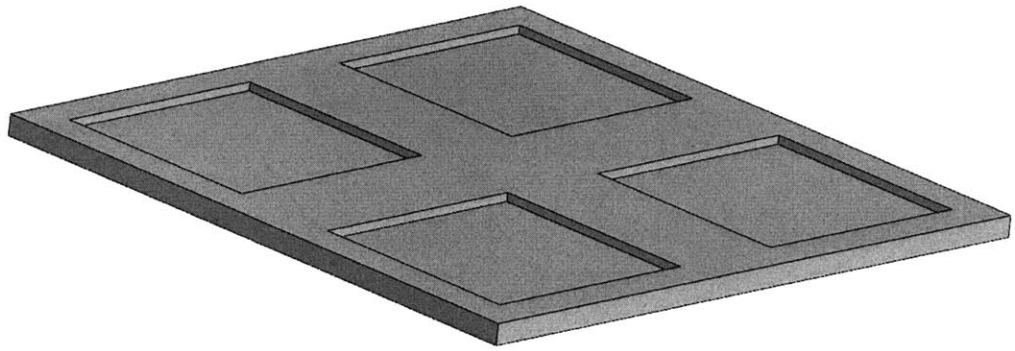

Figure 5-4: A silicon base has been fabricated by KOH etching of a silicon wafer. It fills the cavity of the CPGA package, acts as the base for the device and provide enough room for the proof mass downward motion.

As shown in Figure 5-4, a base has been fabricated out of silicon to fill the cavity and also provide enough room for the proof mass motion. Similar 4-inch silicon wafers with $2\mu m$ LPCVD nitride on both sides have been used to fabricate the base and also the proof mass shown in Figure 3-24. The nitride layer has been patterned dry etched on both sides as the hard mask. Subsequently, the wafers have been soaked in 30% KOH solution at 80° for about three hours to etch the structure.

The size of the base (17mm x 17mm x 0.55mm) has been designed in such a way that it fits the cavity and fills its depth. The main device itself is a little bit bigger (18mm x 18mm x 0.55mm) than the cavity size to minimize the wire-bong distance. The position of aluminum pads on the device have also been designed based on the pads of the package. Only 32 pins out of the 144 pins of the package are required for the 3rd generation device. It gives a redundancy to select the most accessible pins for wire-bonding. Figure 5-5 shows the selected pad configuration. Subsequently, the aluminum pads on the package device are wire-bonded to the designated pads on the CPGA package as shown in Figure 5-6.

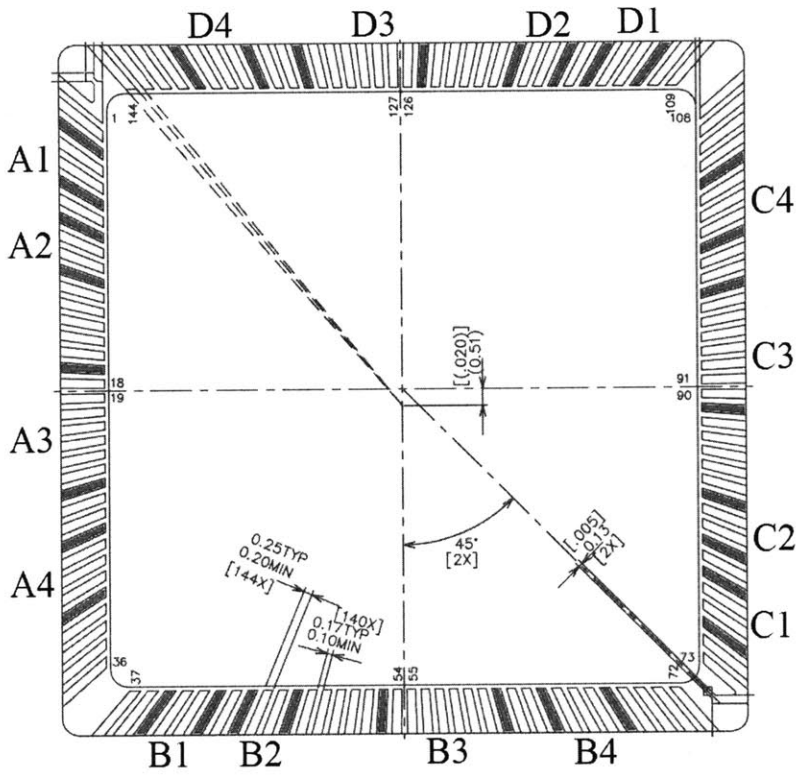

Figure 5-5: Each cell of a device has four pairs of electrodes which are wire-bonded to the designated pads in the package (marked in red).

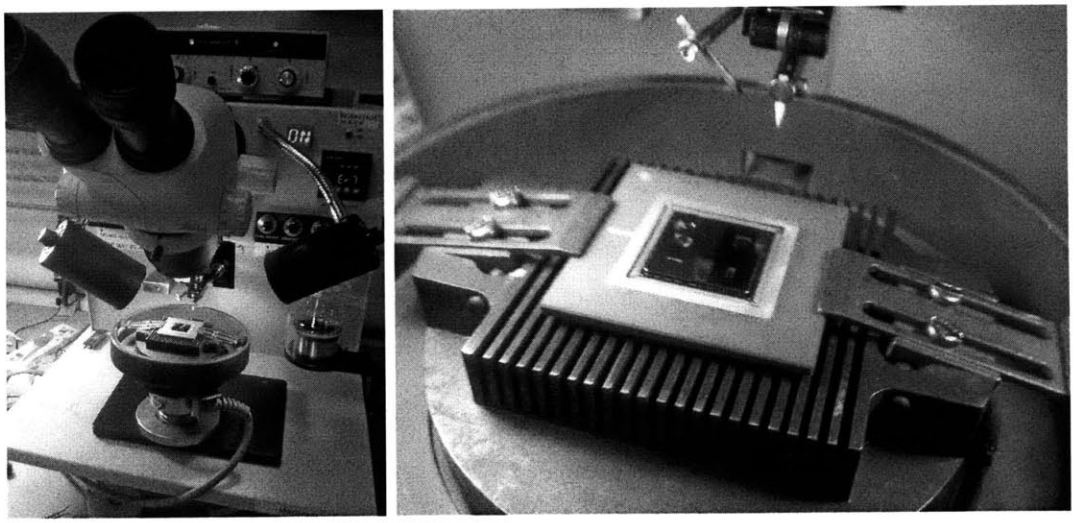

Figure 5-6: The wire-bonding setup. Aluminum pads on the packaged device are bonded by gold wires to the pads on a ceramic pin grid arrays (CPGA) package.

5.3 Testing Board

The ceramic packages are mounted on 0.042" thick perforated printed circuit boards (PCB) for further electrical connection and also electromechanical testing. In case of pie-shaped harvester, the pins of each package were soldered to the board (Figure 5-7). Accordingly, each device required its own PCB. The generated signal from each device can be measured by a low-noise shielded coaxial cable which is connected a BNC coaxial connector on the testing board.

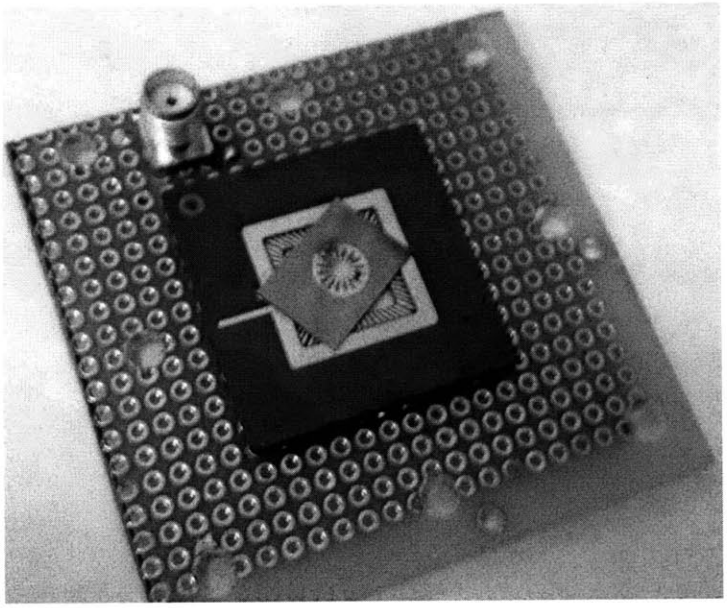

Figure 5-7: The testing board for a pie-shaped device: each package has been directly soldered to a perforated PCB.

For the 3rd generation devices, a single universal testing board has been developed. Each package can be easily mounted on a socket which has been fixed in the center of the board. 8 slide-style DIP switches were positioned around the socket on the board. Each pair of electrodes can be connected to or disconnected from the main electric bus on the board via these DIP switches. Therefore, any combination of the electrodes can be accessed for electrical and electromechanical testings. The addressability of each electrode enables us to electronically disable the electrically-shorted sections of the system. The whole testing board with a complete device is shown in Figure 5-8.

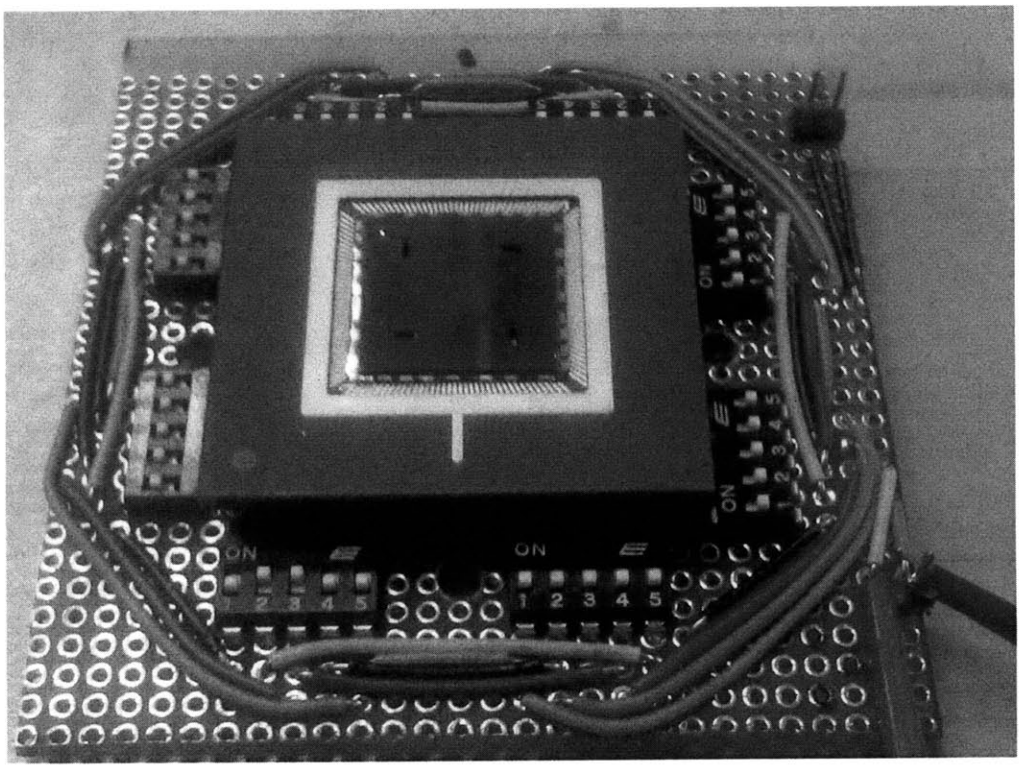

Figure 5-8: Packaged devices can be easily mounted on the testing board for P-V measurements and electromechanical vibration tests. Each pair of electrode can be independently controlled by the DIP switches on the testing board.

5.4 P-V Measurements

The piezoelectricity of a material is described by its hysteretic behavior by a Polarization-Voltage measurement. When a sample of PZT is subjected to an increasing electric field, the dipoles become aligned with the field and polarization increases. When the field has increased to a certain value in which all the dipoles are aligned with the field, polarization will cease to increase. The material then reaches the saturation point, with saturation polarization P_s. If the field is now reduced to zero, dipoles will become less aligned.

However, they do not return to their original alignment, since they are bounded to a preferred direction defined by the applied field during the first part of the hysteresis. Since there is still a high degree of alignment, the polarization does not fall back to zero but to a value somewhat lower than the saturation polarization known as the remnant polarization P_r.

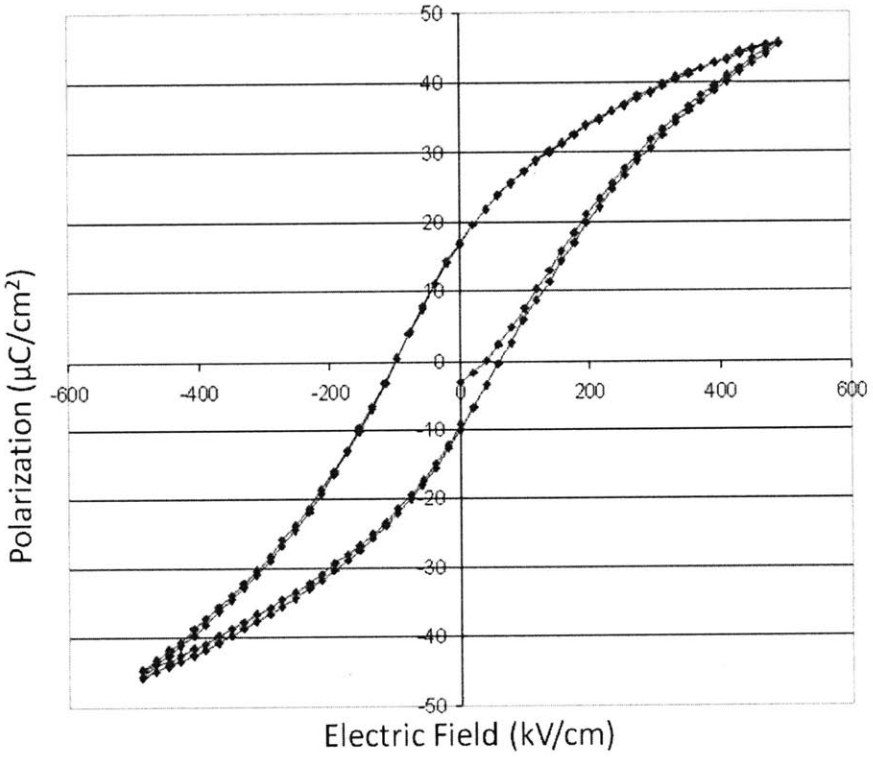

Figure 5-9: Measured P-V curve for the poled pie-shaped energy harvester.

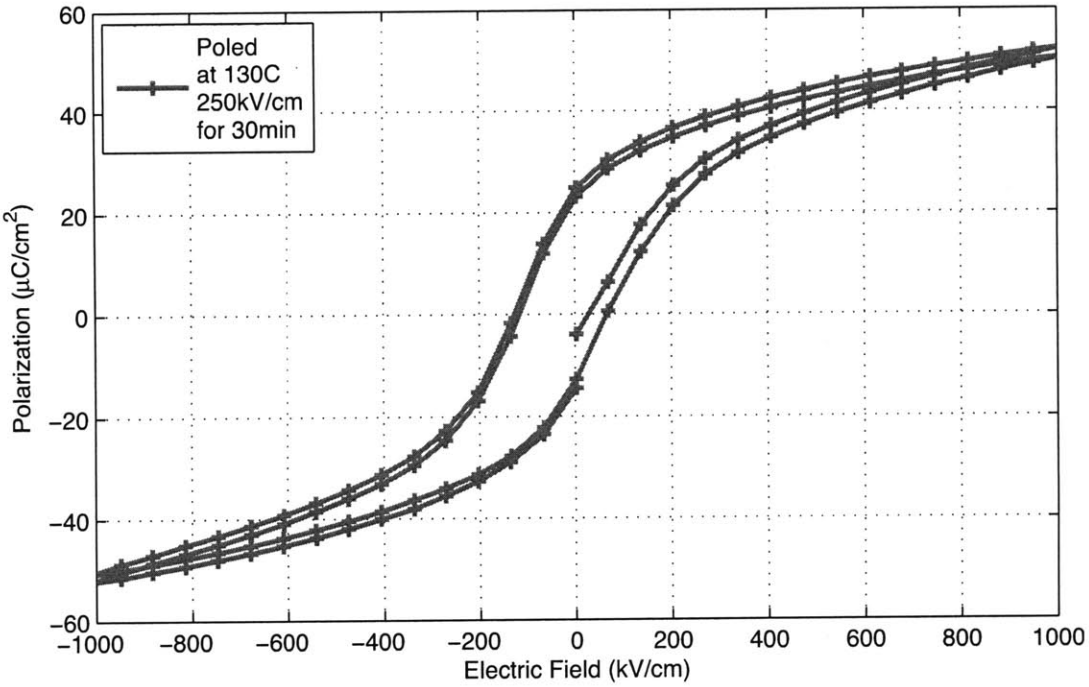

Figure 5-10: Measured P-V curve for the poled 3rd generation energy harvester.

P-V measurements are done using RT-66A standardized ferroelectric test system and its high voltage interface module by RADIANT. The P-V curve associated with the pie-shaped energy harvester is shown in Figure 5-9. This device has been poled at room temperature using a strong electric field ($300kV/cm$) prior the test. Figure 5-10 depicts the P-V curve measured from a poled 3rd generation device using the following settings:

Equipment	Radiant RT-66A w High-Voltage Interface
Profile	Double Bipolar
Amplifier	Internal
Preset Delay	100 ms
Hysteresis Period	6 ms

The measured remnant polarization, saturation polarization, and the coercive field of the device can be estimated as $2P_r$=$36\mu C/cm^2$, $2P_s$=$102\mu C/cm^2$, and $2E_c$=$200kV/cm$, respectively.

5.5 Poling

Since the centers of charge are functions of position only, the potential generated is directly proportional to the applied strain and vice versa, and is directionally dependent such that an opposite stress applied to the bulk results in an equal but opposite electric field. The dipoles are not randomly oriented throughout the tetragonal PZT materials. Neighboring dipoles align with each other to form regions of local alignment known as Weiss domains. Each Weiss domain has a net polarization. On the other hand, different Weiss domains are aligned in random directions; hence no overall polarization or piezoelectricity is exhibited by the material.

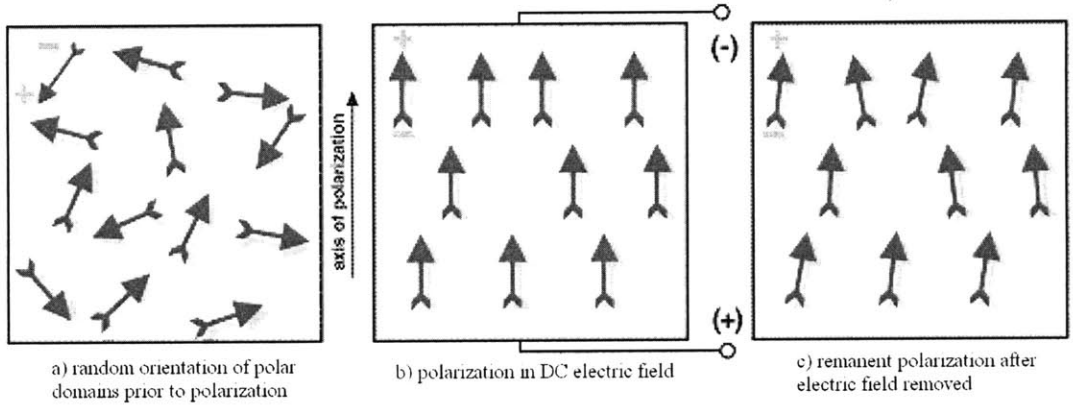

Figure 5-11: polarizing (poling) a piezoelectric ceramic [7]

The ceramic materials become piezoelectric through a poling process at a temperature below Curie point. When the material is placed in an electric field, domains that are aligned to the direction of the field will grow at the expense of other domains. When the field is removed, the dipoles remain locked, giving the ceramic material a permanent deformation (Figure 5-11).

Accordingly, the active layer of the fabricated devices should be poled to align the Weiss domains and increase the piezoelectric effect. In case of d_{31} devices, the PZT crystals grow in the direction of electric field (across the top and bottom electrode) naturally. Furthermore, the distance between electrodes are defined by the PZT thickness (less than a micron) and the PZT laer can be easily poled at room temperature. Conversely, d_{33} mode devices with top interdigitated electrodes are

much more difficult to poled. Weiss domains should be aligned and fixed between the interdigitated electrodes. The gap between electrodes are much larger than the d_{31} mode and much higher voltage is required for poling.

Room temperature poling is not adequate in this case and the device should be poled at elevated temperatures (higher than 100°C). The alignment of Weiss domains and the resulting piezoelectric properties is considerably improved at high temperature. In addition, the electric field should be strong enough to achieve a desirable poling. The poling voltage should be carefully chosen so that the electric field doesn't exceed the breakdown field of thin film PZT, especially at elevated temperature. Packaged pie-shaped were heated to 100°C and poled at 180kV/cm for 30 minutes using the setup shown in Figure 5-12. The electric field is controlled by the output signal from RT-66A system which is amplified by the high-voltage amplifier. The device is covered by a glass container which is heated by a hotplate. Temperature is simply monitored by a mechanical thermometer.

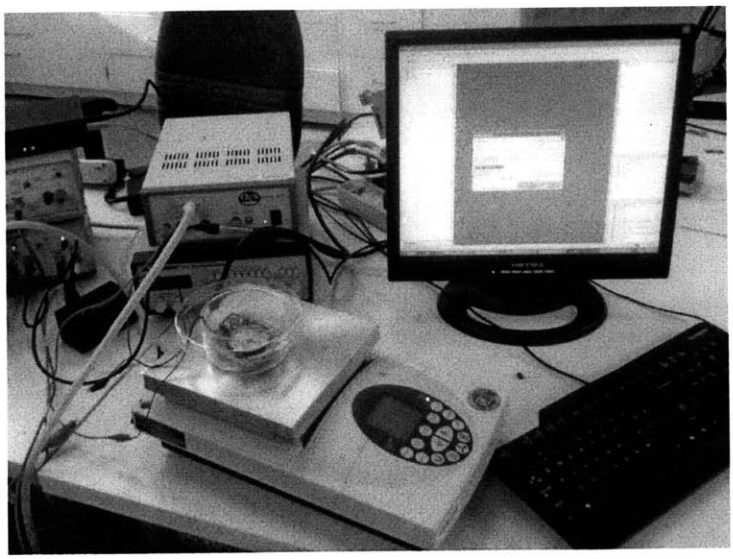

Figure 5-12: First poling setup

As will be explained in Section 5.8, the charge generated by the pie-shaped harvester was very small. The poling condition was suspected as the main reason for the poor performance of the device. Accordingly, the gap between interdigitated electrodes, w_g, was decreased from $5\mu m$ to $4\mu m$ in the 3rd generation device. In addition,

a new setup for poling the device was developed which is shown in Figure 5-13. To reach a more uniform and controlled temperature, a temperature sensor (thermistor) was embedded in a metallic container. The bottom surface of the container was covered with a high-temperature fiberglass insulating sheet. High-temperature resistant cables were used to provide the electric field for poling and also sensing the temperature (connected to the thermistor). The container is capped and heated by a hotplate and can be easily cooled down by a cold slab of metal.

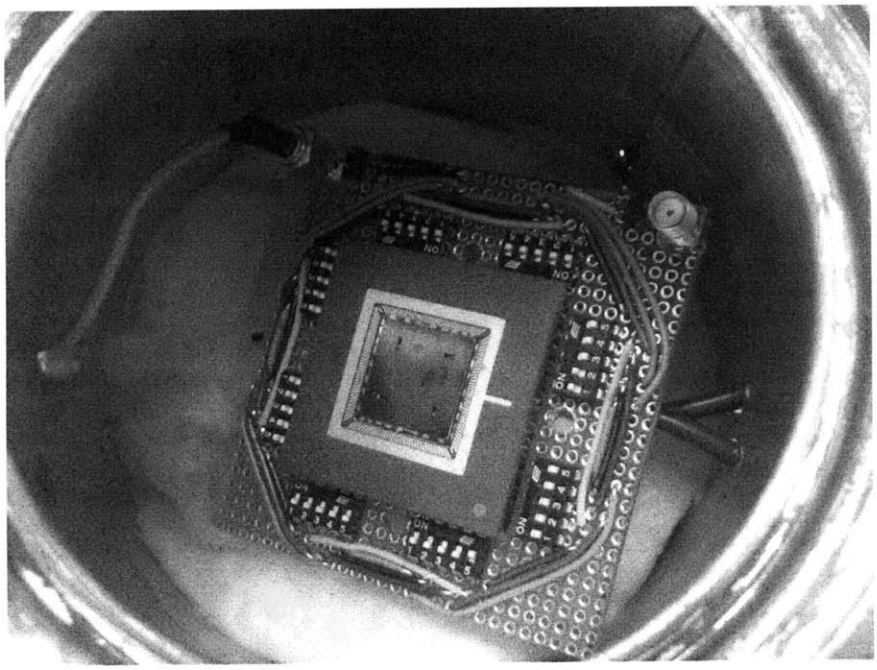

Figure 5-13: Second poling setup: the packaged device mounted on the testing-board is heated by convection at a well-controlled temperature condition.

The poling conditions including the temperature, electric field and the poling time were tested and investigated extensively. Increasing all of these parameters would improve the poling condition. Nevertheless, the risk of the breakdown is also increased. Figure 5-14 depicts a device in which the dielectric layer has been broken down and a crack has been propagated due to an improper poling. Consequently, a safe, repeatable and optimal poling condition has been sought.

The poling procedure has been modified heuristically to avoid the breakdown. At breakdown, excessive electric current passes through the dielectric which can heat

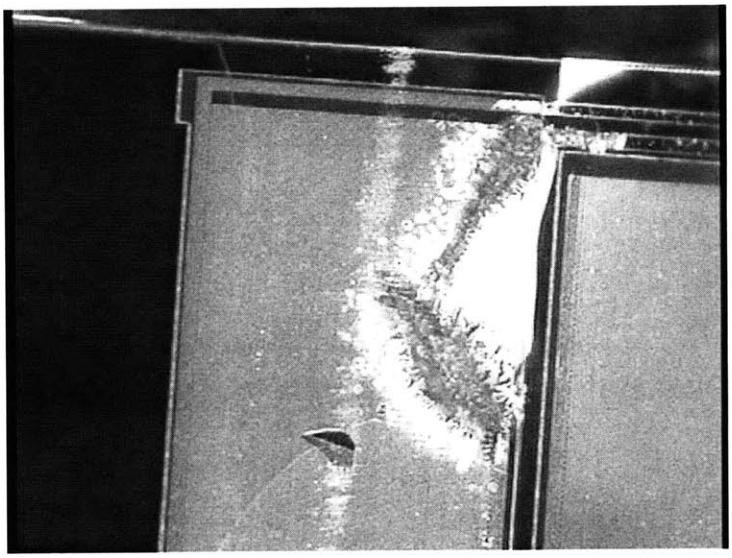

Figure 5-14: Excessive heat and electric field can result in the dielectric breakdown. The dielectric layer has been destroyed and a crack has been propagated from the breakdown region.

it up more and increases the leakage even more. To avoid this destructing cycle, the electric current should be monitored and limited throughout the poling process. During various poling experiments, a large variation in the electric current is observed as a function of time and temperature. At the early stage of poling, a very high current passes through the piezoelectric material which poles most of the domains. Afterward, the current will be stabilized at a much lower densities. At elevated temperature, the leakage current density may go up again. Aligning the rest of the un-aligned domains, requires a long poling at a high electric field.

A limiting resistor (few MegaOhms) was added in series to the input voltage. In normal condition, the current in the circuit is small and the voltage drop across the limiting resistor is negligible. Nevertheless, any large current results in a considerable voltage drop across the limiting resistance which pushes the electric field down in response. Therefore, the limiting resistance provides a negative feedback which keeps the current controlled and limited. Consequently, the electric field during the poling process is adaptively controlled to avoid the dielectric breakdown. This procedure provides a very strong and hence safe poling.

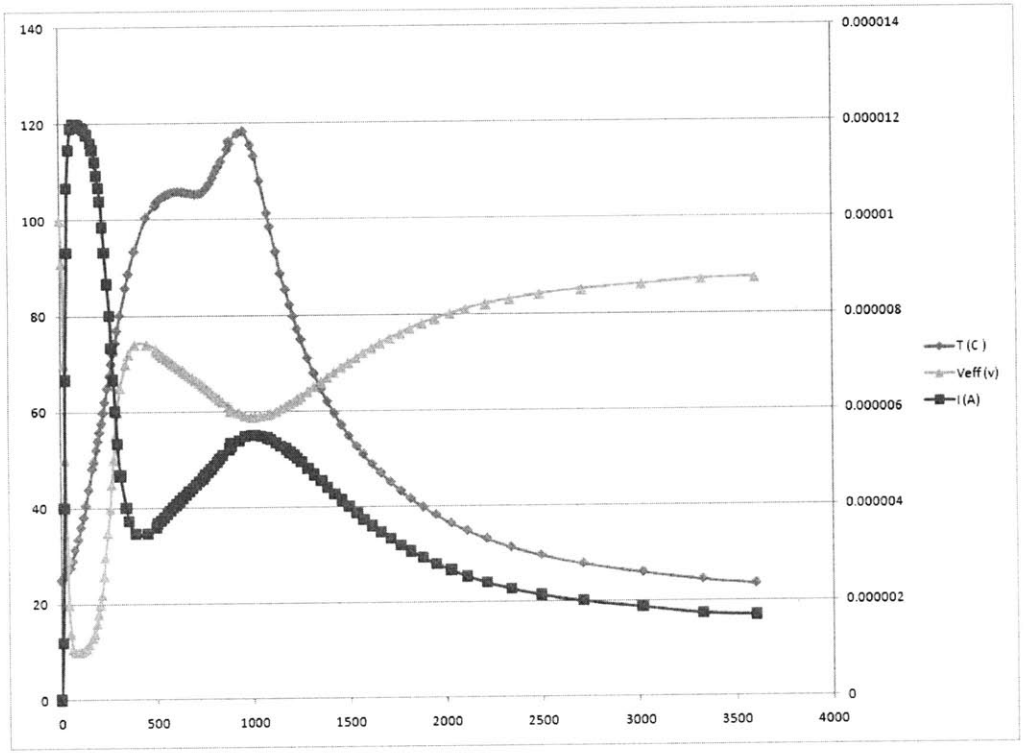

Figure 5-15: New poling process avoids the breakdown using a limiting resistor. The graph shows the effective poling voltage, current and temperature as a function of poling time.

5.6 Electromechanical Testing Setup

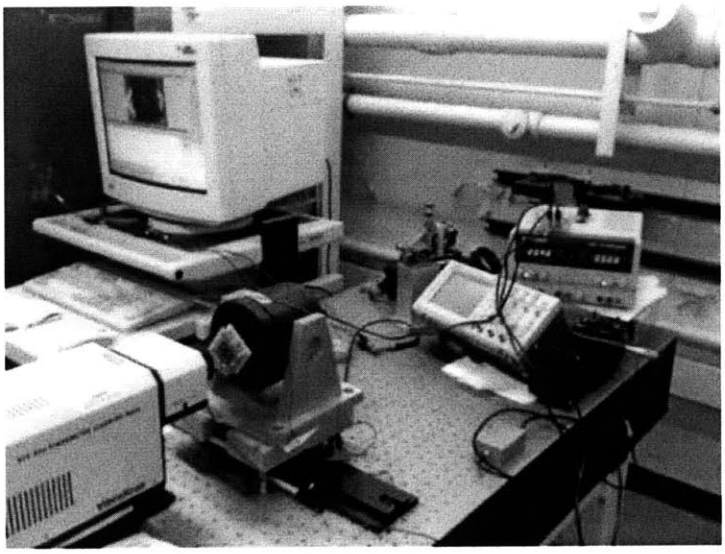

Figure 5-16: Electromechanical test setup: laser vibrometer measure the velocity of the proof mass and the base of the device excited by electromagnetic shaker. The output electrical charge is measured by the charge amplifier.

Electromechanical testing is performed on the packaged pie-shaped device at the Gas Turbine Laboratory using the setup shown in Figure 5-16. Device is excited by a B&K electromagnetic shaker type 4809 which is controlled by Prema ARB 1000 signal generator. The signal is pre-amplified by a Crown DC-300A Series II power amplifier. Motion of the central proof mass and the base is measured remotely by Polytec PSV-300H Doppler-effect laser vibrometer (Figure 5-17).

A laser Doppler vibrometer is an instrument which is used to perform non-contact vibration measurements of reflective surfaces. The vibration amplitude and frequency are extracted from the Doppler shift of the laser beam frequency due to the motion of the surface [128]. The PSV-300H scanning laser vibrometer is a versatile measurement system shown in Figure 5-18. The minimum displacement that the system can measure can be as small as sub-nanometer motion. The position of the laser beam can be controlled by the computer interface at an accuracy of approximately $\pm 10 \mu m$. This accuracy makes it a power system for testing MEMS-scale structure. In our case, both pie-shaped harvester and the 3rd gen device have meso-scale proof

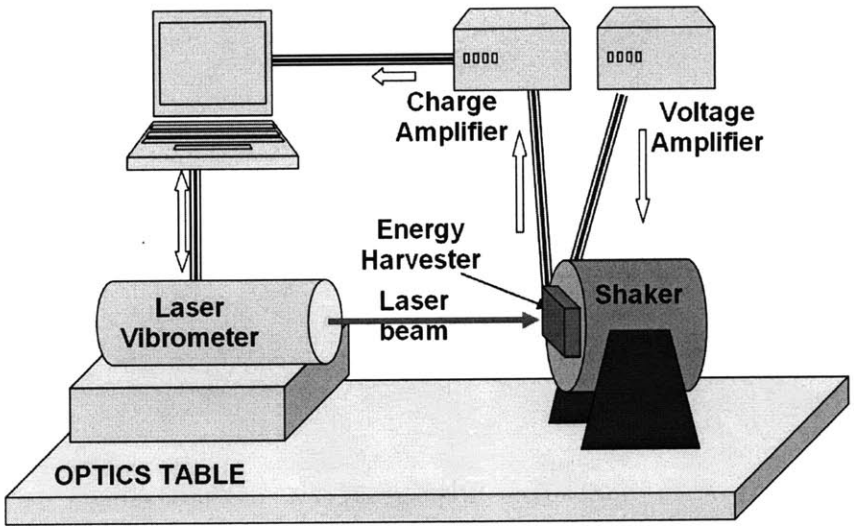

Figure 5-17: Schematic diagram of electromechanical test setup.

masses which can be easily targeted by the laser beam. In addition, the mode shape of vibration can also be measured in the multi-point mode of measurement.

3rd generation devices were tested at Digital Integrated Circuits and Systems Lab. The testing board is mounted on and excited by a ET-126B-1 electrodynamic shaker by Labworks Inc. The input signal is controlled by a signal generator (AFG3102 by Tektronix) or by the computer through a data aquisition (DAQ) board. The input signal is amplified by a power amplifier (PA-138 Labworks Inc.) and fed into the shaker. The generated voltage is measured by an ultra-fast oscilloscope (TDS5054B Tektronix) and also the computer through the DAQ board. The excitation acceleration is monitored through an accelerometer (MSP1001-ND) which is mounted on the shaker. All the input and output signals are processed through a National Instrument PCI data acquisition card (PCI-6229). NI PCI-6229 is a low-cost multifunction DAQ with four 16-bit analog outputs, 32 analog inputs (250kS/s), and 48 digital I/O. NI BNC-2110 is a shielded connector block with signal-labeled BNC connectors that is used as the interface to the PCI-6229 card.

The testing board has been especially designed for this setup. The PCB is connected and fixed to the shaker head by 5 screws to eliminate unwanted vibrations. Each packaged device can be easily mounted on the testing board and go through

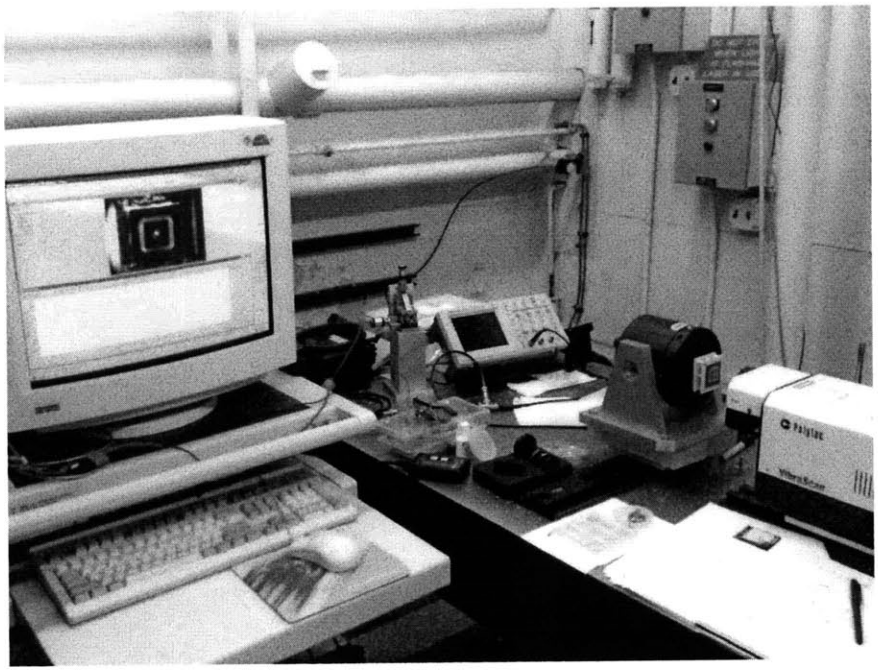

Figure 5-18: The position of laser can be controlled by the software. The velocity of the base and also the proof mass can be measured using multi-point measurement mode.

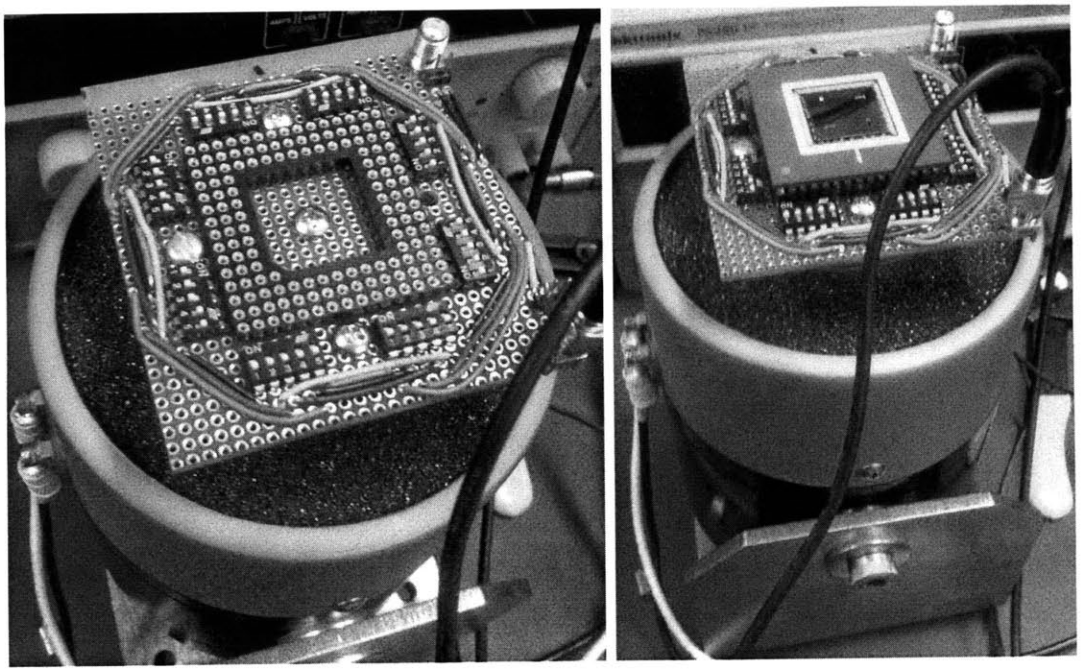

Figure 5-19: The testing board in connected to the shaker by 5 screws to improve the rigidity of the structure during vibration testing (left). Packaged devices can be easily mounted on the socket for electromechanical testings (right).

electromechanical testings as shown in Figure 5-19.

5.7 Vibration Testing Results

In both configurations, the base of each device is excited by the shaker at a constant input voltage. The input signal can be a pure sinusoid at a fixed frequency or a sweeping signal in which the frequency is changing as a function of time. The initial results from the first tested devices did not match our initial theoretical models. As shown in Figure 5-20, the structure resonated with a sharp peak at a very high frequency (about 2.7kHz) like a linear system. However, the mechanical model estimated a nonlinear wide-bandwidth resonance at much lower frequency ranges (about 100Hz). Such a high resonant frequency suggests a very stiff beam. To investigate the stiffness of the beam, a nano-indentation test was carried on the samples.

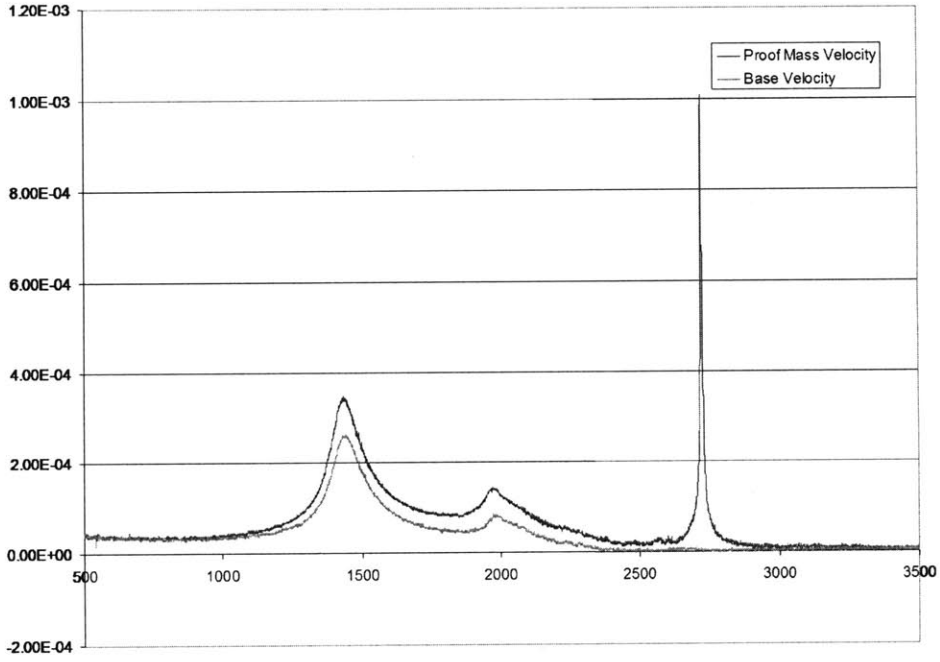

Figure 5-20: The initial testing shows a very high frequency resonance (2.7kHz).

Nano-Indentation

Sample devices with different length and width were testing using Hysitron TriboIndenter Nanoindenter at Materials Science and Engineering (DMSE). This nanoindenter features in situ imaging and AFM imaging of indentations, for a load range of $10\mu Ns$ to $10mNs$ and a maximum displacement of 5 microns. The proof mass has been indented slowly up to $10mN$ which is the maximum allowable load. The displacement of the proof mass is measured and shown in Figure 5-21. The force is a linear function of displacement up to $2\mu m$ deflection. In addition, the beam is very stiff (about 5300N/m). This stiffness is much higher than the theoretical value estimated from Eq. 3.13 but matches the resonance frequency measured in Figure 5-20.

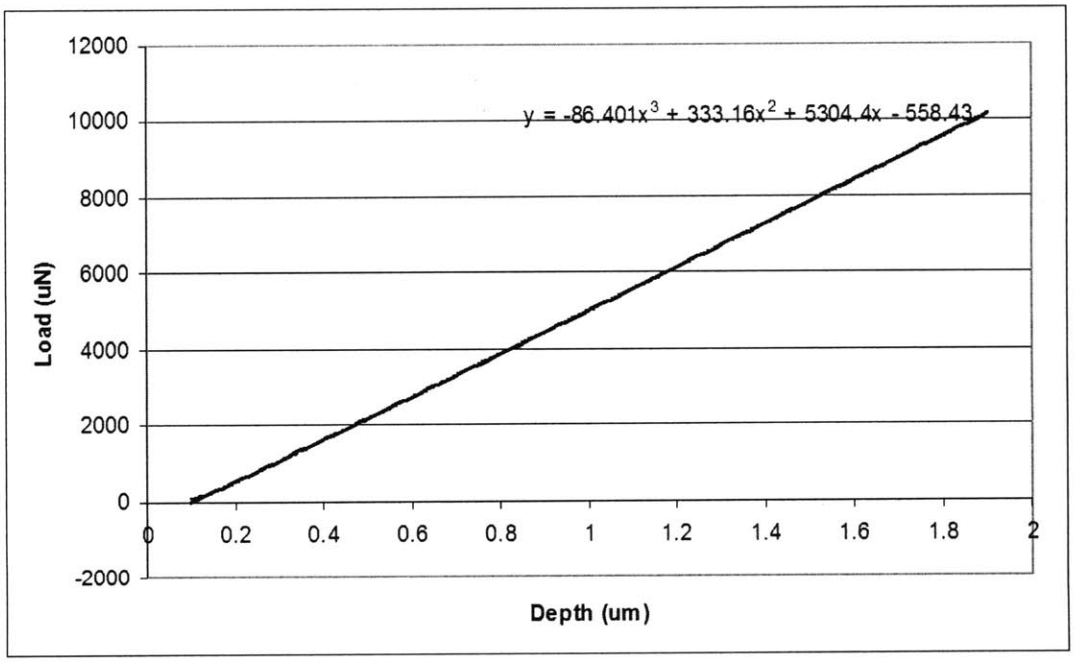

Figure 5-21: Nano-indentation result: the force is a linear function of displacement and the stiffness is estimated about 5300N/m.

Eq. 3.13 doesn't include the linear stiffness from the residual stress and consider the bending stiffness as the only linear term. However, this test showed us that the residual stress should be considered as the main source of stiffness. Therefore, the results were re-evaluated based on the Eq. 3.15. The average residual stress in the beam was estimated about 100MPa. Consequently, the linear stiffness is so high

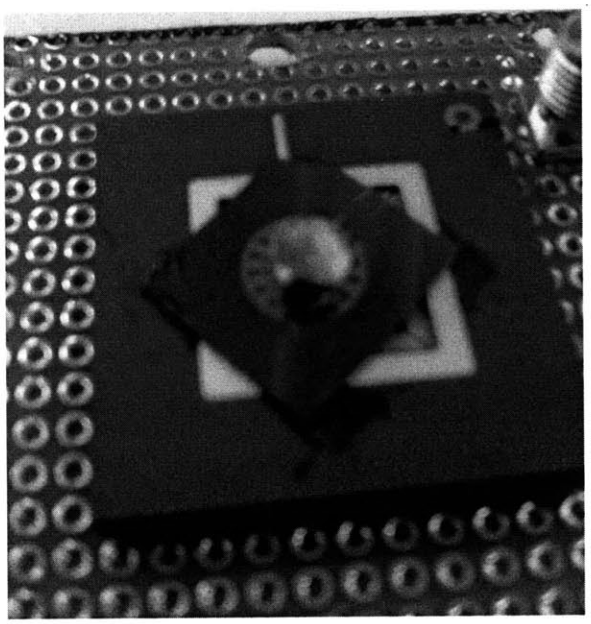

Figure 5-22: External heavy metallic mass attached to the proof mass of the pie-shaped harvester to decrease the resonance frequency.

that pushes the resonant frequency up to 2.7 kHz. At such a high frequency, the beam deflection is so small that cannot excite the nonlinearities. Consequently, the harvester acts like a linear resonator with a sharp resonance peak.

To bring the natural frequency down, either the residual stress should be decreased or a heavy mass can be attached to the original proof mass. Both options were tested successfully. A layer of compressive PECVD oxide/nitride was deposited on the beams. This procedure pushed the resonant frequency down to 1kHz and proved to be applicable in controlling the stress. The stress engineering explained in Section sec:stress-engineering has been implemented based on this observation. In addition, a very heavy metallic (100mg) mass was attached to the proof of the pie-shaped harvester as shown in Figure 5-22.

The pie-shaped harvester with the externally attached proof mass was retested. The base of the pie-shaped energy harvester was subjected to a sweeping vibration at 0.5g acceleration level that first ramps from 500Hz up to 1000Hz and subsequently ramp down back to 500Hz. The proof mass deflection is measured with respect to the base using the laser vibrometer in multi-point scanning mode. The maximum

sweeping time, which is limited by the software's spectrum analyzer, is used to ensure quasi-static measurement.

Using such a heavy mass pushed the resonance frequency down to about 720Hz. At this frequency range, the induced vibration is large enough to excite the nonlinearities. For a better comparison, the frequency response of the system is simulated based on the new model as shown in Figure 5-23a. The wide-bandwidth design (green) is totally different from that of a linear harvester with similar gain (blue). The nonlinear system provides much wider bandwidth (73Hz) compared to the linear system that suffers from a very narrow bandwidth (8.5Hz).

Actual frequency response (shown in Figure 5-23b) are measured in ramp-up (red graph) and ramp-down (blue) that obeys the theoretical prediction shown in Figure 5-23a. Ramping up the frequency slowly enforces the nonlinear stiffness acting as a negative-feedback that activates the high-energy stable region. It keeps the system pre-resonance and a large deflection is materialized in a wide range of frequency (720-855Hz). The amplitude jump-down suddenly at 855Hz to a very small amplitude. Ramping down the system activates the low-energy stable region of the nonlinear system that jumps up below 760Hz by activating the negative feedback. Total ramp up-down response shows a hysteresis-like graph which cannot be seen in linear systems.

5.8 Output Measurement

Pie-shaped energy harvester

The electric charge generated by the pie-shaped energy harvester was transformed into a voltage signal by a charge amplifier (VIPsensors 5000B). The output of the charge amplifier was measured by the DAQ board of the laser vibrometer system. The measured signal suffers from a large coupling due to the electromagnetic shaker. The frequency of the coupled signal is exactly equal to the excitation frequency. Consequently, the charge generated by the bending mode cannot be measured accurately. Nevertheless, The stretching strain is always tensile and reaches its maximum twice

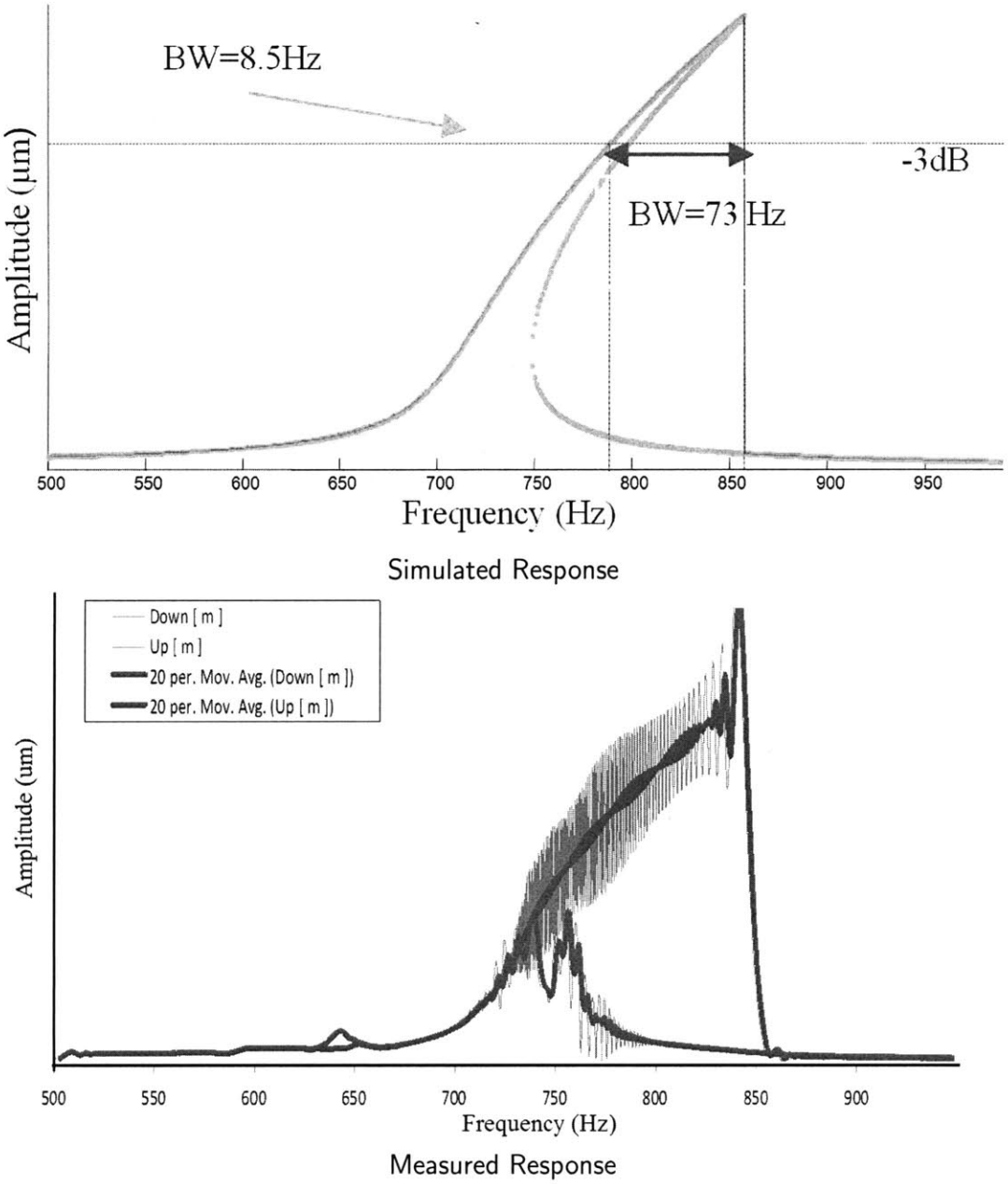

Figure 5-23: System's frequency response: *up* simulated response: nonlinear broadband system shows a wide bandwidth (73Hz) compared to the equivalent linear system that provides a very narrow bandwidth (8.5Hz) at the same gain and damping (Q=85), *down* experimental response verifies the simulation.

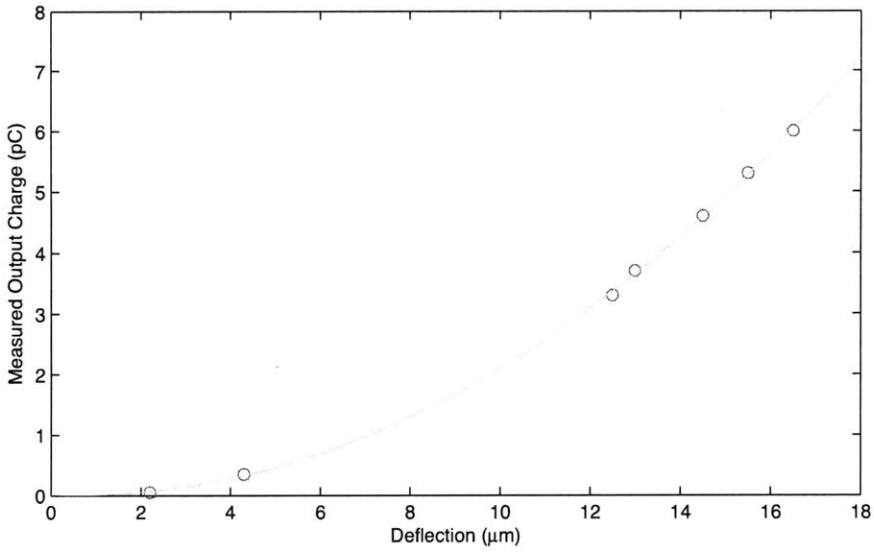

Figure 5-24: Measured output charge from the pie-shaped energy harvester.

per cycle; hence, the output signal associated with the stretching mode occurs at twice the frequency of excitation. Consequently, it would not be affected by the coupling that much.

This signal was measured for the pie-shaped device at several working points. The resulting electric charge has been plotted versus the deflection amplitude in Figure 5-24. Interestingly, the output charge is precisely proportional to the square of the deflection. This observation is in agreement with the Eq. 3.12. Nevertheless, the output charge is at least ten times smaller than the theoretical predictions. This weak signal can be a result of improper poling of the active layer.

3rd generation energy harvester

An early prototype of the 3rd generation energy harvester was poled using the procedure explained in Section 5.5. Afterward, the poled device was tested by the electromechanical test setup shown in Figure 5-19. To avoid the coupling and also noise signals, coaxial cables have been used for the measurement and the head of the shaker is grounded. The measured signal became extremely accurate using the mentioned tricks. The harvester was excited by the shaker and the frequency of vibration was slowly incremented from 260Hz up to 550Hz at which the jump down happened.

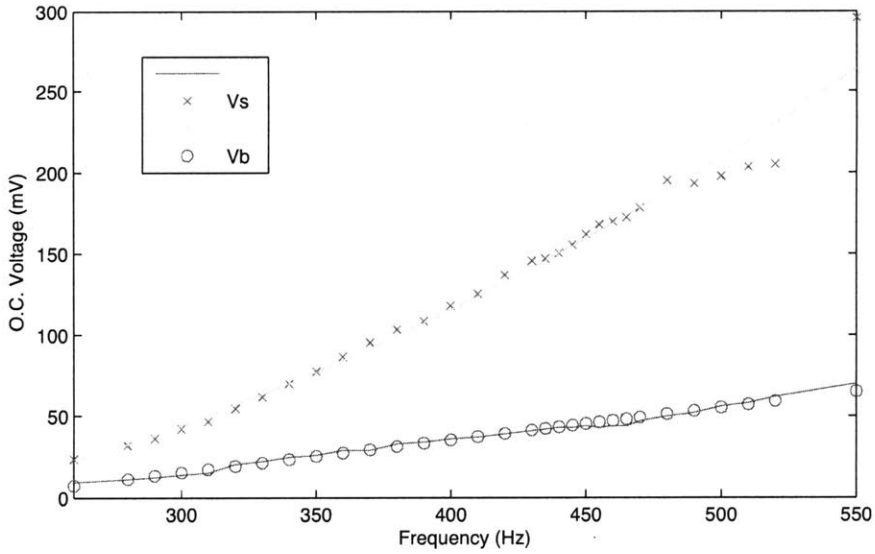

Figure 5-25: The open circuit output voltage from the 3rd generation device with rotated IDT electrodes.

The open-circuit output of the device was measured at various excitation frequencies. The voltage associated with the bending and stretching modes is extracted from the output signal using spectrum analyzer as shown in Figure 5-25. The trend of both signals agrees with the theoretical predictions shown in Figure 3-14. The bending and stretching terms increases linearly and quadratically, respectively. Although the output signal is much larger than the pie-shaped case, it is still smaller than the theoretical predictions due to a fabrication mistake.

The tested device was an early prototype in which the IDT electrodes have been misaligned 90° by mistake. The direction of electric field (across the IDT fingers) should be aligned to the direction of stretching strain (length of the beam) for the optimum performance of the device. Nevertheless, the IDT electrodes were placed perpendicular to the right direction in this prototype. As a result, the PZT layer generated charge in response to the lateral compression of the beam instead of the main stretching term. Consequently, the effectiveness of the harvester is decreased at least by a factor of poisson ratio. (0.18-0.25 for silicon oxide/nitride). This issue has been resolved in the second batch of fabrication and the IDT electrodes were reconfigured to the right direction.

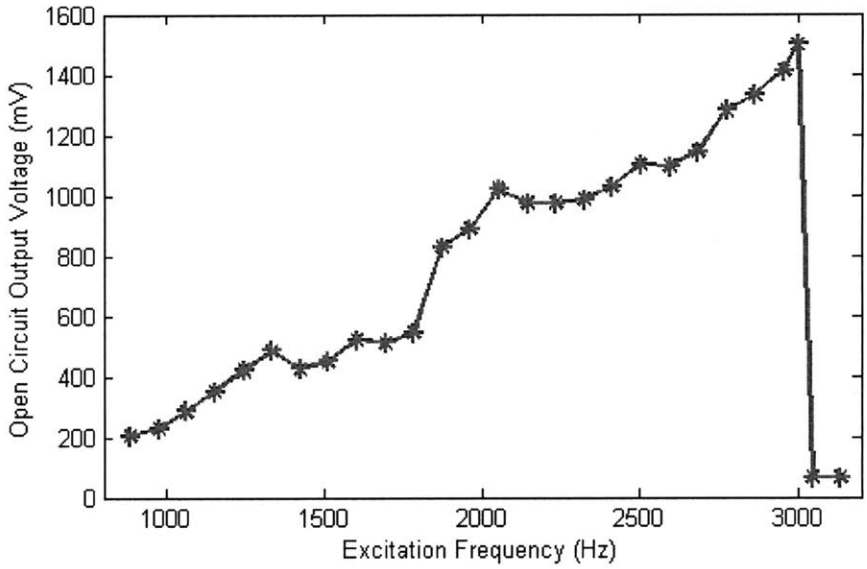

Figure 5-26: Measured open-circuit voltage generated by the harvester (peak-to-peak value in millivolts).

Reconfigured 3rd generation energy harvester

The mask associated with the IDT electrodes was redesigned and the orientation of the electrodes was corrected. A new batch of 3rd generation energy harvesting devices were fabricated based on the new mask. The fabrication yield rate has been improved to more than 60%. For electromechanical testings, a prototype was prepared by packaging a healthy device without an external proof mass. Therefore, each cell in the device could have been investigated independently. The prototype was mounted on the testing board shown in Figure 5-8. All four pairs of IDT electrodes associated with one cell were added in parallel using the DIP switches. The device is tested by the electromechanical testing setup shown in Figure 5-16. The base of the prototype was excited using a sweeping sine input that ramps up slowly from 800Hz up to 3200Hz in 30 seconds. The open circuit voltage across the electrodes were measured and monitored as the output signal using the digital oscilloscope. The frequency of the output signal is twice the oscillation frequency due to the tensile stretching strain.

Figure 5-26 shows the measured signal as a function of excitation frequency. The nonlinear behavior and wide-bandwidth resonance can be clearly seen. The output

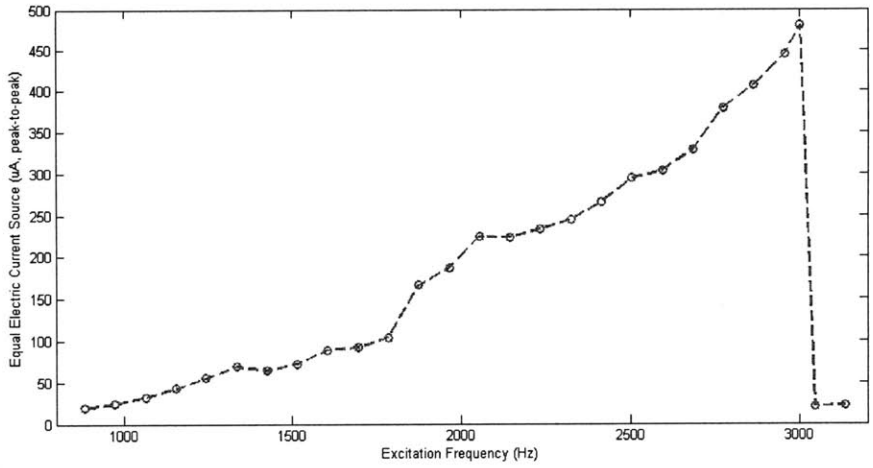

Figure 5-27: Calculated electric current source (peak-to-peak value in microampers).

voltage is slowly increasing from 200mV at 850Hz up to 1.5V at 3050Hz. At the jump-down frequency (about 3050Hz), the output volage abruptly drops to a very negligible value and the harvester goes off-resonance. The capacitance of the device was estimated from the measured P-V curve. The relative dielectric constant and the total capacitance for the whole device are 2000 and 8.5nF. Accordingly, the electric current source of the harvester can be estimated ($I_{source} = 2\omega_{ex}C_0V_{O.C.}$). The strong current source (up to $400\mu A$) implies a healthy device with high-quality piezoelectric response.

The piezoelectric coefficient and piezoelectric coupling factor for this device can be estimated as d_{33}=110pm/V and k_{33}=20%, respectively.

Reconfigured 3rd generation energy harvester with proof mass

To push the frequency range even lower, the reconfigured energy harvester was attached to an external proof mass and tested. The package device was poled using a similar procedure explained in Section 5.5. The poled device was tested using the setup shown in Figure 5-16. The velocity of the central proof mass and the output voltage were measured by the laser vibrometer data acquisition system. The device were excited using a sweeping sinusoid which ramps quickly 300Hz up to 2kHz. The sweeping interval was selected equal to the total FFT time so that each frequency

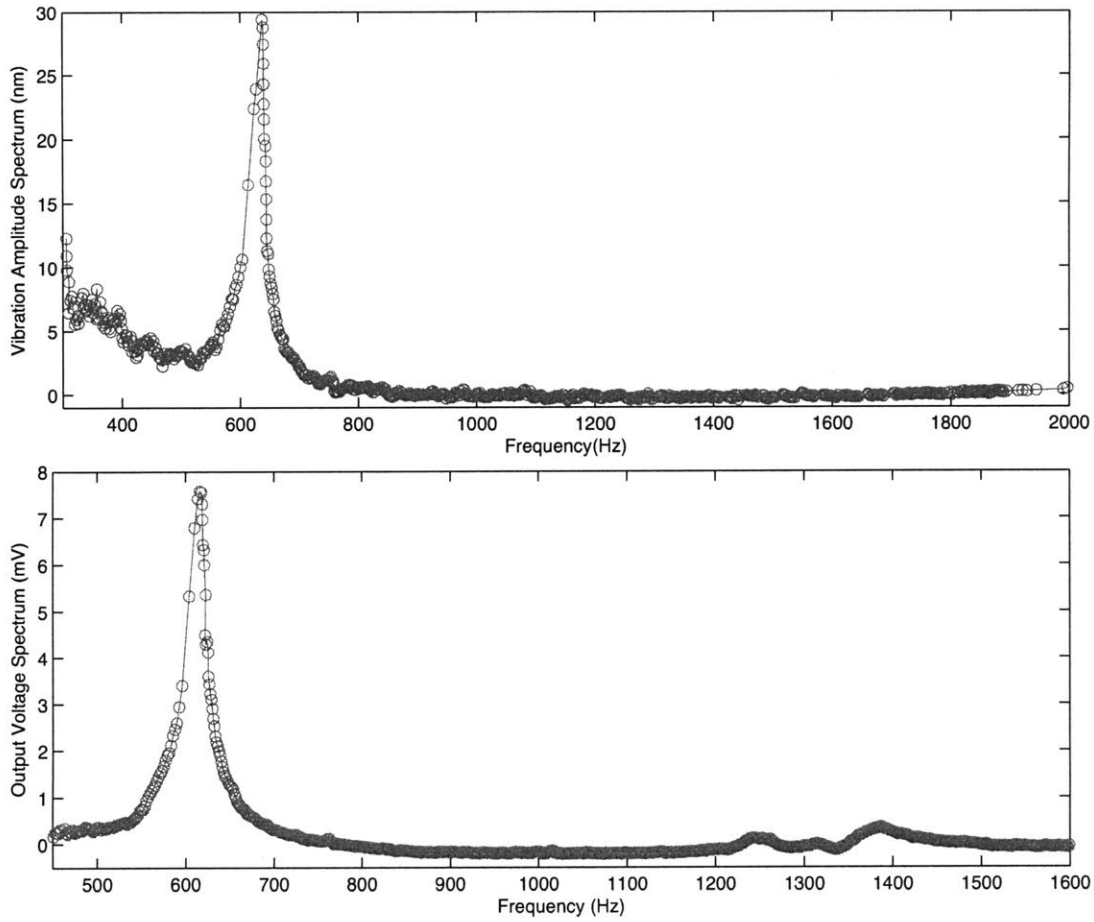

Figure 5-28: Measured displacement (top) and open-circuit voltage (bottom) spectrum generated by the harvester (low-g condition: shaker input of 0.05V).

spectrum covers exactly one test. To improve the accuracy, the frequency spectrum was averaged up to 5 times. The device was excited at low (0.05V), medium (0.4V), and high (1.0V) input voltage amplitude to the shaker. The spectrum of the proof mass motion and the output voltage is calculated by the system's internal FFT analyzer. The output voltage was subsequently scaled to its real values which were measured using the oscilloscope.

The frequency response of the system excited by a low amplitude vibration is shown in Figure 5-28. The excitation amplitude is so small that the system behaves like a linear system with a sharp peak at its resonance frequency (620Hz). The output voltage spectrum shows a strong peak at 620Hz due to the bending mode.

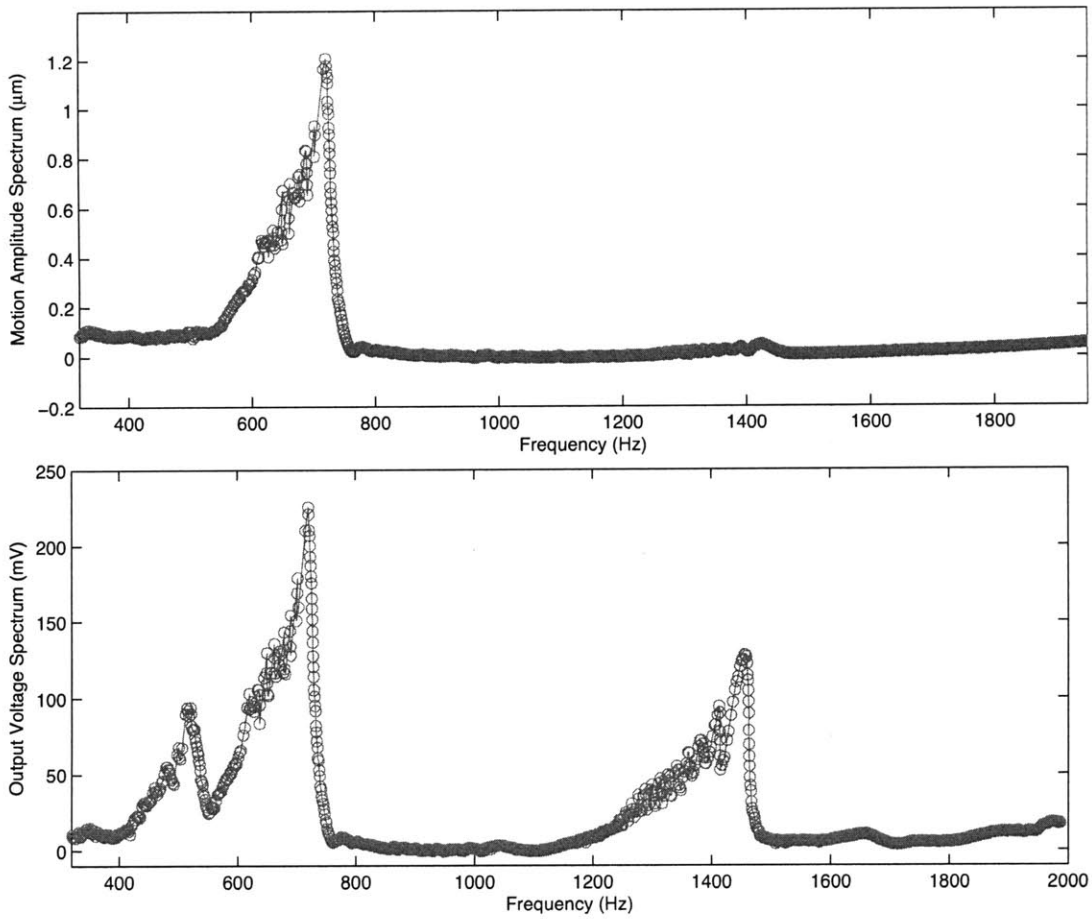

Figure 5-29: Measured displacement (top) and open-circuit voltage (bottom) spectrum generated by the harvester (mid-g condition: shaker input of 0.4V).

The stretching mode is still weak and a very tiny peak can be seen at 1240Hz.

By increasing the input vibration to the mid-range level, the nonlinear stiffness becomes active and a wide-range resonance can be easily seen as shown in Figure 5-29. The harvester starts to resonate at 560Hz and the amplitude of vibration increases smoothly afterward. Finally, the resonator jumps down at 740Hz and becomes quiet. In addition, a second component of voltage can be clearly seen in the output spectrum. This second component can be seen at twice the frequency of vibration due to the always-tensile stretching strain as explained before. Nevertheless, the linear bending component is still dominant.

Increasing the input voltage of the shaker to 1V fully activates the nonlinear mode

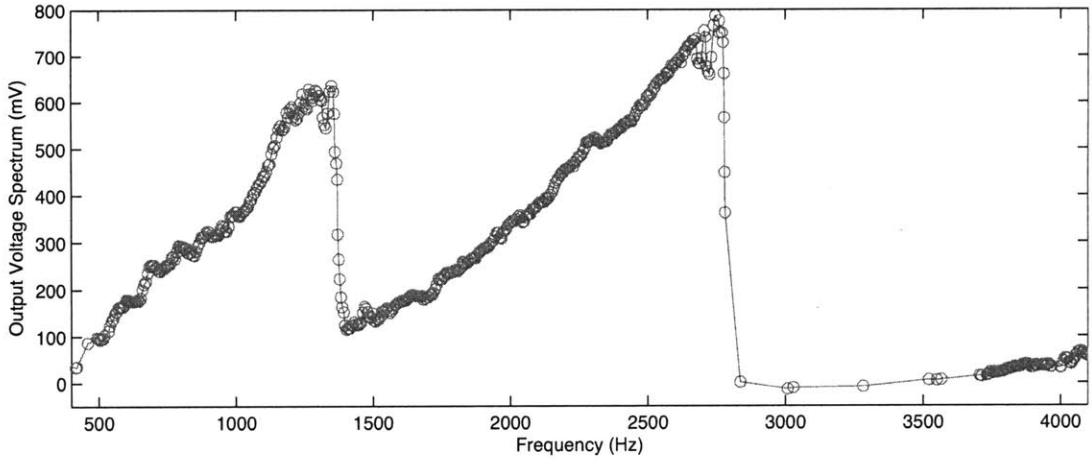

Figure 5-30: Measured open-circuit voltage spectrum generated by the harvester (high-g condition: shaker input of 1.0V).

as shown in Figure 5-30. The harvester resonates in a wide range of frequencies (from 500Hz up to 1400Hz). The output voltage is mainly defined by the stretching mode and a sinusoid voltage at twice the frequency of vibration can be measured from the device. The output voltage reaches 1.7V (peak-to-peak) at 1400Hz.

Chapter 6

Electronic circuits and interfaces

6.1 Electrical Interface

The UWB piezoelectric energy harvester presented in this work aims to maintain large strain in the piezoelectric layer at a wide range of frequency. This elastic energy is converted into electrical energy in the form of oscillating polarization across the piezoelectric layer. However, the main objective of the micro-scale energy harvesting is to exploit this energy and power ULP electronic circuits. The electronic devices generally requires a constant and stable DC power supply.

As shown in Figure 6-1, a classical interface rectifies the AC voltage generated across the piezoelectric element using rectifying diodes followed by a filtering capacitor. A more advanced interface may include an additional DC-to-DC converter to improve the matching and also generate the required voltage level [129]. However, the classic interface is extremely inefficient and delivers small amount of extractable energy at a low voltage level. The efficiency of the piezoelectric energy harvesting can be highly improved using smarter electric interfaces.

Guyomar et al. presented a new technique called synchronized switch harvesting on Inductor (SSHI) which can increase the electric power up to 900% [14]. This method is derived from the synchronized switch damping (SSD), which is a nonlinear technique previously developed to improve active damping efficiency [130]. Ammar and Basrour proposed an alternative an alternative called synchronized switch har-

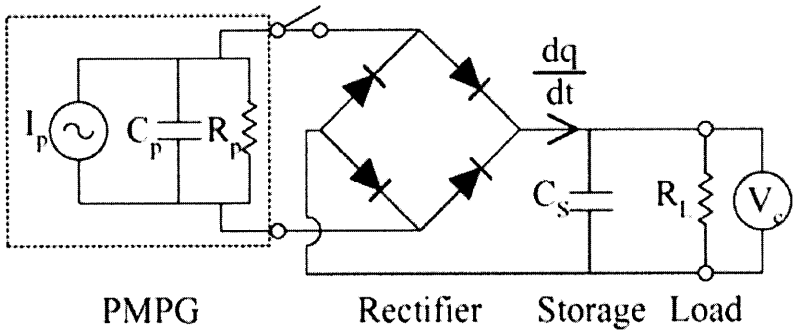

Figure 6-1: A classical piezoelectric energy harvesting interface implemented in the PMPG device. The AC signal generated by the piezoelectric layer is converted to a DC source using a bridge rectifier followed by a filtering capacitor [10].

vesting on capacitor (SSHC) which is basically the dual of the SSHI technique for electromagnetic harvesters [131]. Recently, Ramadass and Chandrakasan have developed a low-power interface based the SSHI technique which is implemented in a $0.35\mu m$ CMOS process [15]. The bias-flip rectifier is coupled to a switching DC-DC converter to improve the matching and tuning the output voltage. In this section, a brief review of these techniques and their compatibility with the UWB design is presented and discussed.

6.1.1 Electromechanical Model

A general form of the electromechanical dynamic equations is required to better understand the effect of electrical interface on the energy harvesting performance. The piezoelectric layer couples the mechanical domain to the electrical domain based on its constitutive equations. Eqs. 2.1 can be rearranged as

$$T = c.S - \epsilon^t.E \tag{6.1}$$

$$D = e.S + \epsilon_S.E \tag{6.2}$$

in which $e = d \times Y$ is the piezoelectric constant. Unlike a linear system, the strain term include both bending and stretching terms (Eqs. 3.12 and 3.11). Integrating

Eqs. 6.1 over the PZT volume, the effective total force and the current from the PZT layer can be estimated. Combining the results with the equation of motion, Eq. 3.23, the complete set of nonlinear electro-mechanical dynamic equations can be derived:

$$\begin{aligned} (k_B + k_{\sigma_0})\,\delta + k_s\delta^3 + c_M\delta + \alpha_E V + m_{pm}\ddot{\delta} &= -m_{pm}A_{ex}\sin\omega_{ex}t \qquad (6.3) \\ \alpha_B\dot{\delta} + \alpha_S\delta\dot{\delta} - C_0\dot{V} &= I \qquad (6.4) \end{aligned}$$

where V is voltage across the piezo element; I denotes the electric current;α_E is the electrical to mechanical force factor; α_B and α_S are mechanical to electrical force factors associate with bending and stretching terms and C_0 is the clamped capacitance. These parameters are a function of device geometry, PZT thickness and material properties. The $\alpha_E V$ term in the first equation shows the effect of electrical loading on the mechanical response of the system. This term has been previously represented as the electrical damping force, $c_E\delta$.

The second equation considers the electrical side of the piezoelectric energy harvester. The motion of the beam generates two sources of electric current via the piezoelectric effect. The bending strain acts as a current source which is proportional to the velocity of the proof mass. Stretching strain, however, acts as a current source that oscillates twice in each mechanical cycles (Figure 6-2).

The UWB piezoelectric energy harvesting is designed mainly based on exploiting the stretching strain. Therefore, the stretching-based current source is the dominant energy source. Nevertheless, the bending term becomes important for the start-up phase as will be explained in Section 6.2. The stretching-based current source can be estimated as a sinusoid signal:

$$I_S(t) = I_{S,max}\sin(2\omega_{ex}t) = A_{IDT}S_{S,max}e_{33}\omega_{ex}\sin(2\omega_{ex}t) \qquad (6.5)$$

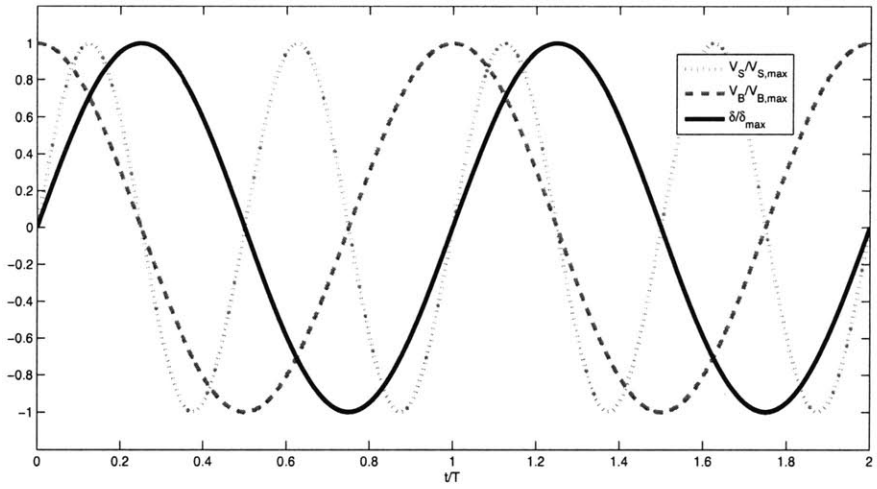

Figure 6-2: The bending strain acts as a current source which is in phase with the velocity of the proof mass. The stretching strain oscillates at twice the frequency of vibration.

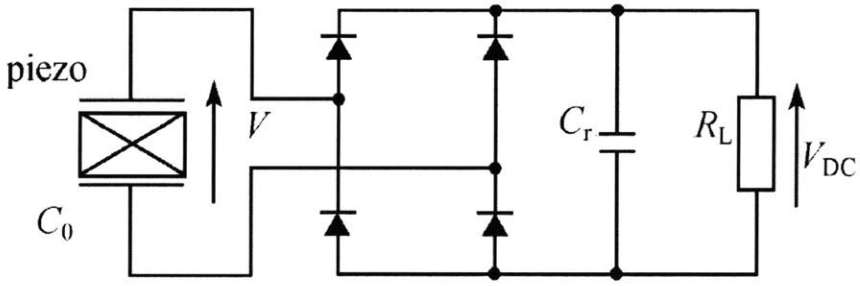

Figure 6-3: Classic DC interface [13].

6.1.2 Piezoelectric energy harvesting interfaces

Qiu et al have investigated four types of interfaces for piezoelectric energy harvesting and compared their efficiencies [13]. These interfaces are explained briefly here and their applicability to the nonlinear UWB energy harvester is investigated.

Classic interface with full-bridge rectifier

The classic interface is shown in Figure 6-3. It includes a full bridge rectifier followed by a filtering capacitor. The electric load is simply represented by a pure resistance, R. For simplicity, the rectifier is assumed to be ideal with no voltage drop. To get an stable output voltage with negligible ripples, a large capacitance C_r is used in general.

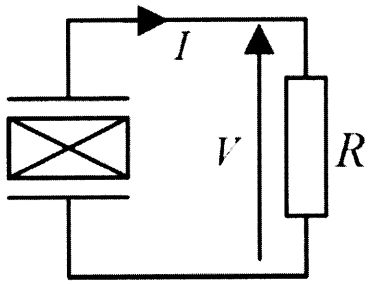

Figure 6-4: Classic AC interface [14].

V_{DC} can be assumed constant if the time constant RC_r is at least 20 times larger than the oscillating period. To better understand the interface, a simple AC classic device is investigated first. The output of energy harvesting is directly connected to a pure resistive load as shown in Figure 6-4.

The piezoelectric device acts like a current source, Eq. 6.5, driving a R-C shunting circuit. The voltage across the load, R_L, can be expressed in phasor domain:

$$\tilde{V_R} = \frac{R}{1 + 2jRC_0\omega_{ex}} I_{S,max} \tag{6.6}$$

The average power transferred to the load, P, optimum load, R_{opt} and the maximum extractable power, P_{max} can be obtained:

$$P = \frac{R}{1 + (2RC_0\omega_{ex})^2} I_{S,max}^2 \tag{6.7}$$

$$R_{opt} = \frac{1}{2C_0\omega_{ex}}, P_{max} = \frac{I_{S,max}^2}{8C_0\omega_{ex}} \tag{6.8}$$

To analyze the DC interface shown in Figure 6-3, the electric charge balance should be considered. The rectifier blocks the current from the piezoelectric element to the load as long as the absolute voltage of the piezo element, V, is lower than V_{DC}. During this blocked state, the charge is stored on C_0 and the voltage V increases as a result. When the absolute value of V exceeds the V_{DC}, the rectifier acts like a perfect connection. Subsequently, the current is divided between the load and also the capacitor C_r. Capacitances preserve the charge in each cycle and it can be assumed that all the charge generated by the piezo element has flown through the load R. As

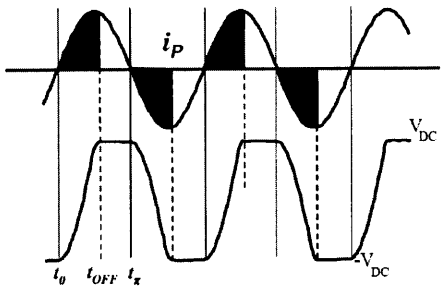

Figure 6-5: Simulated current and voltage waveform for a DC classic interface [15].

a result, the steady-state output voltage, V_{DC}, electric power, optimum load and the maximum extractable power can be found:

$$V_{DC} = \frac{2R}{4RC_0\omega_{ex} + \pi} I_{S,max} \tag{6.9}$$

$$P = \frac{V_{DC}^2}{R} = \frac{4R}{(4RC_0\omega_{ex} + \pi)^2} I_{S,max}^2 \tag{6.10}$$

$$R_{opt} = \frac{\pi}{4C_0\omega_{ex}}, P_{max} = \frac{I_{S,max}^2}{4\pi C_0\omega_{ex}} \tag{6.11}$$

Voltage doubler interface

The voltage doubler interface, shown in Figure 6-6, can generate a higher output voltage compared to the full-bridge rectifier (Figure 6-7). This interface is more practical for piezoelectric energy harvesting in d_{31} mode which generates a low output voltage. In addition, the diodes are not ideal in reality and cause a voltage drop of 0.2V-0.7V. Consequently, one diode voltage drop in the voltage doubler interface is more acceptable than two diode voltage drops related to the full-bridge rectifier. Accordingly, this scheme has been preferred in some reported piezoelectric energy harvesters [65]. The output voltage and the harvested power can be derived theoretically:

$$V_{DC} = \frac{R}{RC_0\omega_{ex} + \pi\left(1 + \frac{C_0}{C_1}\right)} I_{S,max} \tag{6.12}$$

$$P = \frac{R}{\left[RC_0\omega_{ex} + \pi\left(1 + \frac{C_0}{C_1}\right)\right]^2} I_{S,max}^2 \tag{6.13}$$

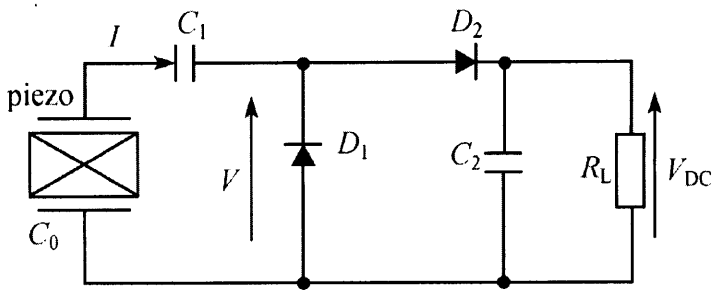

Figure 6-6: Voltage doubler interface [13].

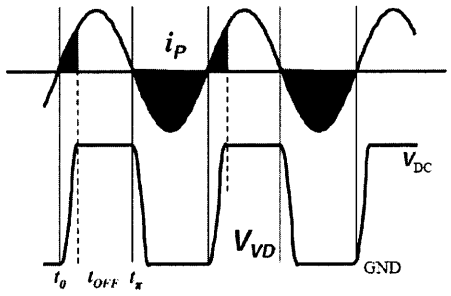

Figure 6-7: Simulated current and voltage waveform for a voltage doubler interface [15].

Synchronized switching harvesting on the inductor (SSHI)

The main limitation associated with the classic interface is the internal capacitance of the piezoelectric element. The interface acts as a R-C shunted load in which the current source is divided between the capacitance and the resistive load. At optimum case, the impedance of the resistive load should be matched to the impedance of the capacitor. Consequently, the maximum extractable power is defined by the internal capacitance of the system. Therefore, if the internal capacitance of the harvester could be canceled somehow, the extractable power would be only defined by the resistive load.

Adding a shunting inductor, L, in parallel to the electric load can result in a RLC-shunting load as shown in Figure 6-8. The internal capacitance can be canceled theoretically by matching the natural frequency of the RLC circuit, $1/\sqrt{LC}$, to the frequency of the current source. However, in practice it requires an extremely large inductor (up to hundreds of Henrys) for a typical piezoelectric energy harvester.

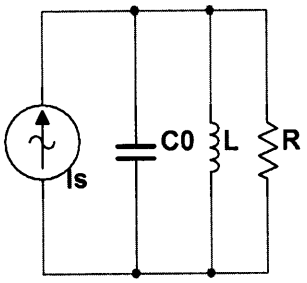

Figure 6-8: Adding an inductor to the classic AC interface can improve the efficiency.

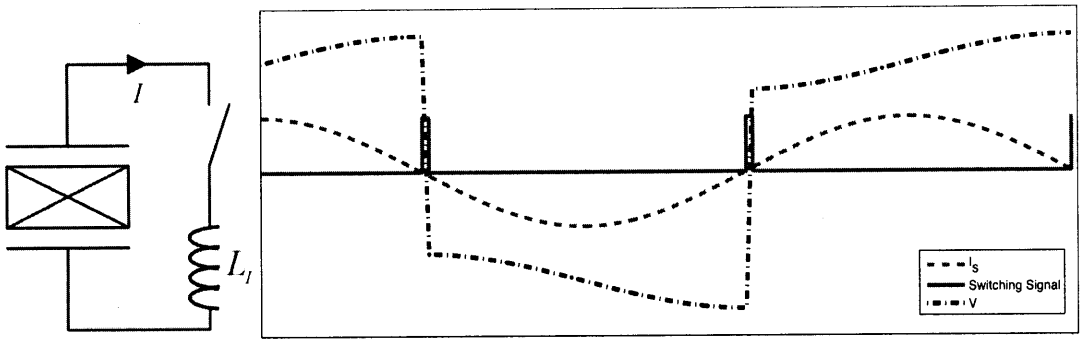

Figure 6-9: A switching inductor circuit and its corresponding voltage, current and switching waveforms.

Guyomar et al. have proposed a nonlinear technique based on switching a small shunting inductor instead of using a large inductor [14]. Figure 6-9 shows the basic idea of SSHI method using a simple circuit. The piezoelectric element is shunted with an inductor in series with a switch. The switch is almost always open except when the current becomes zero. At this point, the switch is closed and the charge stored on the capacitor flows through the inductor till the voltage is reversed across the device. During the switching period, the circuit acts like a LC load that has a time period of $2\pi\sqrt{L_1 C_0}$. Therefore, the switching time is defined by half of this period, $t_s = \pi\sqrt{L_1 C_0}$, which takes to reverse the voltage. Subsequently, the switch is opened again and the current source continues to increase the absolute voltage across the capacitor. Consequently, this technique can generate a large voltage across the piezoelectric element and also on the load.

However, the inductor is not ideal and has some internal resistance. Accordingly,a quality factor, Q_I can be defined for the inversion during the switching. The relation-

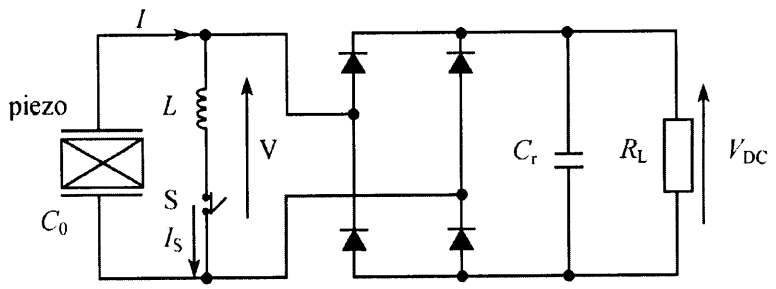

Figure 6-10: Synchronized switch harvesting on the inductor (SSHI) interface [13].

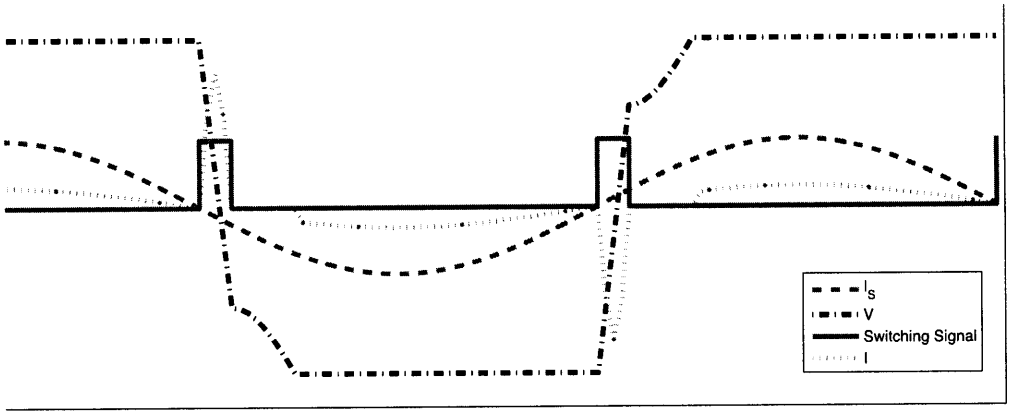

Figure 6-11: Simulated current and voltage waveforms for a voltage doubler interface.

ship between the voltage before, V_1, and after, V_2, the switching, V_2, can be expressed as a function of the quality factor:

$$V_2 = -V_1 e^{-\pi/2Q_I} \tag{6.14}$$

The waveform generated by this circuit is shown schematically in Figure 6-9. The switching inductor increases the efficiency of the energy harvesting in two ways: boosting the voltage level and aligning the voltage and current always in phase. A complete SSHI interface including a full bridge rectifier, filtering capacitance and the resistive load is shown in Figure 6-10. The electric current and voltage waveforms associated with this interface is shown schematically in Figure 6-11.

The steady state output DC voltage, electric power, optimum load and maximum extractable power can be derived by considering the conservation of electric charge as explained in [14]:

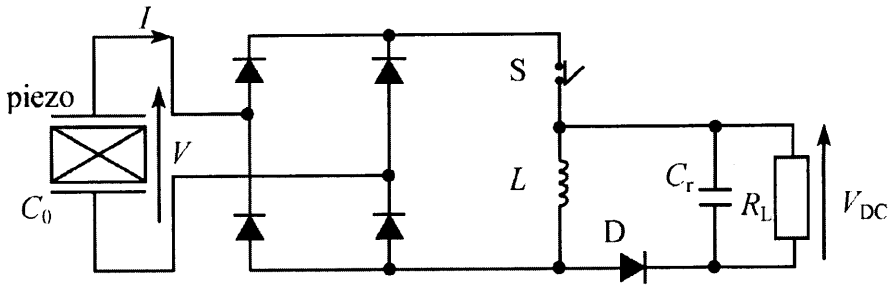

Figure 6-12: synchronized charge extraction (SCE) interface [13].

$$V_{DC} = \frac{R}{RC_0\left(1 - e^{\frac{-\pi}{2Q_I}}\right)\omega_{ex} + \frac{\pi}{2}} I_{S,max} \tag{6.15}$$

$$P = \frac{R}{\left[RC_0\left(1 - e^{\frac{-\pi}{2Q_I}}\right)\omega_{ex} + \frac{\pi}{2}\right]^2} I_{S,max}^2 \tag{6.16}$$

$$R_{opt} = \frac{\pi}{2C_0\left(1 - e^{\frac{-\pi}{2Q_I}}\right)\omega_{ex}}, P_{max} = \frac{I_{S,max}^2}{2\pi C_0\left(1 - e^{\frac{-\pi}{2Q_I}}\right)\omega_{ex}} \tag{6.17}$$

In case of high quality factor inductor, $Q_I \gg \frac{\pi}{2}$, the maximum extractable power can be approximated by Eq. 6.18. This means that for UWB energy harvester, the maximum extractable electric power is proportional to the inversion quality factor. By implementing very high Q_I, it is possible to extract the available power calculated in Section 3.5.5.

$$P_{max} = \frac{Q_I I_{S,max}^2}{4\pi^2 C_0 \omega_{ex}} \tag{6.18}$$

Recently, similar electrical interfaces have been reported based on switching technique. These methods includes synchronized charge extraction (SCE) [13] (shown in figure 6-12, synchronized switching harvesting on capacitor (SSHC) [131], and switch-only rectifier circuit [15]. However, SSHI technique seems to provide the best performance at such a simplicity. Yogesh and Chandrakasan have coupled the SSHI interface with a DC-DC buck/boost converter in a single chip to actively control the electric load [15]. The architecture of the bias-flip rectifier system which is fabricated

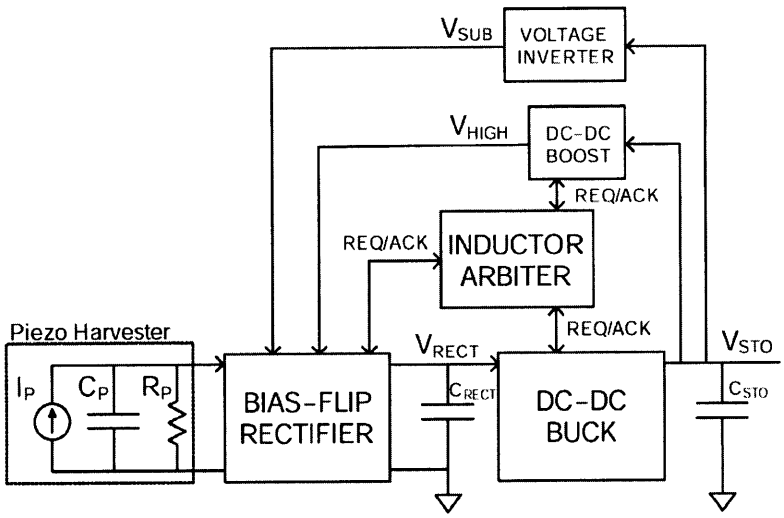

Figure 6-13: synchronized charge extraction (SCE) interface [13].

as a ULP chip as shown in Figure 6-13. A similar system should be modified based on the UWB energy harvester properties. The interface should smartly tune the effective loading based on the maximum electrical damping explained in section 3.5.5.

6.1.3 Power Estimation

In electrical domain, a piezoelectric energy harvester can be fully defined by its associated current source model and its internal capacitance and resistance. The final prototype developed in Section 5.8 can be similarly defined by its internal resistance ($3.5M\Omega$), internal capacitance (8.5nF), and the current source shown in Figure 5-27. The extractable harvestable power is a function of the electric interface as it was explained. The output power and matched loading conditions can be calculated based on the equation given in this chapter. This equations are valid as long as the generated power does not exceed the maximum theoretical value of the electrical damping explained in section 3.5.6. Otherwise, the oscillator will jump down and negligible electric power would be available afterward. Consequently, the UWB energy harvesting is achievable by employing an efficient interface such as SSHI and carefully tuning the maximum load to avoid the jump-down.

The matched load and the maximum extractable electric power based on the

less efficient classic AC interface can be estimated using Eq. 6.8 for any harvester. Figure 6-14 shows these value evaluated in case of the 3rd-generation piezoelectric energy harvester. The extractable electric power can be as high as $45\mu W$ at 3050Hz. Considering the total volume of the piezoelectric layer (2.16e-5), the power generation density is evaluated as well. The maximum power density is about $2W/cm^3$ which is close to the theoretical value presented in Table 3.1.

In addition, the extractable electric power based on the more efficient SSHI interface is estimated in Figure 6-15. The power is evaluated in case of a moderate inversion quality factor ($Q_I = 10$). Nevertheless, a more efficient SSHI interface with higher Q_I can be implemented using high quality inductors and switching circuits. Up to $180\mu W$ power seems to be extractable using this interface. Nevertheless, at frequencies near the jump-down, there is a little room for electrical damping as explained above. The efficiency of the SSHI interface can be utilized in boosting the output power from lower frequencies as much as possible. Consequently, a more uniform and balanced output power similar to the Figure 3-20.

6.2 Start-up Circuit

As explained in Section3.5, the nonlinear harvester may be stabilized at two points for a range of frequencies. The high-energy stable solution which results in large stretching strain and the low-energy stable solution at which the device acts like a linear resonator with negligible generated stretching strain. Consequently, the high-energy stable region is preferred and should be used for energy harvesting. Nevertheless, stabilizing at the high-energy region requires a special excitation path. For example, the resonator can be slowly ramped up from lower frequencies. The other possibility is providing high-energy initial condition like a large initial deflection. Nevertheless, in practice the device is exposed to a vibration which normally pushes the resonator to the low-energy region. Therefore, a start-up mechanism which can push the system from the low-energy region to the high-energy solution seems necessary in practice.

For the first time, we propose a novel start-up circuit based on the 3rd-generation

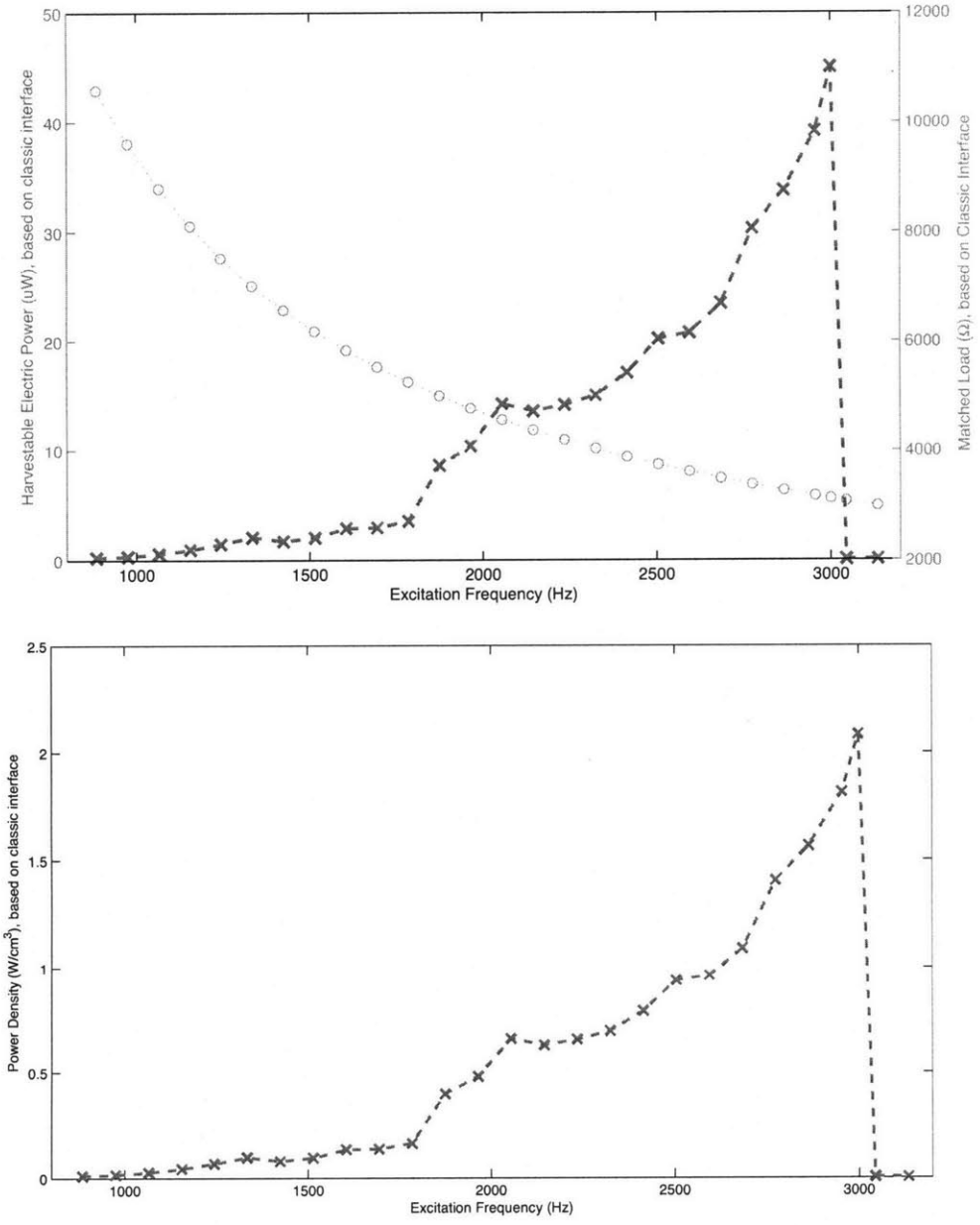

Figure 6-14: Calculated Matched resistive load, extractable electric power and the power density based on a classic AC interface.

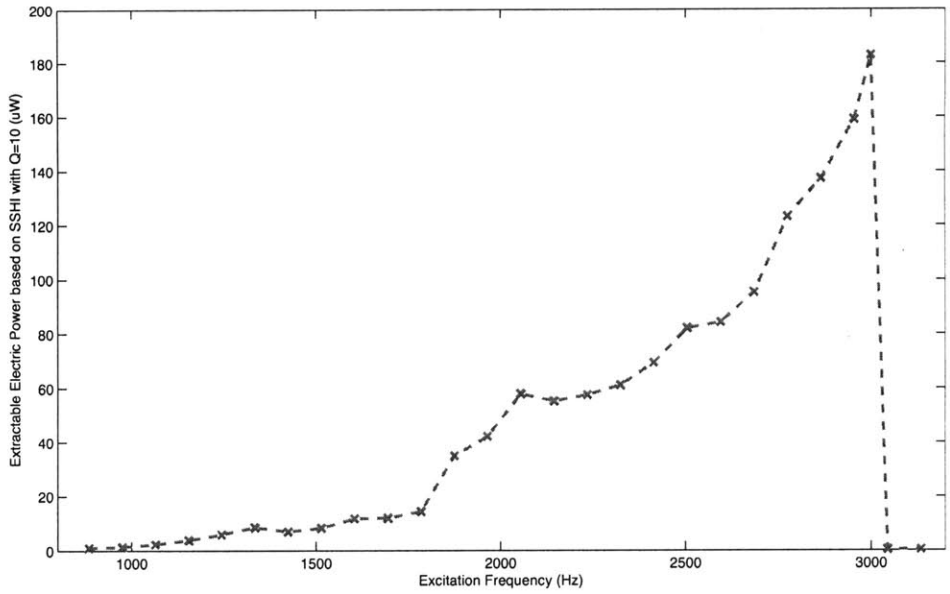

Figure 6-15: Calculated extractable electric power based on a SSHI interface (Q_I=10).

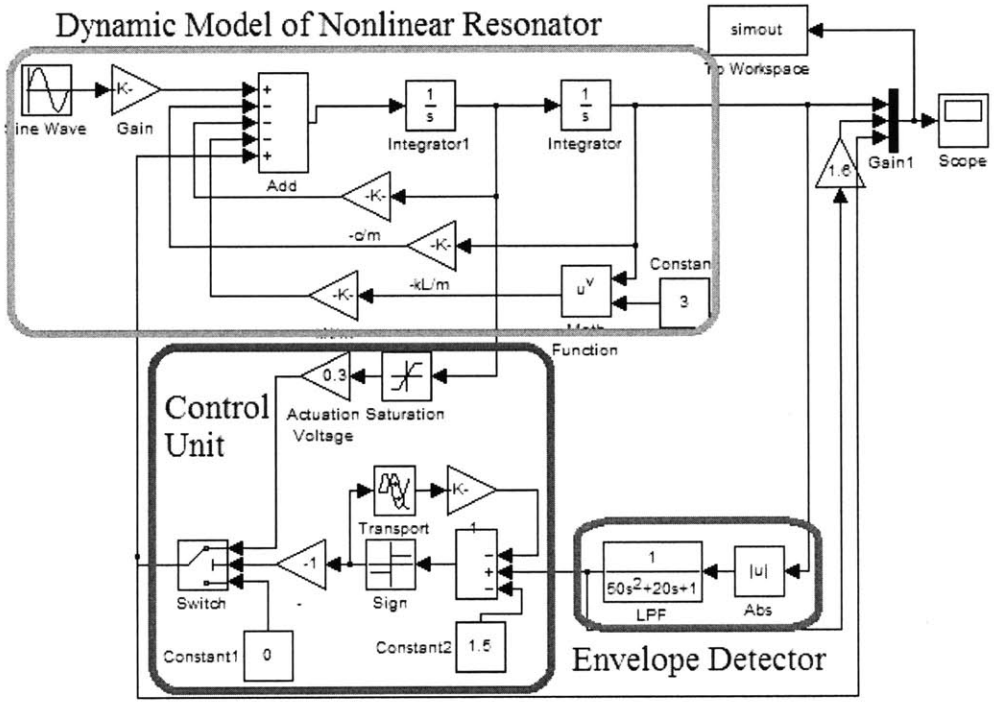

Figure 6-16: Block diagram of the start-up circuit simulated in MATLAB/Simulink.

piezoelectric energy harvester. This system is simulated using MATLAB/Simulink as shown in Figure 6-16. In this system, the amplitude of vibration is detected by the envelope detection unit which consist of a rectifier and a low-pass filter. In case of small amplitude, the control unit is activated which exploit the actuation mode of the piezoelectric layer for a short period of time. A bing-bang controller applies an actuation voltage to the piezoelectric layer during the start-up period. The sign of this constant voltage is determined by the direction of velocity. As a result, the piezoelectric layer applies a bending moment in sync with the motion of the proof mass. In other words, the control unit is increasing the amplitude of vibration by inducing a negative damping. Both amplitude and frequency of vibration is smoothly increased till it reaches the high-energy stable region. Subsequently, the control unit detects this mode from the amplitude of vibration and disables the actuation.

The startup circuit consumes small amount of energy for a short period of time. Afterward, the system goes back to the energy harvesting mode and can compensate the consumed energy in a short period of time. The response of the nonlinear harvester without and with the startup circuit is shown in Figure 6-17. Without the actuation mode, the system stays in the low-energy region forever and oscillates at a very small amplitude. By activating the actuation mode, the amplitude of vibration is increasing slowly till the system reaches the high-energy mode. Interestingly, the frequency of vibration is ramping up automatically by such a simple control scheme. The harvesting mode has been activated after only 70 time periods. Considering the typical frequency of vibration (about one hundred Hertz), 70Ts corresponds to less than a second.

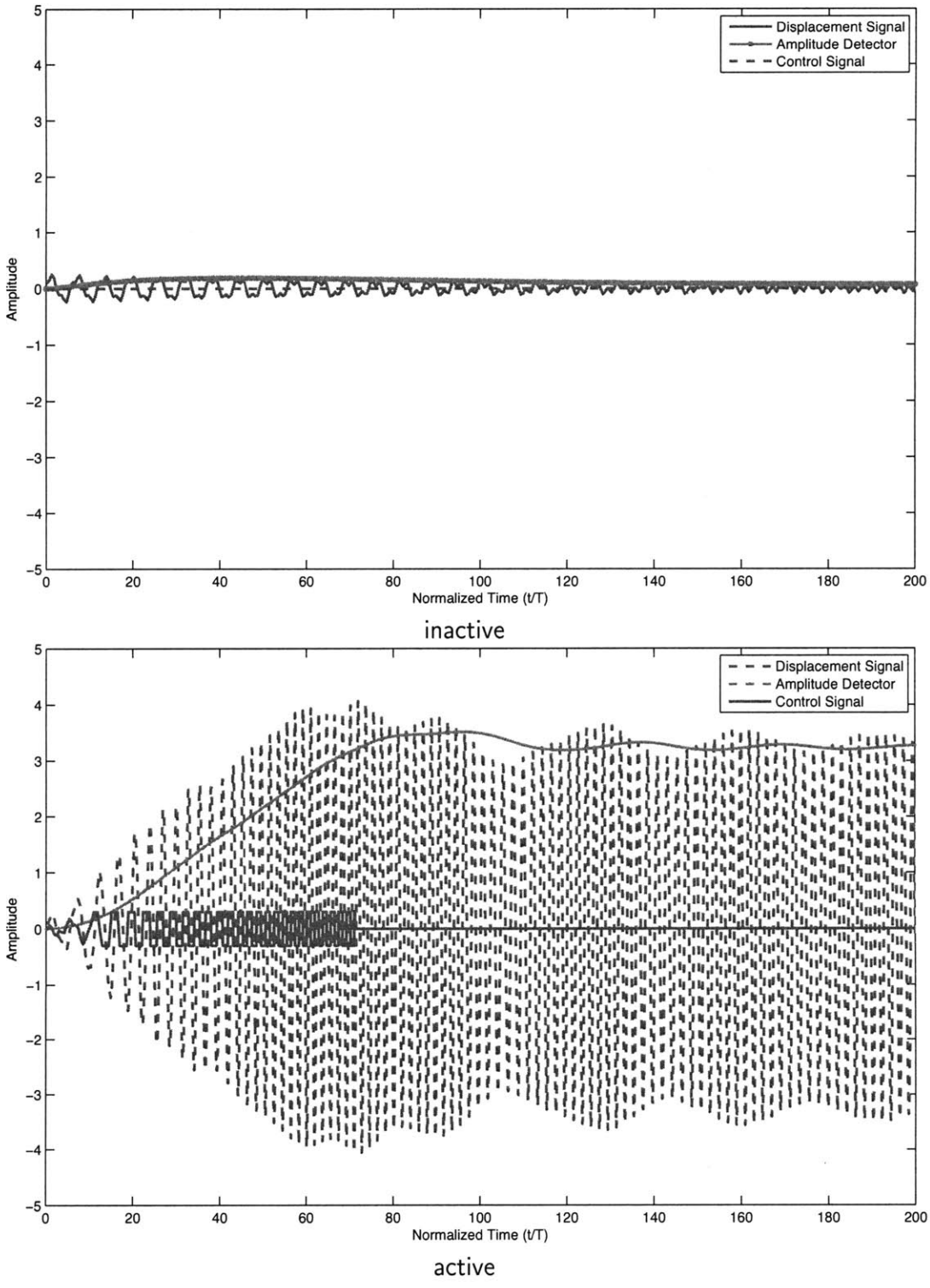

Figure 6-17: The effect of the start-up circuit on the response of the nonlinear energy harvester. Activating the circuit for a short period of time can push the system from low-amplitude stable region (up) to its high-amplitude stable region.

Chapter 7

Summary and Conclusions

7.1 Thesis Summary and Conclusion

A novel UWB piezoelectric MEMS-scale energy harvester has been designed, analyzed, fabricated and tested. The tensile stretching strain in thin doubly clamped structures in large deflection was suggested to achieve a wide bandwidth and high power density piezoelectric energy harvesting. A nonlinear electromechanical model of the nonlinear device was developed to verify the design. The concept of ultra wide-bandwidth energy harvesting based on a nonlinear resonator is presented for the first time. The power bandwidth can be improved by two orders of magnitude compared to the linear harvesters and expand up to 75% of the peak frequency.

A MEMS device was microfabricated to have a thin-film PZT on a silicon nitride membrane. The device was packaged and poled using a novel poling process which employs a limiting serial resistor as a negative feedback that avoids electric breakdown. The quality of the piezoelectric layer was monitored throughout the process by XRD crystallography and also P-V measurements. The electromechanical testing showed a much wider-bandwidth resonance of the excited beam which matches very well to the theoretical model. The device generated up to 1.5V (peak-to-peak) open circuit output in a wide range of frequencies. The dielectric constant, piezoelectric constant, and piezoelectric coupling factor are estimated $\epsilon_r = 2000$, d_{33}=110pm/V and k_{33}=20%, respectively.

Various electric interfaces and their compatibility with the nonlinear harvester were investigated. The maximum extractable power and the matched load for the tested device is estimated based on classic AC ($45\mu W$) and SSHI ($180\mu W$) interfaces. The stretching-based device shows an extremely high power generation density ($2W/cm^3$) which is three orders of magnitude higher than the typical bulk-scale harvesters. Employing the actuation mode of the piezoelectric layer, a startup circuit is proposed that can ensure the high-energy power generation response of the nonlinear device.

In conclusion, the stretching-based energy harvesting can be regarded as a new paradigm in energy harvesting that can provide high density electric power generation in a wide range of frequencies. This design can be easily implemented in practice to power ultra low-power electronic circuits.

7.2 Future Work

The piezoelectric energy harvester tested in this work employs only one layer of thick film PZT for testing purposes. However, the thickness of the film can be easily increase up to 1-2 microns by adding more layers. Accordingly, the extractable electric power can be scaled up to even higher values.

In addition, by minimizing the mechanical losses, it is easier to reach a resonance at smaller excitation amplitude. Furthermore, lower mechanical damping provides more room for electrical damping which increases the maximum extractable electric power. Vacuum packaging should be be considered for energy harvesting at extremely low vibration levels. The extractable power and also the bandwidth can be also improved by reducing the residual stress, employing heavier proof mass and increase the active area in the device.

This new design can be assembled in an stack to reach even higher power levels. All these approaches can be pursued to enhance the performance of this new system. In addition to the mechanical structure, the electric interface can also be improved. The electric interface can be designed specifically for the nonlinear harvester to improve the

energy harvesting efficiency and achieve the UWB performance. The startup circuit is required for a practical device and should be integrated in the ULP interface.

Appendix A

MATLAB Codes

A.1 Piezoelectric Energy Harvester Response

```
clear
fmin=200;fmax=1200;     %Frequency Range
Pm=zeros(1,1+fmax-fmin);
QQ=logspace(0,2.5,350);
%Device Dimensions
w=5e-3;l=4e-3;t=5.7e-6;Y=250e9/2;S0=10e6;rho=2330;tp=400e-6;wp=16e-3;Lp=16e-3;
Qa=80;Qs=1000;Qe=1e6;   %Damping Coefficients
m=rho*tp*wp*Lp  %Proof Mass
kl=(pi^2/2*t*w/l*S0+Y*pi^4/6*t^3*w/l^3)*4   %Linear Stiffness
kn=(Y*pi^4/8*t*w/l^3)*4     %Nonlinear Stiffness
A=20;   %Excitation Amplitude
for j=1:size(QQ,2),
    Qe=QQ(j);
    ca=sqrt(kl*m)/Qa;cs=ca*Qa/Qs;ce=ca*Qa/Qe;
    D=[];F=[];DU=[];DD=[];
    for f=fmin:fmax,
        w=2*pi*f;
    R=roots([9*kn^2/16*(1+cs^2/kl^2*w^2),1.5*kn*(kl+(ca+ce+cs)*cs/kl*w^2-m*w^2)...
```

```
        ,(ca+ce+cs)^2*w^2+(kl-m*w^2)^2,-m^2*A^2]); %Roots of Nonlinear Equations
        F=[F [f;f;f]];
        R=R.^.5.*(imag(R)==0);
        D=[D R];        DU=[DU max(R)];        DD=[DD min(R(find(R)))];
    end
    ii=find(D);
P=0.5*ce*DU.^2.*[fmin:fmax].^2*(2*pi)^2*1e6;Pm=max(Pm,P); %Maximum Power
end
figure('Position',[800-100 600-100 600 400])
plot(fmin:fmax,DU*1e6,'g.-',fmin:fmax,DD*1e6,'r.-')
xlabel('Excitation Frequency (Hz)');ylabel('Deflection Amplitude (\mum)');
xlim([fmin fmax])
Ss=pi^2/4*(DU/l).^2;
Sb=12*3.9e-6/l^2*DU;
figure('Position',[800-200 600-200 600 400])
plot(fmin:fmax,Sb*100,'c+-',fmin:fmax,Ss*100,'ro-')
plot(fmin:fmax,3*(Ss*1600).^2*pi*8.5e-9.*[fmin:fmax])
Pe=3e6*(Ss*1600).^2*pi*8.5e-9.*[fmin:fmax];
xlabel('Excitation Frequency (Hz)');ylabel('Strain (%)');xlim([fmin fmax])
figure('Position',[800 600 600 400])
Pem=min(Pm,Pe*2);
plot(fmin:fmax,Pm,'.',fmin:fmax,Pe*2,fmin:fmax,Pem,'r')
xlabel('Excitation Frequency (Hz)');
ylabel('Maximum Extractable Electrical Power (\muW)');xlim([fmin fmax])
```

A.2 Designing the Mask

```
XX=[-30 -10 10 30 -20 0 20 -20 0 20];
YY=[0 0 0 0 22 22 22 -22 -22 -22];
w1=0.100; %gap btw bus and the beam's edge
w2=0.100; %bus width
w3=0.050; %gap btw bus and electrode
g1=0.010; %gap btw PZT and bottom electrode
g2=0.030; %gap btw top electrode and PZT
g3=0.020; %gap btw bottom electrode and center line
g4=0.010; %PZT bridge extension length over bottom electrode
w4=0.050; %bus width on PZT bridge

w6=0.050; %Bottom Electrode Intrusion into beam
g5=0.050; %gap btw wirebond pads from edge
g6=0.50; %Device Etching Offset

L=2; %beams length
L1=2; %bar length
Lg=0.7; %Hole length
W=5; %beams width
W1=1.5; %distance btw opening and centerline
W2=1.5; %distance btw opening and edge
W3=0.5; %Opening width
Wg=2; %Hole width

X0=W1+W2+2*W3+W;
Y0=W1+W2+2*L+L1; %Length of Quarter

delete('EH1.scr');fid1 = fopen('EH1.scr','wt');   %Bottom Electrode
```

```
delete('EH2.scr');fid2 = fopen('EH2.scr','wt');   %PZT
delete('EH3.scr');fid3 = fopen('EH3.scr','wt');   %Top Electrode
delete('EH4.scr');fid4 = fopen('EH4.scr','wt');   %Nitride Etching
delete('EH5.scr');fid5 = fopen('EH5.scr','wt');   %Backside Etching

x0=W1+W3+W/2;y0=W1+L+L1/2;

%Mask 1: Bottom Electrode
X1=[x0-W/2+w1+w2+w3 x0-W/2+w1+w2+w3 x0+W/2-w1-w2 x0+W/2-w1-w2 X0-g5 X0-g5...
 x0+W/2-w1 x0+W/2-w1 x0-W/2+w1+w2+w3];
Y1=[y0+L1/2-w6 y0+L1/2+L/2-g3 y0+L1/2+L/2-g3 Y0-g5 Y0-g5 W1+3*W2/4+2*L+L1...
 W1+3*W2/4+2*L+L1 y0+L1/2-w6 y0+L1/2-w6];
X2=[x0-W/2+w1+w2+w3 x0-W/2+w1+w2+w3 x0+W/2-w1-w2 x0+W/2-w1-w2 X0-g5 X0-g5...
 x0+W/2-w1 x0+W/2-w1 x0-W/2+w1+w2+w3];
Y2=[y0-L1/2+w6 y0-L1/2-L/2+g3 y0-L1/2-L/2+g3 0.2*W1 0.2*W1 0.8*W1 0.8*W1...
 y0-L1/2+w6 y0-L1/2+w6];
X3=[x0-W/2+w1+w2 x0+W/2-w1-w2-w3 x0+W/2-w1-w2-w3 x0-W/2+w1 x0-W/2+w1...
 x0+W/2-w1-w2-w3 x0+W/2-w1-w2-w3 x0-W/2+w1+w2 x0-W/2+w1+w2];
Y3=[y0+L1/2+L/2+g3 y0+L1/2+L/2+g3 y0+L1/2+L+w6 y0+L1/2+L+w6 y0-L1/2-L-w6...
 y0-L1/2-L-w6 y0-L1/2-L/2-g3 y0-L1/2-L/2-g3 y0+L1/2+L/2+g3];
%Mask 2: PZT
X4=[x0-W/2+w1+w2+w3+g1 x0+W/2-w1-g1-w2-2*g2 x0+W/2-w1-g1-w2-2*g2...
 x0+W/2-w1-g1 x0+W/2-w1-g1 x0-W/2+w1+w2+w3+g1 x0-W/2+w1+w2+w3+g1];
Y4=[y0+L1/2-w6+g1 y0+L1/2-w6+g1 y0+L1/2-w6-g4 y0+L1/2-w6-g4...
 y0+L1/2+L/2-g3-g1 y0+L1/2+L/2-g3-g1 y0+L1/2-w6+g1];
X5=X4;Y5=2*y0-Y4;
X6=[x0-W/2+w1+g1 x0+W/2-w1-w2-w3-g1 x0+W/2-w1-w2-w3-g1 x0-W/2+w1+g1+2*g2+w2...
 x0-W/2+w1+g1+2*g2+w2 x0-W/2+w1+g1 x0-W/2+w1+g1];
Y6=[y0+L1/2+L/2+g3+g1 y0+L1/2+L/2+g3+g1 y0+L1/2+L+w6-g1 y0+L1/2+L+w6-g1...
 y0+L1/2+L+w6+g4 y0+L1/2+L+w6+g4 y0+L1/2+L/2+g3+g1];
```

```
X7=X6;Y7=2*y0-Y6;
%Mask 3: Top Electrode
X8=[x0-W/2+w1+w2+w3+g1+g2 x0+W/2-w1-g1-w2-g2 x0+W/2-w1-g1-w2-g2...
 x0-W/2+w1+w2+w3+g1+g2 x0-W/2+w1+w2+w3+g1+g2 x0+W/2-w1-g1-g2...
  x0+W/2-w1-g1-g2 x0-W/2+w1+w2+w3+g1+g2 x0-W/2+w1+w2+w3+g1+g2];
Y8=[y0+L1/2-w6+g1+g2 y0+L1/2-w6+g1+g2 y0-L1/2+w6-g1-g2 y0-L1/2+w6-g1-g2...
 y0-L1/2-L/2+g3+g1+g2 y0-L1/2-L/2+g3+g1+g2 y0+L1/2+L/2-g3-g1-g2...
  y0+L1/2+L/2-g3-g1-g2 y0+L1/2-w6+g1+g2];
X9=[x0-W/2+w1+g1+g2 x0+W/2-w1-w2-w3-g1-g2 x0+W/2-w1-w2-w3-g1-g2...
 x0-W/2+w1+g1+g2+w2 x0-W/2+w1+g1+g2+w2 x0 x0 x0-W/2+w1+g1+g2 x0-W/2+w1+g1+g2];
Y9=[y0+L1/2+L/2+g3+g1+g2 y0+L1/2+L/2+g3+g1+g2 y0+L1/2+L+w6-g1-g2...
 y0+L1/2+L+w6-g1-g3 W1+1*W2/4+2*L+L1 W1+1*W2/4+2*L+L1 W1+2*W2/4+2*L+L1...
  W1+2*W2/4+2*L+L1 y0+L1/2+L/2+g3+g1+g2];
X10=[x0-W/2+w1+g1+g2 x0+W/2-w1-w2-w3-g1-g2 x0+W/2-w1-w2-w3-g1-g2 x0-W/2+w1+...
g1+g2+w2 x0-W/2+w1+g1+g2+w2 X0-g5 X0-g5 x0-W/2+w1+g1+g2 x0-W/2+w1+g1+g2];
Y10=[y0-L1/2-L/2-g3-g1-g2 y0-L1/2-L/2-g3-g1-g2 y0-L1/2-L-w6+g1+g2 y0-L1/2-L-...
w6+g1+g2 -0.2*W1 -0.2*W1 -0.8*W1 -0.8*W1 y0-L1/2-L/2-g3-g1-g2];
%Mask 4: Nitride Etching
X11=[W1 W1+W3 W1+W3 W1 W1];Y11=[W1 W1 W1+2*L+L1 W1+2*L+L1 W1];
X12=[W1+W3+W W1+2*W3+W W1+2*W3+W W1+W3+W W1+W3+W];Y12=Y11;
%Mask 5: Backside Etching
X13=[W1 W1+2*W3+W W1+2*W3+W W1 W1];Y13=[W1 W1 W1+2*L+L1 W1+2*L+L1 W1];
X14=x0+[-Wg Wg Wg -Wg -Wg]/2;Y14=y0+[-Lg -Lg Lg Lg -Lg]/2;X15=X14;Y15=Y14;
X16=x0+[-W W W -W -W]/2;Y16=y0+[-L1 -L1 L1 L1 -L1]/2;
M=[1 1 1 2 2 2 2 3 3 3 4 4 5 4 5 5];
SQ=[-X0 X0 X0 -X0 -X0;-Y0 -Y0 Y0 Y0 -Y0];
SQe=[-X0-g6 X0+g6 X0+g6 -X0-g6 -X0-g6;-Y0-g6 -Y0-g6 Y0+g6 Y0+g6 -Y0-g6];

for k=1:size(XX,2),
    for m=1:size(M,2),
```

```
        xx=eval(['X' num2str(m)]);yy=eval(['Y' num2str(m)]);
        for j=0:3,
            p=j*pi/2;
            T=[cos(p) -sin(p);sin(p) cos(p)];
            XY=T*[xx;yy];
            fprintf(eval(['fid' num2str(M(m))]),'_POLYLINE\n');
            for i=1:size(XY,2)
     fprintf(eval(['fid' num2str(M(m))]),'%f,%f\n',XY(1,i)+XX(k),XY(2,i)+YY(k));
            end
            fprintf(eval(['fid' num2str(M(m))]),'\n');
        end
    end
     fprintf(fid4,'_POLYLINE\n');fprintf(fid5,'_POLYLINE\n');
     for i=1:5,
         fprintf(fid4,'%f,%f\n',SQ(1,i)+XX(k),SQ(2,i)+YY(k));
         fprintf(fid5,'%f,%f\n',SQ(1,i)+XX(k),SQ(2,i)+YY(k));
     end
     fprintf(fid4,'\n');fprintf(fid5,'\n');
     fprintf(fid4,'_POLYLINE\n');fprintf(fid5,'_POLYLINE\n');
     for i=1:5,
         fprintf(fid4,'%f,%f\n',SQe(1,i)+XX(k),SQe(2,i)+YY(k));
         fprintf(fid5,'%f,%f\n',SQe(1,i)+XX(k),SQe(2,i)+YY(k));
     end
     fprintf(fid4,'\n');fprintf(fid5,'\n');
end

fclose(fid1);fclose(fid2);fclose(fid3);fclose(fid4);fclose(fid5);
```

A.3 Interdigitated Electrodes Mask, 3rd Generation

```
f=0.004;g=0.004;fl=1-.032;L=4.496+0.016;wb=0.035;Lb=0.25;
x0=22.174;y0=28.55;x1=x0+2*g;y1=y0-2*g;
delete('EHIDT.scr');fid = fopen('EHIDT.scr','wt'); %Bottom Electrode
X1=[-wb -wb];Y1=[fl+6*g+wb 0];
X2=[wb+2*g wb+2*g L+wb L+wb];Y2=[fl+6*g+wb fl-5*g+wb fl-5*g+wb 0];
for iii=1:fl/2/(f+g),
    i=iii-1;
     Y1=[Y1 i*2*(f+g) i*2*(f+g) i*2*(f+g)+f i*2*(f+g)+f];
     X1=[X1 0 L L 0];
     Y2=[Y2 i*2*(f+g) i*2*(f+g) i*2*(f+g)+f i*2*(f+g)+f];
     X2=[X2 L 0 0 L];
 end
X1=[X1 0];
Y1=[Y1 fl+6*g+wb];
X2=[X2 L 2*g 2*g];
Y2=[Y2 fl-2*g fl-2*g fl+6*g+wb];
X3=26.838-X1-x0;Y3=28.458-Y1-y0;
X4=26.83-X2-x1;Y4=28.45-Y2-y1;
fprintf(fid,'_PLINE\n');
for i=1:size(X1,2)
    fprintf(fid,'%f,%f\n',x0+X1(i),y0+Y1(i));
end
fprintf(fid,'\n');
fprintf(fid,'_PLINE\n');
for i=1:size(X2,2)
    fprintf(fid,'%f,%f\n',x1+X2(i),y1+Y2(i));
end
```

```
fprintf(fid,'\n');
fprintf(fid,'_PLINE\n');
for i=1:size(X3,2)
    fprintf(fid,'%f,%f\n',x0+X3(i),y0+Y3(i));
end
fprintf(fid,'\n');
fprintf(fid,'_PLINE\n');
for i=1:size(X4,2)
    fprintf(fid,'%f,%f\n',x1+X4(i),y1+Y4(i));
end
fprintf(fid,'\n');
fclose(fid);
```

Appendix B

Masks

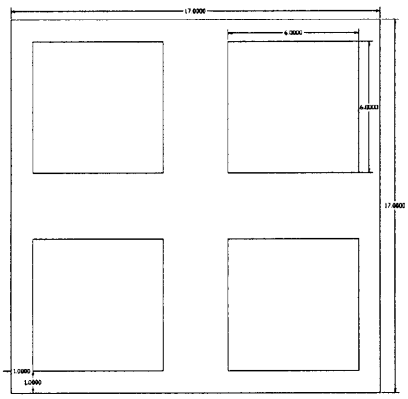

Base (top-side)

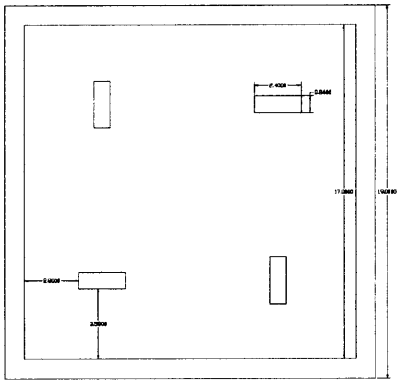

Base (back-side)

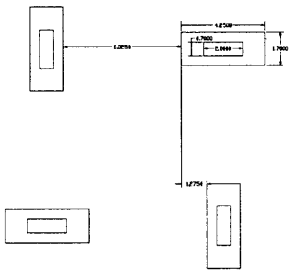

Proof Mass (top-side)

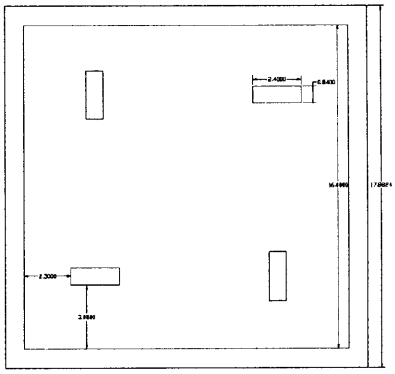

Proof-Mass (back-side)

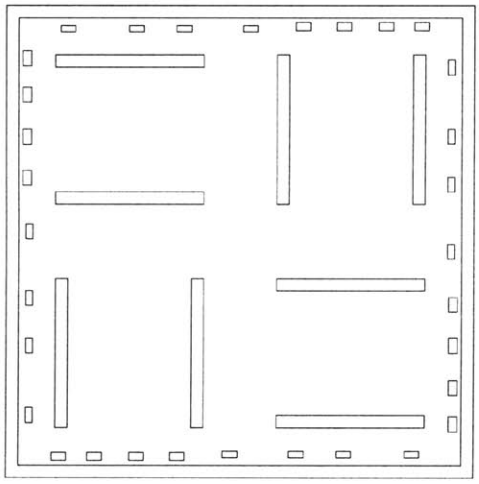

Passivation Layer RIE

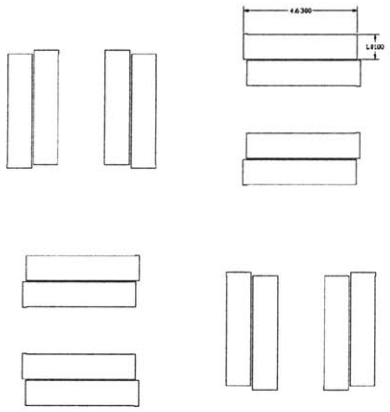

PZT Layer Wet-Etching

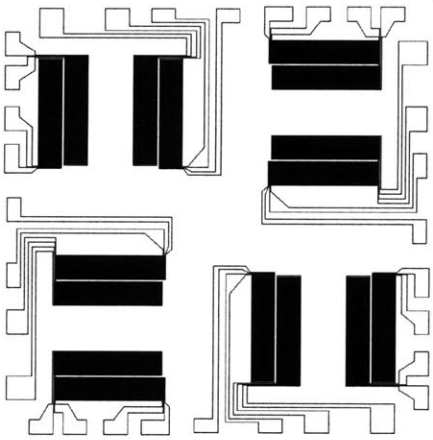

IDT Electrodes

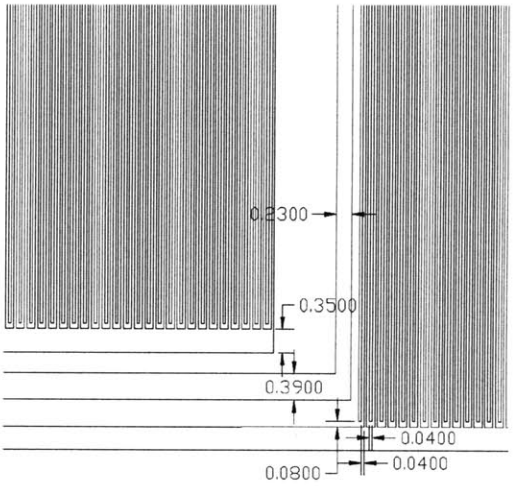

IDT Electrodes (scale 10x)

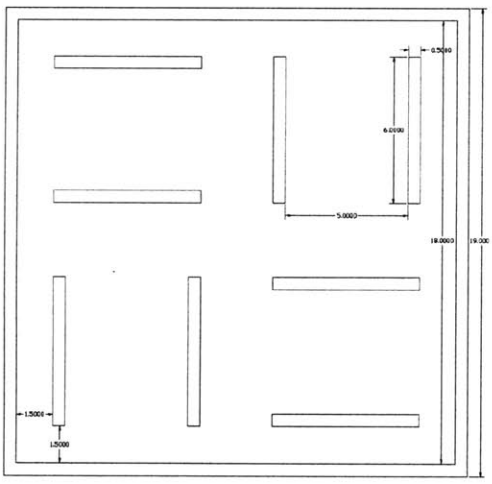

Structural Layer RIE

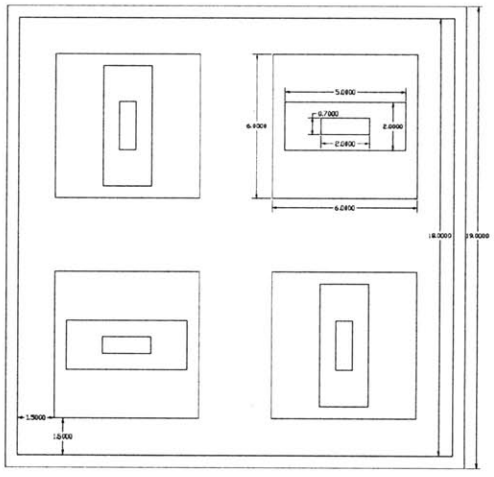

Backside DRIE

Bibliography

[1] Roundy S, Wright P and Rabaey J 2003 *Computer Communications* **26** 1131–1144

[2] Prof. shad roundy homepage, australian national university `http://engnet.anu.edu.au/DEpeople/Shad.Roundy`

[3] Roundy S, Wright P and Rabaey J 2004 *Energy scavenging for wireless sensor networks: with special focus on vibrations* (Springer Netherlands)

[4] Amirtharajah R and Ch A P 1998 *IEEE Journal of Solid-State Circuits* **33** 687–695

[5] Marioli D, Sardini E and Serpelloni M 2009 *Procedia Chemistry* **1** 469–472

[6] Wikipedia, piezoelectricity `http://en.wikipedia.org/wiki/Piezoelectricity`

[7] Piezoelectric ceramics: Principles and applications `http://www.americanpiezo.com/piezo_theory`

[8] Sood R K 2003 *Piezoelectric Micro Power Generator (PMPG) : a MEMS-based energy scavenger* Master's thesis Massachusetts Institute of Technology. Dept. of Electrical Engineering and Computer Science.

[9] Kymissis J, Kendall C, Paradiso J and Gershenfeld N 1998 Parasitic power harvesting in shoes *Proc. of the Second IEEE International Conference on Wearable Computing (ISWC), IEEE Computer Society Press* pp 132–139

[10] Jeon Y, Sood R, h Jeong J and Kim S G 2005 *Sensors and Actuators A: Physical* **122** 16 – 22 ISSN 0924-4247

[11] Liu J Q, Fang H B, Xu Z Y, Mao X H, Shen X C, Chen D, Liao H and Cai B C 2008 *Microelectronics Journal* **39** 802 – 806 ISSN 0026-2692

[12] Goldschmidtboeing F and Woias P 2008 *Journal of Micromechanics and Microengineering* **18** 104013

[13] Qiu J, Jiang H, Ji H and Zhu K 2009 *Frontiers of Mechanical Engineering in China* **4** 153–159

[14] Guyomar D, Badel A, Lefeuvre E and Richard C 2005 *IEEE transactions on ultrasonics, ferroelectrics, and frequency control* **52**

[15] Ramadass Y and Chandrakasan A 2010 *IEEE journal of solid-state circuits* **45** 189

[16] Yang B, Lee C, Kotlanka R, Xie J and Lim S 2010 *Journal of Micromechanics and Microengineering* **20** 065017

[17] Beeby S P, Tudor M J and White N M 2006 *Measurement Science and Technology* **17** R175–R195

[18] Energy harvesting: Ulp meets energy harvesting, a game-changing combination for design engineers `http://www.ti.com/corp/docs/landing/cc430/graphics/slyy018_20081031.pdf`

[19] Williams C, Shearwood C, Harradine M, Mellor P, Birch T and Yates R 2001 *IEE Proceedings-Circuits, Devices and Systems* **148** 337–342

[20] Shearwood C and Yates R 1997 *Electronics Letters* **33** 1883–1884

[21] El-Hami M, Glynne-Jones P, White N, Hill M, Beeby S, James E, Brown A and Ross J 2001 *Sensors and Actuators A: Physical* **92** 335–342

[22] Mizuno M and Chetwynd D 2003 *Journal of Micromechanics and Microengineering* **13** 209

[23] Glynne-Jones P, Tudor M, Beeby S and White N 2004 *Sensors and Actuators A: Physical* **110** 344–349

[24] Perpetuum ltd. `http://www.perpetuum.com`

[25] Kulah H and Najafi K 2004 An electromagnetic micro power generator for low-frequency environmental vibrations *Micro Electro Mechanical Systems, 2004. 17th IEEE International Conference on.(MEMS)* pp 237–240

[26] Huang W S, Tzeng K E, Cheng M C and Huang R S 2003 Design and fabrication of a vibrational micro-generator for wearable mems *Proc. Eurosensors XVII (Guimaraes, Portugal)*

[27] Perez-Rodriguez A, Serre C and Fondevilla N 2005 Design of electromagnetic inertial generators for energy scavenging applications *Proceeedings of Eurosensors XIX, Barcelona, Spain*

[28] Beeby S, Tudor M, Koukharenko E, White N, O'Donnell T, Saha C, Kulkarni S and Roy S 2005 Micromachined silicon generator for harvesting power from vibrations *Proc. Transducers (Seoul, Korea)*

[29] Li W, Wen Z, Wong P, Chan G and Leong P 2000 A micromachined vibration-induced power generator for low power sensors of robotic systems *World Automation Congress: 8th Int. Symp. on Robotics with Applications (Hawaii)*

[30] Ching N, Wong H, Li W, Leong P and Wen Z 2000 A laser-micromachined vibrational to electrical power transducer for wireless sensing systems *11th International Conference on Solid-State Sensors and Actuators, Munich, Germany*

[31] Scherrer S, Plumlee D and Moll A 2005 Energy scavenging device in ltcc materials *2005 IEEE Workshop on Microelectronics and Electron Devices, 2005. WMED'05* pp 77–78

[32] Meninger S, Mur-Miranda J, Amirtharajah R, Chandrakasan A, Lang J and MIT C 2001 *IEEE Transactions on Very Large Scale Integration (VLSI) Systems* **9** 64–76

[33] Kuehne I, Frey A, Marinkovic D, Eckstein G and Seidel H 2008 *Sensors and Actuators A: Physical* **142** 263–269

[34] Chiu Y and Tseng V 2008 *Journal of Micromechanics and Microengineering* **18** 104004

[35] Hoffmann D, Folkmer B and Manoli Y 2009 *Journal of Micromechanics and Microengineering* **19** 094001

[36] Basrour S, Chaillout J, Charlot B, Despesse G, Jager T, Leger J and Vassilev A 2005 Fabrication and characterization of high damping electrostatic micro devices for vibration energy scavenging *Proc. DTIP'05* pp 386–90

[37] Basset P, Galayko D, Paracha A, Marty F, Dudka A and Bourouina T 2009 *Journal of Micromechanics and Microengineering* **19** 115025

[38] Arakawa Y, Suzuki Y and Kasagi N 2004 Micro seismic power generator using electret polymer film *Proc. PowerMEMS* pp 187–190

[39] Lo H and Tai Y 2008 *Journal of Micromechanics and Microengineering* **18** 104006

[40] Naruse Y, Matsubara N, Mabuchi K, Izumi M and Suzuki S 2009 *Journal of Micromechanics and Microengineering* **19** 094002 (5pp)

[41] Mitcheson P, Stark B, Miao P, Yeatman E, Holmes A and Green T 2003 Analysis and optimization of mems on-chip power supply for self powering of slow moving sensors *Proc. Eurosensors XVII (Guimaraes, Portugal)* pp 30–31

[42] Shenck N and Paradiso J 2001 *IEEE Micro* **21** 30–42

[43] Ramsay M and Clark W 2001 Piezoelectric energy harvesting for bio-mems applications *Proceedings of SPIE* vol 4332 p 429

[44] Glynne-Jones P, Beeby S and White N 2001 *IEE Proceedings-Science, Measurement and Technology* **148** 68–72

[45] Sodano H, Park G and Inman D 2004 *Strain* **40** 49–58

[46] Duggirala R, Li H, Pappu A, Fu Z, Aspel A and Lal A 2004 *Proc. PowerMEMS* 133–136

[47] Bayrashev A, Robbins W and Ziaie B 2004 *Sensors and Actuators A: Physical* **114** 244–249

[48] Marzencki M, Basrour S, Charlot B, Grasso A, Colin M and Valbin L 2005 Design and fabrication of piezoelectric micro power generators for autonomous microsystems *Proc. of DTIP05* pp 299–302

[49] van Schaijk R, Elfrink R, Kamel T and Goedbloed M 2008 *2008 IEEE Sensors* 45–48

[50] Kim H, Bedekar V, Islam R, ho Lee W, Leo D and Priya S 2008 *Ultrasonics, Ferroelectrics and Frequency Control, IEEE Transactions on* **55** 1900–1905 ISSN 0885-3010

[51] Shen D 2009 *Piezoelectric energy harvesting devices for low frequency vibration applications* Ph.D. thesis AUBURN UNIVERSITY

[52] Shen D, Park J H, Ajitsaria J, Choe S Y, III H C W and Kim D J 2008 *Journal of Micromechanics and Microengineering* **18** 055017

[53] Kok S, White N and Harris N 2009 *Measurement Science and Technology* **20** 124010

[54] Park J and Park J 2009 Micromachined piezoelectric energy harvester with low vibration *Applications of Ferroelectrics, 2009. ISAF 2009. 18th IEEE International Symposium on the* (IEEE) pp 1–6

[55] Shen D, Park J H, Noh J H, Choe S Y, Kim S H, III H C W and Kim D J 2009 *Sensors and Actuators A: Physical* **154** 103 – 108 ISSN 0924-4247

[56] Lee B, Lin S, Wu W, Wang X, Chang P and Lee C 2009 *Journal of Micromechanics and Microengineering* **19** 065014

[57] Elfrink R, Renaud M, Kamel T, de Nooijer C, Jambunathan M, Goedbloed M, Hohlfeld D, Matova S and van Schaijk R 2009 Vacuum packaged mems piezoelectric vibration energy harvesters *PowerMEMS*

[58] Muralt P, Marzencki M, Belgacem B, Calame F and Basrour S 2009 *Procedia Chemistry* **1** 1191–1194

[59] Morimoto K, Kanno I, Wasa K and Kotera H 2010 *Sensors and Actuators A: Physical*

[60] Park J 2010 *Development of MEMS Piezoelectric Energy Harvesters* Master's thesis Auburn University

[61] Anton S R and Sodano H A 2007 *Smart Materials and Structures* **16** 1–21

[62] Reilly EK; Wright P 2006 Thin film piezoelectric energy scavenging systems for an on-chip power supply *Proceedings Power MEMS*

[63] Erturk A and Inman D 2008 *Journal of Intelligent Material Systems and Structures* **19** 1311–1325

[64] Choi W, Jeon Y, Sood R and Kim S 2006 *Journal of Electroceramics* **17** 543–548

[65] Xia Y 2006 *Self-powered wireless sensor system using MEMS piezoelectric micro power generator (PMPG)* Master's thesis Massachusetts Institute of Technology. Dept. of Electrical Engineering and Computer Science.

[66] Charnegie D 2007 *Frequency Tuning Concepts For Piezoelectric Cantilever Beams And Plates For Energy Harvesting* Master's thesis University of Pittsburgh

[67] Halvorsen E 2007 Broadband excitation of resonant energy harvesters *PowerMEMS2007*

[68] Shahruz S 2008 *Journal of Vibration and Control* **14** 753–768

[69] Challa V R, Prasad M G and Fisher F T 2007 Resonant frequency tunable vibration energy harvesting device *The 6th International Workshop on Structural Health Monitoring*

[70] Hajati A and Kim S G 2008 Rectifier-less piezoelectric micro power generator *Active and Passive Smart Structures and Integrated Systems 2008* vol 6928 (SPIE)

[71] Hajati A and Kim S G 2009 Wide-bandwidth mems-scale piezoelectric energy harvester *Proceedings Power MEMS* pp 269–272

[72] Intel core i5-540um processor
`http://ark.intel.com/Product.aspx?id=49159`

[73] Snapdragon cpu by qualcomm
`http://en.wikipedia.org/wiki/Snapdragon_processor`

[74] Harb A 2010 *Renewable Energy*

[75] Chau K, Lewis S, Zhao Y, Howe R, Bart S and Marcheselli R 1996 *Sensors and Actuators A: Physical* **54** 472–476

[76] Chau K, Sulouff R *et al.* 1998 *Microelectronics Journal* **29** 579–586

[77] Mide, commercial piezoelectric energy harvester provider `http://www.mide.com`

[78] Priya S 2007 *Journal of Electroceramics* **19** 165–182

[79] Paradiso J and Starner T 2005 *IEEE Pervasive computing* **4** 18–27

[80] Op het Veld B, Hohlfeld D and Pop V 2009 *Information Systems Frontiers* **11** 7–18

[81] Lefeuvre E, Sebald G, Guyomar D, Lallart M and Richard C 2009 *Journal of Electroceramics* **22** 171–179

[82] Vullers R, van Schaijk R, Doms I, Van Hoof C and Mertens R 2009 *Solid-State Electronics* **53** 684–693

[83] Muralt P, Polcawich R and Trolier-McKinstry S 2009 *MRS BULLETIN* **34**

[84] Mitcheson P, Yeatman E, Rao G, Holmes A and Green T 2008 *Proceedings of the IEEE* **96** 1457–1486 ISSN 0018-9219

[85] Sodano A 2008 *Technical Digest PowerMEMS 2007 (Freiburg, Germany, 28–29 November 2007)* 39–44

[86] Bogue R 2009 *Sensor Review* **29** 194–199

[87] Farmer J 2007 *A comparison of power harvesting techniques and related energy storage issues* Master's thesis Virginia Polytechnic Institute and State University

[88] Park G, Rosing T, Todd M D, Farrar C R and Hodgkiss W 2008 *Journal of Infrastructure Systems* **14** 64–79

[89] Cook-Chennault K A, Thambi N and Sastry A M 2008 *Smart Materials and Structures* **17** 043001 (33pp)

[90] Dongna Shen Song-Yul Choe D J K 2007 Comparison of piezoelectric materials for vibration energy conversion devices *Mater. Res. Soc. Symp. Proc.* 0966-T07-34 (MRS)

[91] Majidi C, Haataja M and Srolovitz D 2010 *Smart Materials and Structures* **19** 055027

[92] Song H, Choi Y, Wang G and Wereley N 2009 *Journal of Mechanical Design* **131** 091008

[93] Mathers A, Moon K and Yi J 2009 *Sensors Journal, IEEE* **9** 731–739 ISSN 1530-437X

[94] Erturk A and Inman D J 2008 *Smart Materials and Structures* **17** 065016 (14pp)

[95] Renno J M, Daqaq M F and Inman D J 2009 *Journal of Sound and Vibration* **320** 386 – 405 ISSN 0022-460X

[96] Kim M, Hoegen M, Kim W S, Kim S H, Dugundji J and Wardle B L 2007 Proof mass modeling considerations in cantilevered piezoelectric vibration energy harvesters *Mater. Res. Soc. Symp. Proc.* 1120-M08-01

[97] Lewandowski B E 2009 *An implantable, stimulated muscle powered piezoelectric generator* Ph.D. thesis Case Western Reserve University

[98] Saha C, O'Donnell T, Wang N and McCloskey P 2008 *Sensors and Actuators A: Physical* **147** 248 – 253 ISSN 0924-4247

[99] Guan M and Liao W 2008 *Journal of Intelligent Material Systems and Structures* **19** 671–680

[100] Challa V R, Prasad M G and Fisher F T 2009 *Smart Materials and Structures* **18** 095029 (11pp)

[101] Hua-Bin F, Jing-Quan L, Zheng-Yi X, Lu D, Di C, Bing-Chu C and Yue L 2006 *Chinese Physics Letters* **23** 732

[102] Wischke M, Masur M, Goldschmidtboeing F and Woias P 2010 *Journal of Micromechanics and Microengineering* **20** 035025

[103] Mann B and Sims N 2009 *Journal of Sound and Vibration* **319** 515–530

[104] Stanton S, McGehee C and Mann B 2010 *Physica D: Nonlinear Phenomena*

[105] Cottone F, Vocca H and Gammaitoni L 2009 *Physical Review Letters* **102** 080601 (pages 4)

[106] Barton D, Burrow S and Clare L 2010 *Journal of Vibration and Acoustics* **132** 021009

[107] Kulah H and Najafi K 2008 *IEEE Sensors Journal* **8** 261–268

[108] Marinkovic B and Koser H 2009 *Applied Physics Letters* **94** 103505 (pages 3)

[109] Senturia S D 2004 *Microsystem Design* (Springer)

[110] Timoshenko S P and Goodier J 1970 *Theory of Elasticity* 3rd ed (McGraw Hill Higher Education)

[111] Brotz J 2004 *Damping in CMOS-MEMS resonators* Master's thesis Carnegie Mellon University

[112] Mickens R 1981 *An introduction to nonlinear oscillations* (Cambridge Univ Pr)

[113] duToit N, Wardle B and Kim S 2005 *Integrated Ferroelectrics* **71** 121–160

[114] Badel A, Guyomar D, Lefeuvre E and Richard C 2005 *Journal of intelligent material systems and structures* **16** 889

[115] Lefeuvre E, Badel A, Richard C, Petit L and Guyomar D 2006 *Sensors and Actuators A: Physical* **126** 405–416

[116] Bathurst S, Lee H and Kim S 2008 *Digital Fabrication* 897–901

[117] Traina Z J 2007 *A large strain piezoelectric microactuator by folding assembly* Master's thesis Massachusetts Institute of Technology

[118] Wong C 2003 *Strain-tuning of periodic optical devices: tunable gratings and photonic crystals* Ph.D. thesis Massachusetts Institute of Technology

[119] Soyama N, Maki K, Mori S and Ogi K 2000 *Jpn. J. Appl. Phys., Part 1* **39** 5434–5436

[120] Flinn P 1989 Principles and applications of wafer curvature techniques for stress measurements in thin films *Mater. Res. Soc. Symp. Proc* vol 130 pp 41–51

[121] Chen K and Ou K 2002 *Journal of Micromechanics and Microengineering* **12** 917

[122] Chen K 2006 *MEMS/NEMS* 1252–1328

[123] Chen K, Zhang X and Lin S 2003 *Thin Solid Films* **434** 190–202

[124] Morin P, Martinez E, Wacquant F and Regolini J 2005 Thermal stress relaxation of plasma enhanced chemical vapor deposition silicon nitride *Materials research society symposium proceedings* vol 875 (Warrendale, Pa.; Materials Research Society; 1999) p 437

[125] Mackenzie K, Johnson D, DeVre M, Westerman R and Reelfs B 2005 Stress control of si-based pecvd dielectrics *Silicon nitride, silicon dioxide thin insulating films, and other emerging dielectrics VIII: proceedings of the international symposium* (The Electrochemical Society) p 148

[126] Plasma quest ecr etcher, stanford nanofabrication facility `https://snf.stanford.edu/SNF/equipment/dry-etching/plasma-quest-ecr-etcher-pquest-contaminated`

[127] Spectrum semiconductor materials, inc `http://www.spectrum-semi.com`

[128] Wikipedia, laser doppler vibrometer `http://en.wikipedia.org/wiki/Laser_Doppler_vibrometer`

[129] Maurath D, Peters C, Hehn T, Ortmanns M and Manoli Y *Advances in Radio Science-Kleinheubacher Berichte* **6**

[130] Richard C, Guyomar D, Audigier D and Bassaler H 2000 Enhanced semi-passive damping using continuous switching of a piezoelectric device on an inductor *Proceedings of SPIE* vol 3989 p 288

[131] Ammar Y and Barsour S 2007 *Arxiv preprint arXiv:0711.3308*